Structure and evolution of deformation-band-dominated faults in porous volcaniclastic rocks.
Insights from Eastern Taiwan

Master in Petroleum Geology/Structural Geology

Hanna Serina Jervidalo

Department of Earth Science
University of Bergen

June 2018

ABSTRACT

This MSc project documents fault evolution in porous volcaniclastic rocks of Miocene age in Shihtiping, Eastern Taiwan. Sequential fault evolution in porous sandstone, and to some extent in carbonates, has been studied for several decades. It is widely recognised that formation of faults in porous rocks includes a sequential evolution as a result of progressive shear. Fault formation initiates from simple deformation band structures with small displacements to form more complex band structures. By progressive shear and strain hardening deformation bands may evolve into faults with continuous slip surfaces. Despite extensive studies on deformation bands and fault evolution in other porous rocks, there are significantly less studies conducted on the subject in volcaniclastic rocks. This study aims to fill the knowledge gap and expand our understanding of fault evolution in porous volcaniclastic rocks. In order to do so, an outcrop-based study on strike-slip deformation bands and faults in volcaniclastic rocks along the eastern coast of Taiwan has been conducted.

By documenting and quantifying the geometry of deformation bands and faults in the study area, a sequential fault evolution model for porous volcaniclastic rocks was developed. In the presented model, displacement is used as a proxy for its division. The *initial stage* of fault formation is characterised by small deformation bands with mm-cm-scale displacements accommodated through granular flow and cataclastic flow mechanisms. Deformation bands at the initial stage are comprised of single or a few strands. By progressive shear, linking and interaction, deformation bands may evolve into the *intermediate stage* of fault development. This stage is characterised by several-stranded deformation band clusters and networks with patchy slip surfaces. Displacements at this stage range between 5 and 50 centimetres and is accommodated through a combination of cataclastic flow and discrete brittle failure. Formation of through-going slip surfaces and accumulation of significant shear displacement (>0.5 metres) characterise the *final fault stage*. Discrete brittle failure replaces cataclastic flow as the dominating deformation mechanism at the final fault stage.

This study documents fault architecture in a porous volcaniclastic succession by detailed mapping and topological analysis. Fault architecture is a function of displacement lithology and structural position along strike. The fault core is either dominated by slip surfaces within a shear-zone of deformation bands or discrete brittle failure. In terms of lithological control, the porosity, volcanic glass content and number of lithic fragments in the host rock control the fault core architecture. Linking of deformation bands and fault segments are associated with structural complex zones and high structural connectivity at all stages of fault evolution.

This study does not only contribute to the understanding of deformation band and fault evolution, it may also improve the understanding of structurally controlled fluid flow in volcaniclastic reservoirs/aquifers.

Acknowledgements

This MSc. thesis is a part of my master's degree in Structural Geology at the department of Earth Science at the University of Bergen. Fundings for this project has been provided by BKK through the BKK-UiB agreement.

First and foremost, I would like to thank and express my sincere appreciation to my supervisor, Prof. Atle Rotevatn, for his guidance and motivation during my master's degree. I am so grateful for his will to share knowledge, humour and positivety. Thank you so much for constructive feedbacks and for always being available, despite the fact that you have been on the other side of the globe for the last year. I would also like to express my gratitude to my co-supervisor Prof. Thibault Cavailhes (University of Bordeaux) for appreciated feedbacks and guidance in the field and after. Thank you for inviting Martin Kjenes and I to Bordeaux last semester for an educational and fun "kick-off" week. In addition, I would like to thank Dr. Eivind Bastesen, Maria Marvik and Maria Ordemann for their contributions during the weeks of fieldwork in Taiwan.

Mr Wang and his wife at the "Sea Fan Guesthouse" is thanked for their hospitality during our two field seasons, and my friend Chung is thanked for his translations and good conversations during our stays in Taiwan. I am also grateful to Vilde Dimmen for introducing me to topology and teaching me ArcGIS. Moreover, a special thanks to Bjørn Nyberg and Casey Nixon helping me with the GT toolbox and teaching me how to use it. Christian Eide is thanked for his help and assistance regarding the makings of the virtual outcrops in *AgiSoft*. I also appreciate the help and guidance Irene Heggstad provided when operating the SEM. Ray Leadbitter at the Independent Petrographic Services in Aberdeen is acknowledged for providing exceptional thin sections.

Thanks to all my good friends at the University of Bergen for fun and memorable moments during the past five years. Special thanks to Mari, Mari N, Ane, Ida, Solveig, Knut, Sindre and Heidi for support the last couple of months. I want to thank my family and boyfriend, Mads, who have been so supportive, patient and caring during my time finalizing the thesis.

Finally, I especially want to thank my friend and field partner Martin Kjenes for fun and memorable field trips, for proof reading, good discussions and suggestions. I am so grateful for all your help and support. I would not have finished this thesis without you.

List of contents

1 INTRODUCTION

This study is one out of two related MSc projects studying deformation bands in volcaniclastic porous rocks on the eastern coast of Taiwan. Combined, the two projects aim to investigate and improve the understanding of the deformation mechanisms affecting volcaniclastics rocks at micro- and macroscale. While the focus of this thesis is the evolution and architecture from deformation bands into faults in volcaniclastic rocks, the focus of the sister MSc project by Martin Kjenes (Kjenes, 2018) was the microstructure and deformation mechanisms of different types of deformation bands.

1.1 Rationale and background

Fault zones are generally viewed as consisting of a fault core, which accommodate the majority of the displacement, and an enveloping damage zone with secondary deformation structures (Caine et al., 1996). The growth and development of fault zones in porous sandstones has been a subject for discussion for decades (e.g. Antonellini et al. 1994; Shipton and Cowie, 2001; Schultz and Siddharthan, 2005; Fossen et al. 2007; 2018), from the time when Aydin and Johnson (1978) first identified a consistent sequential evolution in which deformation bands develop into faults with increasing displacement. Deformation bands are thin tabular structures of strain localisation, formed in porous and granular rocks due to stress failure (Aydin, 1978). The complexity and growth of deformation bands are related to the displacement they accommodate (Shipton and Cowie, 2001) as the number of strands are commonly proportional with the displacement within a deformation band zone (e.g. Mair et al. 2000). Temporal and spatial evolution of faults may be elucidated by comparing small-offset structures with large-offset structures (Aydin and Johnson, 1978; 1983). Both deformation bands and faults are known to affect fluid flow in the subsurface as they alter the porosity and permeability of their host rock (e.g. Caine et al., 1996; Fossen and Bale, 2007). Consequently, it is important understand these structures and their spatial relationships in time and place as it could have implications for hydrothermal energy recourses, utilization and exploration of hydrocarbons, deep-waste deposition and ore deposits (e.g. Sibson et al., 1988; Stagpoole, 2001; Schutter 2003; Hawkins, 2004; Rohrman, 2007; Oelkers and Cole, 2008; Walker et al., 2013). Recently, also deformation bands and their progressive evolution into faults in porous and granular carbonates have been documented and characterised (e.g. Tondi et al. 2006: 2012; Cilona et al., 2012)

Volcaniclastic rocks may serve as reservoir rocks for groundwater, hydrothermal energy, hydrocarbons and are potential storage sites industrial made greenhouse gasses and nuclear waste (e.g. Neeper and Gilkeson, 1996; Sruoga and Rubinstein, 2007; Feng, 2008; Lenhardt and Götz 2011). It is therefore of great importance to understand the structure and evolution of faults in such rocks. However, limited work has been done on deformation bands and faults in porous volcaniclastic rocks (e.g. Wilson et al., 2003; Evans and Bradbury, 2004; Okubu, 2012). Notably, we know of no previous studies that attempt to elucidate the evolution of deformation-band-dominated faults in porous volcaniclastic rocks, probably because deformation bands themselves in volcaniclastic rocks have not been extensively studied. It is the aim of this outcrop-based study to contribute to filling this knowledge gap.

1.2 Aims and Objectives

This project sets out to increase the knowledge of fault evolution in volcaniclastic rock and to better understand the factors controlling fault zone architecture. More specifically, this thesis aims to i) to investigate the sequential development of deformation-band dominated faults in volcaniclastics, from deformation band to fully developed fault, ii) to document and examine lithological and structural controls on deformation band and fault zone architecture, and iii) to better understand structurally controlled fluid flow in volcaniclastics. The aims are achieved by an outcrop-based study in volcaniclastic rocks in Eastern Taiwan, addressing the following objectives:

i) Document and quantify the geometry, structure and displacement variations along deformation bands and faults in volcaniclastic rocks.
ii) Characterise fault zone architecture, and variability thereof, through geometrical and topological analyses.
iii) Microstructural and lithological investigations of rock samples from deformation bands, faults and host rock.
iv) Determine porosity, and any differences thereof, in deformation bands, faults and host rock.

1.3 Study area

The study area is located along the eastern coast of Taiwan (Fig. 1.1A), along a 1.5 km long stretch of coastal outcrops in the township of Shihtiping (Fig. 1.1B). Taiwan is positioned on an active convergent plate boundary where the continental margin of China collides with the Philippine Sea plate and the Luzon volcanic arc (e.g. Suppe et al., 1981; Barrier et al., 1986) The study area situated on the coastline of the Coastal Range, which is a mountain range originating from the relict and accreted Luzon Arc (e.g. Huang et al., 2000). The studied deformation bands and faults are hosted in a volcaniclastic succession of ignimbrites and tuff of the Miocene age (Song and Lo, 2002). The extremely well-exposed nature of the outcrops, and an abundance of exposed deformation bands and faults, make this an ideal study area for the present work. More details on the geology of Taiwan and the study area will be presented in Chapters 2 and 5.

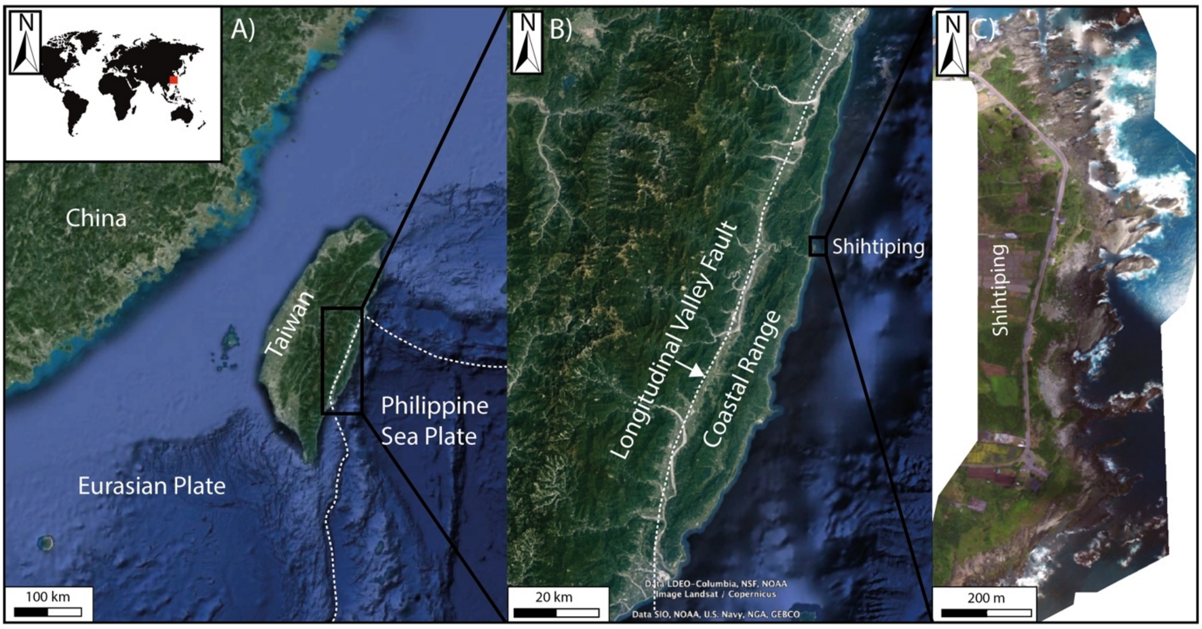

Figure 1.1: A) Satellite photograph of Taiwan and its location relative to China. Tectonic plates, and boundaries thereof, are marked. Inset map show where Taiwan is situated on the world map. B) Satellite imagery of the Coastal range. Longitudinal Valley Fault is highlighted, and the study area (Shihtiping) is outlined. C) Drone model of the coastal outcrops of Shihtiping where the field work was done.

2. GEOLOGICAL FRAMEWORK

This chapter presents the tectonic evolution of Taiwan and gives an overview of the regional tectonic framework of the island (Section 2.1). The main focus is on the eastern Coastal Range where the study is located (Section 2.2). A presentation of the local geology of the study area is provided in Section 2.3.

2.1 Regional tectonic framework

The island of Taiwan is located in southeast Asia, off the coast of southeastern China, separated from the mainland by the South China Sea. It is situated on the convergent plate boundary where the Philippine sea plate collides with the Eurasian plate. Taiwan island is the result of an active arc-continental collision, between the continental margin of the Eurasian plate and the Luzon volcanic arc (Barrier et al., 1986). The growing mountain belt is one of the world's youngest (Sibuet and Hsu, 2004). Taiwan is located in a highly complex compressional geological setting (Fig. 2.1), where the East-west trending Ryuku subduction zone is positioned to the east and the north-south trending Manila subduction zone (Fig. 2.1) is located to the south (Hsu, 1990). Oceanic lithosphere of the Eurasian plate is subducted beneath the Philippine Sea Plate (PSP) in the Manila subduction (Sibuet and Hsu, 2004), whereas at the Ryuku Trench the PSP is subducted under the Ryuku Arc. Subduction of the PSP in Ryuku Trench initiates back-arc extension in the Okinawa Trough and collapse of the Taiwanese orogen in the NE of Taiwan (Fig. 2.1) (e.g. Lallemand et al., 1999, 2001; Huang et al., 2000; Huang et al., 2006; Ramsey et al., 2007). The geology of Taiwan itself is strongly dominated by the collision of the continental margin of China and the accreted Luzon arc.

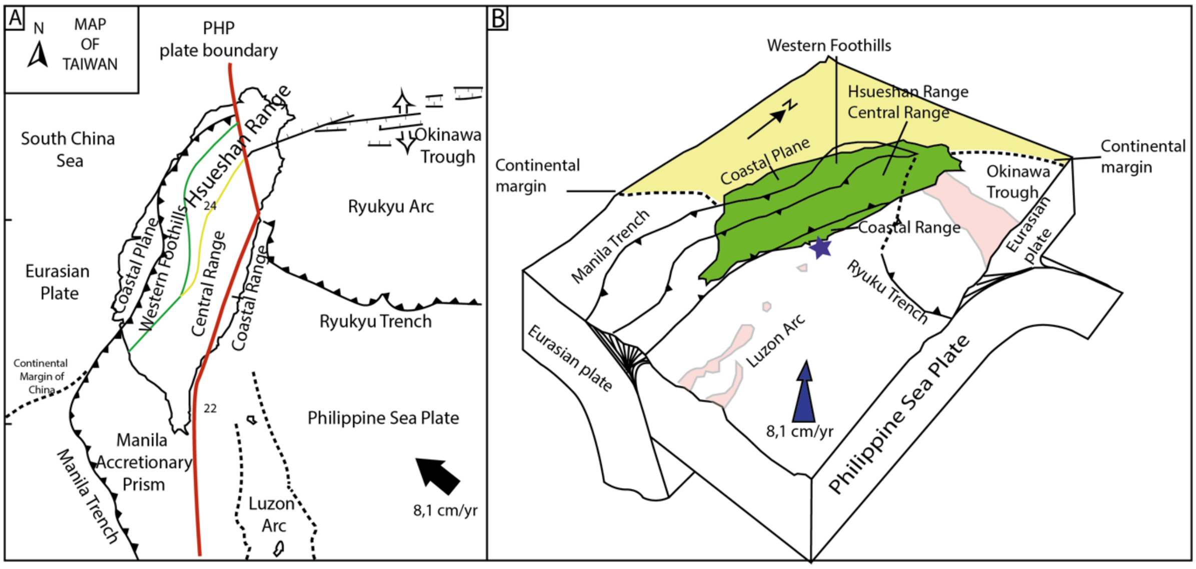

Figure 2.1: Location map of Taiwan showing the structural setting and an overview of the five tectonic domains; (1) the Coastal Plane to the west; (2) the Western Foothills; (3) the Hsueshan Range; (4) The Central Range and (5) the Coastal RangeFrom Chang et al. (2000). Arrows indicate the movement of the plates. The PH/EU motion collected form GPS data is 81 mm/year (Yu et al., 1997). Modified from Sibuet and Hsu (2004) and Pathier (2003). B) A block diagram that illustrates Taiwan's geodynamic setting in 3D. The star separates the full-stage arc-continent collision in the north, where the Luzon arc collides with the Chinese continental margin, from the initial stage further south, where the oceanic crust of the margin of china is subducted under the PH sea plate (Huang, 2006; Ramsey, et al., 2007). Modified from Ramsey et al. (2007).

The continental margin of China is oriented SW-NE, which makes the margin obliquely orientated relative to the Luzon Arc (N-S trending) and the convergent collision zone. This has resulted in a step-wise progression of the collision zone, as the collision initiated in the north and has progressed towards the south (Teng, 1990; Malavielle et al., 2002; Sibuet and Hsu, 2004). Consequently, the northeastern part of Taiwan is in a phase of orogen collapse, the central part of Taiwan is characterized by active collision and mountain building, while southern part, including Manila Subduction zone, is in a pre-collisional phase. Huang et al. (2000; 2006) presented a model that subdivides the evolution of Taiwan into four phases based on the tectonic processes that dominates the time and place; (I) Intra-oceanic Subduction, (II) Initial Arc-Continent Collision, (III) Advanced arc-continent collision and (IV) Arc Collapse and Subduction. The subdivision (Huang et al., 2000; 2006) will be used in the following and is illustrated in Figure 2.2.

(a) 12 Ma : Intra-Oceanic Subduction Stage (or present south of 21° N)

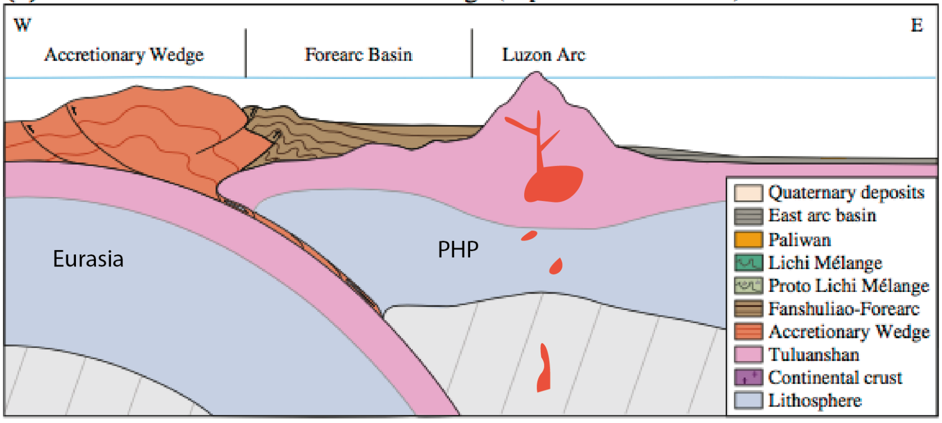

(b) 5 Ma : Initial Arc-Continent Collision (or present 22° 2'N)

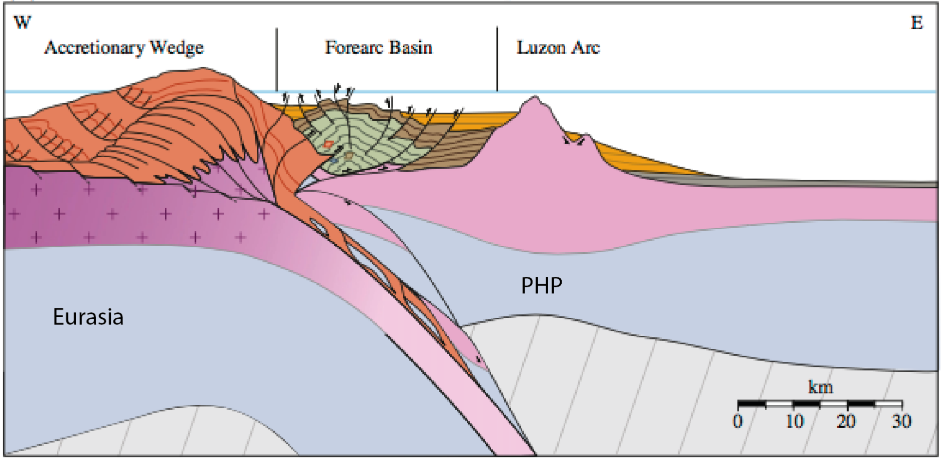

(c) Present : Advanced Arc-Continent Collision (or present north of 23° N)

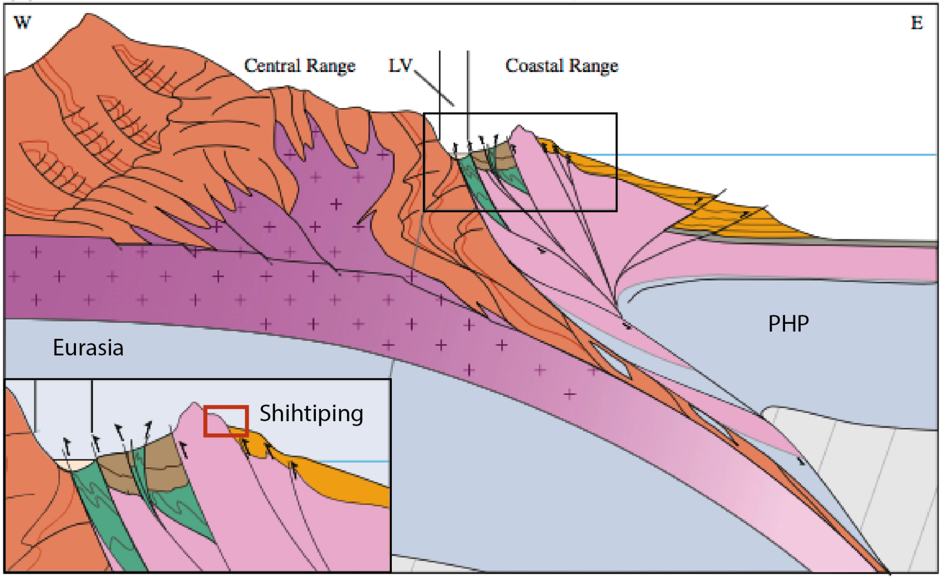

Figure 2.2: A schematic overview of the sequential evolution of Taiwan, and the current situation from north to south. The blue line represents the sea level. LV: Longitudinal Valley A) Intra- Oceanic Subduction stage. Volcanism and creation of the Luzon Arc and Manila accretionary prism. B) Initial arc-continent stage. C) Advanced arc-continent collision and the current tectonic setting of the eastern and central Taiwan. The inset photo illustrates the tectonic situation for the Coastal Range. Red square indicates approximately tectonic location of the study area. See text for further explanation. Modified from Thomas et al. (2014)

Intra-Oceanic Subduction

A plate reorganization around 15 Myr ago (Wolfe, 1981; Sibuet and Hsu, 2004) gave rise to the Manila subduction zone. Subsequently, the eastward subduction of the Eurasia margin under the PHP initiated. Volcanism related to the subduction zone established the Luzon Volcanic Arc and accretion of marine sediments created the Mainila accretionary prism and a forearc basin. Age dating done in the volcanics of the former Luzon Arc yielded ages of 15-16 Ma. This is interpreted to represent the age of onset of Luzon Arc volcanism (Yang et al., 1988 and 1995; Huang et al., 2006). Today the intra-oceanic subduction stage is found south of 21° 20'N and north of 19°N and near the Luzon Island (Huang et al., 2000; Thomas et al., 2014). The intra-oceanic subduction stage is comprised of an arc-trench system consisting of the Luzon Arc, a forearc basin, Manila accretionary prism and the Manila Trench among other provinces (Fig. 2.2a) (Huang et al., 2000).

Initial Arc-Continent Collision

The collision between the continental margin of Eurasia and the Luzon Arc occurred in the late Miocene between 12 to 5 Myr (Teng, 1990; Huang et al., 2000) as the subduction consumed oceanic lithosphere of the South China Sea which brought the continental margin of China closer. The initial arc-continent collision phase is characterised by narrowing and closing of the Luzon Arc forearc basin, in addition to the initial deformation of the forearc sediments (Huang et al., 2000; 2006). Moreover, this stage is characterised by eastward back-thrusting of the forearc sediments, an onset of a future suture zone of separate terrains, tectonic uplift and, lastly, termination of volcanic activity. Three volcanic islands started to accrete on to the Eurasian continental shelf, the eastern margin of proto-Taiwan (Huang et al., 2006). These have an age ranging from 8 to 3.3 million years (Chi et al., 1881; Yang et al., 1988; Huang et al., 2006; Thomas et al., 2014) and represent a shift from subduction to collision (Huang et al., 2006). Today the initial arc-continent collision stage is seen from 21°10'N to 22°40'N, just off the southern coast of Taiwan (Huang et al., 2000; 2006). See figure 2.2 B for illustrations of this stage.

Advanced arc-continent collision

The advanced arc-continent collision initiated 1.5-1 million years ago (Chi et al., 1981; Lee et al., 1991; Huang et al., 2006). It started when the Luzon arc, including associated sedimentary basins, was thrusted and accreted on to the margin of Eurasia. In the Coastal range in eastern Taiwan is this zone characterized by a volcanic succession with east-dipping thrust faults (Fig. 2.2c). The advanced arc-continent collision region is today located between 22°40'N and 24°N. It therefore dominates the geology of Central Taiwan. The Longitudinal Valley divides the Costal range and the Central range, and it is also where the boundary between Luzon arc, PSP, and the Eurasian continent is located (e.g. Angelier et al., 1997), see Figure 2.2c.

Arc Collapse and Subduction

The northernmost part of Taiwan, north of 24° N, is a transitional domain, from a regime characterized by contraction, to a regime where the driving forces are extension (Angelier et al., 1986; Shyu et al., 2005; Ching et al., 2011). Normal faults and strike-slip faults replace the reverse thrusts from the domain further south. This transition is related to the opening of the Okiwana trough (Chin et al., 2016) and subduction of the Luzon arc in the Ryukyu Trough (Huang et al., 2006). The subduction of the PSP contributes to the collapse of the Taiwan orogeny (Huang et al., 2012).

2.2 Tectonic domains of Taiwan

Taiwan can be divided into roughly five NNE-SSE trending tectonic domains (Huang et al., 2000; 2006). The tectonic domains represent the geological evolution of Taiwan which is dominated by mountain building and accretion. From west to east; the Coastal plane, the Western Foothills, the Hsuehshan Range, the Central Range and the Costal Range (Fig 2.1) (e.g. Chen et al., 2001; Brown et al., 2012; Huang et al., 2012). A fold and thrust belt is formed in the western part of Taiwan and includes The Coastal Plane, Western Foothills and Hsuehshan Range; these are all of Eurasian continental margin affinity. The Central Range is comprised of the uplifted, pre-collisional accretionary prism (Lin et al. 2003). Lastly, the Coastal Range, where the present study area is located, is made up by the accreted Luzon arc upon the Eurasian margin and include island arc volcanics and volcaniclastics, as well as associated forearc basins (Huang et al. 2012).

2.3 Coastal Range

The Coastal Range represents the accreted Luzon arc, following the arc-continent collision between the Luzon Arc and the continental margin of China (e.g. Ho, 1988; Sibuet and Hsu, 2004; Malavielle and Trullenque, 2009). It is situated on the PSP and consist of pre- to syncollisional volcanics, volcaniclastics and sediments of the former Luzon Arc and the basins around it (e.g. Thomas et al., 2014). The Coastal Range is about 150 km long and 15 km wide and is bound by the Longitudinal Valley in the west and the Pacific Ocean in the east. The Longitudinal Valley Fault is a sinistral oblique thrust fault (Fig 2.3) (e.g. Teng and Wang, 1981; Angelier et al., 1997; Hsu and Burgmann, 2006), where the Coastal Range is juxtaposed against the metamorphic basement of the Central Range. The Coastal Range is interpreted to include several volcanic islands with associated forearc basins and two intra-arc basins (Chang et al., 2000; Huang et al 2000; 2006; Thomas et al., 2014). Based on lithology, the Coastal Range is divided into the Tuluanshan formation, the Fanshuliao formation, the Paliwan formation, the Lichi Mélange and the Pinianshan Conglomerate (Teng and Wang, 1981; Thomas et al. 2014). See Figure 2.3 for more information about the Coastal Range and distribution of the formations. Within the study area (Shihtiping), the Tuluanshan Formation is the interval if interest in this study, and is described in the following.

Tuluanshan Formation

The Tuluanshan formation has been dated to be 16.6 to 5 Ma and is considered to be the oldest formation of the Costal Range (Fig. 2.3) (Song and Lo, 2002; Thomas et al., 2014). The formation represents a volcanic sequence of several accreted volcanic islands. They form the basis for the division, from north to south; Yuehmei pyroclastics, Chimei-, the Chengkuangao- and the Tulunashan igneous complex (Huang et al., 2006: Lai et al., 2014; Thomas et al., 2014; Chen et al., 2017). The volcanic islands started to erupt in submarine environments and gradually rose from the deep marine conditions to subaerial exposures (Lai and Song, 2013). Consequently, the Tuluanshan formation is comprised of a variety of volcanics and volcaniclastic rocks with andesitic origin. It includes andesitic breccia, agglomerate, lava flows, dikes, tuffaceous conglomerates and sandstones from the former Luzon Arc (Hsu, 1956; Teng and Lo, 1985; Song and Lo., 2002; Thomas et al. 2014; Chen et al., 2017). Also, reefal limestones are found in the upper part of the formation, which originates from fringing reefs which developed around the volcanic islands when the islands were subaerially exposed (Huang et al., 1988 Song and Lo, 2002). The Tuluanshan Formation can be further divided into three members; The Shihtiping Tuff, the Shihmen Breccia and the Kangkou Limestone (Song and Lo, 2002). Shihtiping and the study area is located in the Shihtiping Tuff member, which encompasses the subaerial exposed parts of the Chimei igneous complex.

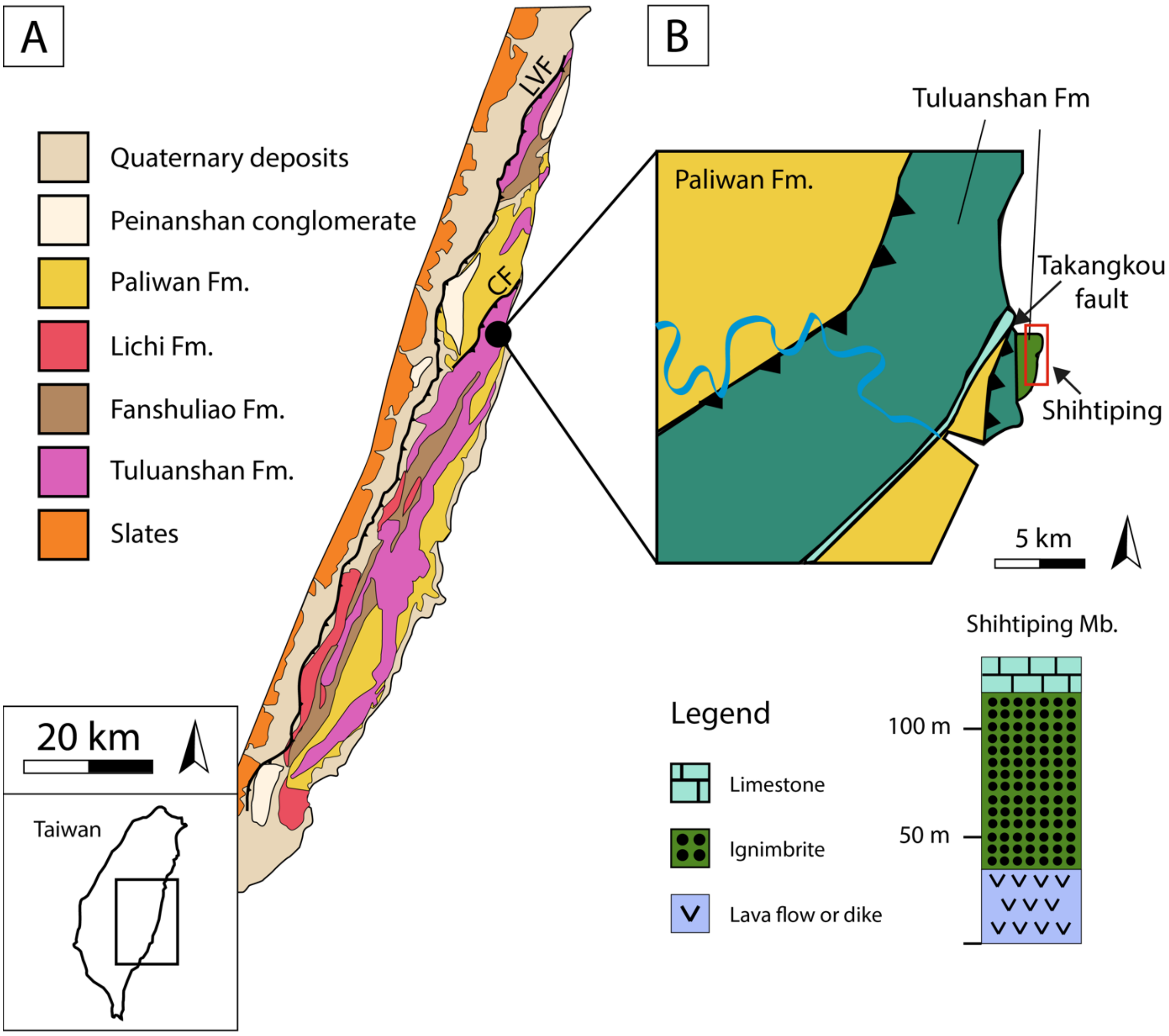

Figure 2.3: A) A geological map over the Coastal Range. The study area is outlined in red. Modified after Thomas et al. (2014). LVF: Longitudinal Valley Fault. CF: Chimei Fault B) Geological map of Shihtiping and the surrounding area, together with an illustration of the previous log of the study area by Song and Lo (2002). The study area is outlined in red. Modified after Song and Lo (2002) and Lai and Song (2013).

2.3.2 Study area and the Shihtiping Tuff

The Shithiping Tuff member is comprised of pyroclastic and volcaniclastic material. The upper part of this c. 100 metres thick section consists of a layered sequence of ignimbrites and crystalline tuff (Song and Lo, 1988; Song and Lo, 2002). The studied deformation bands dissect this upper ignimbritic unit, which is exposed along the Coast of Shihtiping. Age dating constrains the age of the youngest volcanic deposits in the member to c. 5.5 Ma (Lai and Song, 2013). The ignimbrites are poorly sorted and deposited by pyroclastic flows. The composition of the ignimbrites consists of volcanic glass fragments, well- to sub-rounded volcanic bombs and pumice, in addition to more angular lithic fragments and phenocrysts. Plastic deformation, impact- and welded structures are found in the pumice- and glass fragments, which indicates high temperatures during deposition. The ignimbrites are locally interbedded with polygenic volcanic breccias (Lai and Song, 2013)

The interbedded tuff layers are comprised of 55-80% crystal fragments, and some lithic clasts, within a groundmass of volcanic glass (Song and Lo, 2002). It is comprised of both thin and more massive ash layers and is interbedded with the ignimbrites. In these tuff beds, sedimentary structures such as parallel lamination and herringbone cross stratification are common features. The mineral assemblage in both the ignimbrite and the crystalline tuff are andesitic and consist off plagioclase, hornblende, hypersthene, augite and magnetite.

The tuff either originates from eruption of crystallized magmas, physical fractionation and sorting associated with pyroclastic eruption and transportation processes, or reworking and redeposition (Cas and Wright, 1988; Song and Lo; 2002). In other words, the tuff layers are consequences of, in air, grain size sorting during an eruption. While redeposition of eroded ignimbrites deposited in water, with significant amount of energy (e.g. tidal environments), may be the origin of the cross stratified tuffs. Song and Lo (2002) propose that the Shihtiping ignimbrites are formed in a subaerial environment, while the cross-bedded tuffaceous sandstone originates from a tidal environment. However, peperite volcanic bombs are also found in the ignimbrite layers, which indicate that the hot flow was deposited in water (Lai and Song, 2013).

The accretion of northern segment of the Luzon arc upon the Eurasian margin involved both folding and faulting in the area. The study area is comprised of a folded succession with folds striking towards NNE (Lin and Huang, 2014). The nearest mapped fault in the study area is the Takangkou reverse fault, located to the west of Shihtiping (Fig. 2.3) (Hsieh et al., 2004). Takangkou fault is striking NNE with a high angle dip of approximately 60° towards the east (Hsieh et al., 2004). Two conjugate sets of deformation band, respectively oriented ENE and WNW, are dissecting the folded sequence (Lin and Huang, 2014).

3. THEORETICAL BACKGROUND

This chapter reviews existing knowledge and terminology concerning deformation bands as well as the structure and evolution of fault zones in porous and granular rocks. Most of the published literature covers deformation bands in porous sandstones and carbonates, since less research has been dedicated to deformation bands and faults in volcaniclastic rocks. First, general characteristics of deformation bands and their classification will be reviewed in Sections 3.1-2. A summary of the existing literature on deformation band in volcaniclastics will be given in the following Section (3.3). This is followed by a description of fault evolution in porous granular rocks (Section 3.4), and the characteristics of fault zone architecture (section 3.5). Lastly, Section 3.6 will give an outline of fracture network characterisation by the use of topology.

3.1 Deformation bands in porous and granular rocks

The term deformation bands was first introduced by Aydin (1978) who described tabular mm-wide deformation structures in sandstones with displacement of a few millimetres to centimetres. Since then, the term has widely been used to describe strain location structures in porous sandstones (e.g. Aydin and Johnson, 1978; 1983; Antonellini et al., 1994; Fossen and Hesthammer, 1997; Soliva et al., 2013; Fossen et al., 2007; 2018). Deformation bands are generally cohesive structures with localized shear and/or may include volume changes. They can crop out as single bands, in clusters or in networks of bands (Aydin and Johnson, 1978). Pore space in granular rocks means such rocks are susceptible to different deformation mechanism compared to those mechanisms that dominated in low- to non-porous rocks; these mechanisms include grain reorganization (disaggregation, granular flow), cataclasis (grain comminution, cataclastic flow) and/or solution/precipitation to accommodate strain in form of a deformation band (e.g. Wong et al., 1997; Fossen et al. 2007). The formation of deformation bands in porous sandstones are generally thought to be associated with strain hardening (e.g. Aydin & Johnson 1983; Antonellini et a. 1994; Mair et al. 2000; Rotevatn and Fossen 2012) and alteration of the porosity distribution. Deformation bands typically display porosity reductions and permeability reduction from one to three orders of magnitude compared to the host rock (Antonellini and Aydin 1994; Fossen et al. 2007; Ballas et al., 2012). In contrast, non-porous rocks deform decidedly different as they accommodate strain by brittle fractures which generally leads to an increase in porosity and permeability (e.g. Fossen et al., 2007; 2018). In recent times, deformation bands have also been found in carbonates (e.g. Tondi et al., 2006; Cilona et al., 2012; Rotevatn et al., 2016) and volcaniclastic rocks (e.g. Wilson et al., 2003; Zhu et al., 2011; Okubu et al., 2012). Additionally, deformation bands are also investigated by laboratory experiments the last decades (e.g. Wong et al., 1997; Mair et al., 2000; Kaproth et al. 2010). Since porous and granular rocks also are good reservoir rocks, deformation bands are important to understand as they affect the pertrophysical properties (porosity and permeability) and therefore may alter the fluid flow within a reservoir (e.g. Fossen and Bale; Rotevatn et al., 2013; Fossen et al., 2018).

3.2 Classification

Deformation bands can be classified according to the main deformation mechanism or by the kinematics (Aydin et al., 2006; Fossen et al., 2007; 2018).

3.2.1 Mechanisms

According to Fossen et al. (2007) deformation bands can be classified by the most prominent deformation mechanism that forms them; 1) granular flow, 2) cataclasis, 3) phyllosilicate smearing and 4) dissolution and cementation. Classification of deformation bands can be done based on these mechanisms (Fig.3.1).

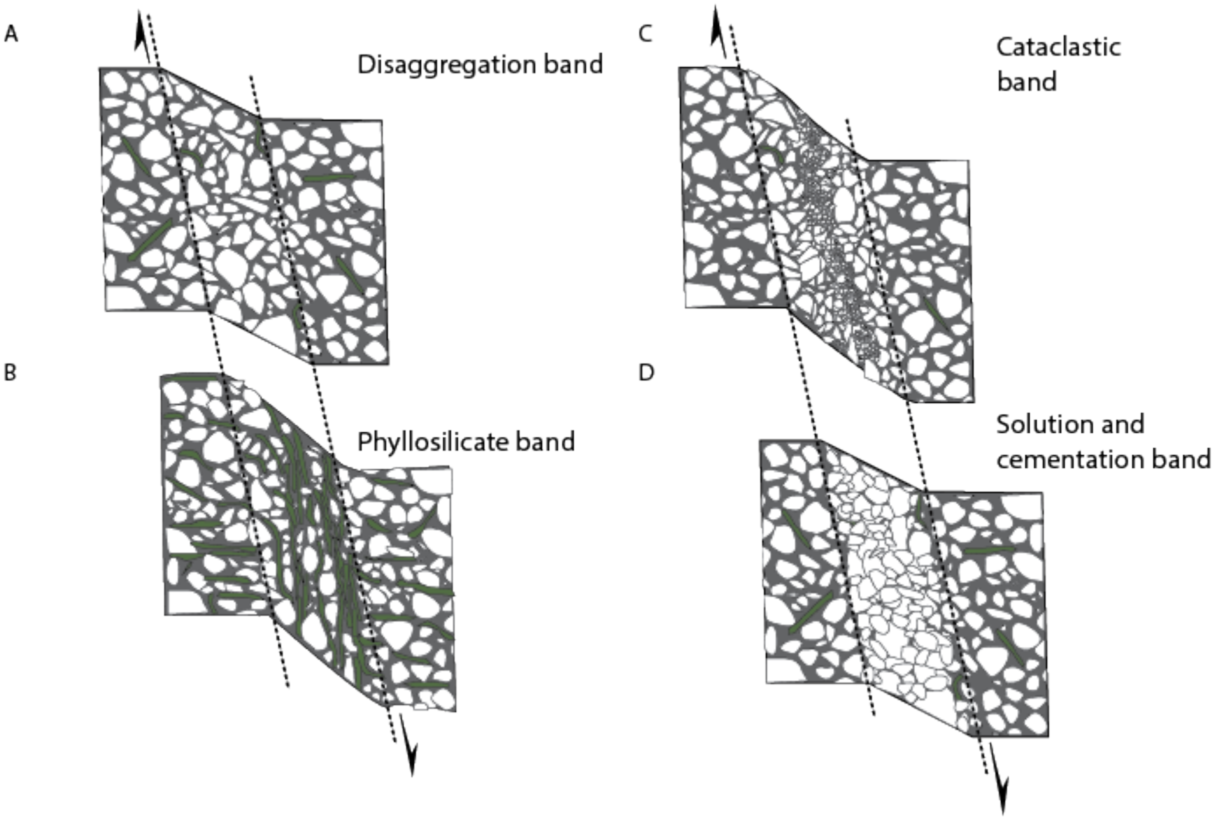

Figure 3.1: Classification of deformation bands based on the formation deformation mechanism. A) Disaggregation band formed by granular flow; translation and rotation. B) Phyllosilicate band formed in mica/clay bearing sandstone by alignment of phyllosilicates. C) Cataclastic bands formed due to grain crushing and fracturing resulting in e.g. grain size reduction. D) Solution and cementation bands formed as a result of dissolution and cementation processes. Slightly modified after Fossen et al. (2007)

*Disaggregation band*s (Fig. 3.1A) are formed by grain-reorganisation caused by granular flow (e.g. Twiss and Moores, 1992). This process includes breaking of grain-bounding cement, rolling, rotation and translation of the individual grains, and will often lead to compaction of the porous media (Fossen et al., 2007). There is little to no grain-size reduction in these kinds of bands. They commonly form at shallow burial depths (less than 1 km) in unconsolidated, or weakly consolidated, sediments (e.g. Mandl et al. 1977, Hesthammer and Fossen, 2001; Fossen et al., 2018). However, overpressure may enhance disaggregation at deeper burial depths (Fossen et al., 2018). Disaggregation bands may act as a conduit for fluid flow (du Bernard et al 2002; Antonellini et al 1994) which is especially true for dilation bands. Others (e.g. Molemma and Antonellini, 1996; Fischer and Knipe, 2001) have reported of a small reduction in permeability in disaggregation bands. Nevertheless, the effect of disaggregation bands on fluid flow is trivial (Knipe et al., 1997).

Phyllosilicate bands (Fig. 3.1B) only occur in rocks that contain a certain amount (14%-40%) of mica/clay minerals (Knipe et al., 1997; Fisher et al., 2000). These bands forms when elongated phyllosilicate minerals rotate and align themselves parallel to the band by granular flow and grain boundary sliding (Fossen et al., 2007). Phyllosilicate bands decrease the fluid flow as aligned elongated mica crystals represent a barrier that reduces the permeability and porosity. As the deformation mechanism is the same as disaggregation bands, they often are considered as a sub-group of these.

Cementation and solution bands (Fig 3.1D) forms as dissolution and/or cementation take place along deformation bands during, or after, deformation (Fossen et al. 2007). They are recognised as tightly packed zones with a grain size smaller than the matrix (Gibson 1998; Fossen 2007). Dissolution is associated with chemical compaction or pressure solution and is in sandstones promoted by high temperatures (90°C) at greater burial depth than 3 km and/or clay minerals (Walderhaug, 1996; Fossen et al., 2007). It is suggested by Tondi et al. (2006) and Cilona (2012) that pressure solution is a more prominent deformation mechanism in carbonates than in sandstones. Cementation and precipitation are at its most active on newly fractured and exposed grain surfaces, where the grains are coated with illite (Storvoll et al. 2002) or chlorite (Ehrenberg 1993) and in tensile fractures (Leveille et al. 1997; Fossen et al., 2007).

Cataclastic bands (Fig 3.1C) form when applied stress leads to grain fracturing and grain crushing. Grain-reorganisation is also accompanied in such a process. Cataclastic bands are distinguished by a compact zone where the pore space and grain size are reduced. Aydin (1978) divided cataclastic bands into two zones; (1) An inner zone characterised by absence of pore space, poorer sorting, more matrix and fractured, angular grains, and (2) an outer zone that is more compact than the host rock and have less fractured grains than the inner zone. Fossen et al. (2007), refer to this outer zone as the transition zone. Compaction, grain-reorganisation and cataclasis in these bands causes grains to interlock and subsequently become harder to move, initiating a strain hardening effect Aydin, 1978; Fossen et al., 2007). Rotevatn et al. (2008) described slipped cataclastic bands in the Suez rift, Egypt, which is defined by intense cataclasis, smaller amount of compaction and a central slip surface with localised shear. If present, slipped deformation bands represent the final stage of the evolution of a cataclastic deformation band and may be the precursors for faults (Fig. 3.2) (Rotevatn et al., 2008). Cataclastic bands in porous sandstones are associated with burial depth greater than 1.5 km, but in contractional regimes they can occur at shallower depth, as the mean stress increases (Solvia et al., 2013; Fossen et al., 2018).

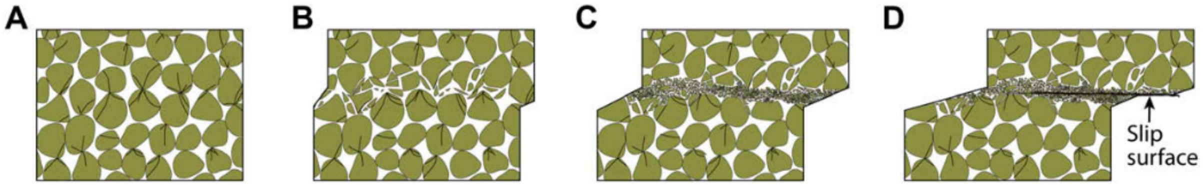

Figure 3.2: Schematic illustration of the evolution of a slipped cataclastic band: A) Grain fracturing at grain contacts due to increased stress. B) Mild cataclasis and the initial configuration of a cataclastic band. C) Shear causes progressively more cataclasis. D) A slip surface develops after continued shear and cataclasis. From Rotevatn et al. (2008).

The dominant deformation mechanism is dependent of the host rock properties and external conditions (listed in Fig. 3.3B). External conditions including confining- and pore-fluid pressure and tectonic regime, which all affect the way porous media deform over time (Fossen et al., 2007; 2018). Shallow burial depth provides low confining pressure which again promotes disaggregation. At shallow depth, less stress is transmitted through grain contacts and the grains can easily move relatively to each other. Consequently, higher confining pressure at deeper burial depth will enhance cataclasis. Meanwhile, high fluid pressure relieves stress on grain contacts points, counteracting confining pressure and favoring disaggregation as the dominant deformation mechanism (Fossen et al., 2007; 2018). Tectonic stress influences the deformation mechanism as it causes the mean stress to change. Contractional regimes increases the mean stress and following cataclasis, whereas in extensional regimes, the mean stress is decreased, promoting disaggregation (Solvia et al 2013; Fossen et al., 2018). In addition, relatively constant internal properties within the rock like sorting, grain size and shape, mineralogy, coating on grains and porosity influence the style of mechanism (Fossen et al., 2007). A well-sorted and rounded sandstone has few and small grain contacts, compared to a poorly sorted sandstone with angular clasts, and will therefore be prone to cataclasis as more stress will be transmitted through these grain contacts (Gallagher et al., 1974; Cheung et al. 2012; Fossen et al. 2018).

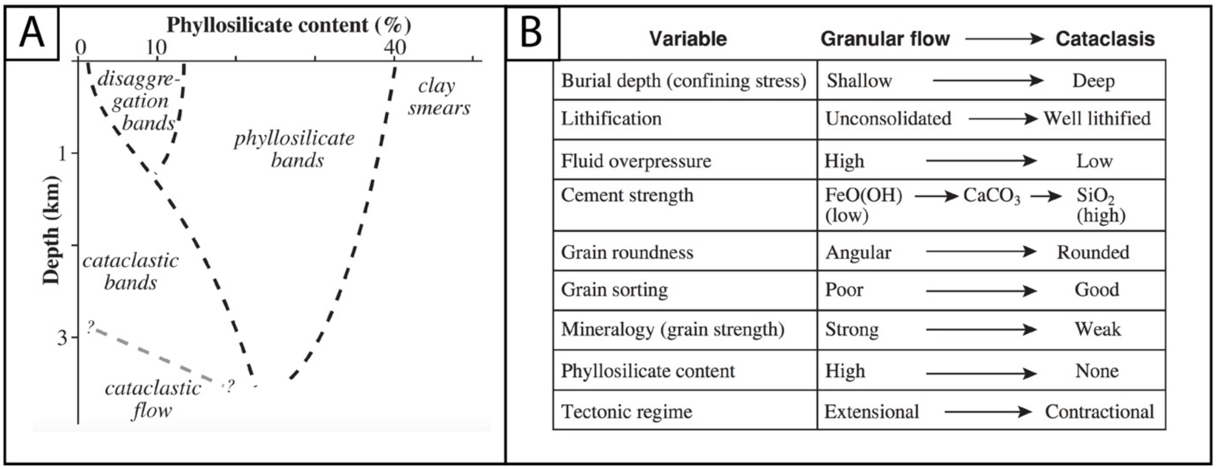

Variable	Granular flow ⟶ Cataclasis
Burial depth (confining stress)	Shallow ⟶ Deep
Lithification	Unconsolidated ⟶ Well lithified
Fluid overpressure	High ⟶ Low
Cement strength	FeO(OH) (low) ⟶ $CaCO_3$ ⟶ SiO_2 (high)
Grain roundness	Angular ⟶ Rounded
Grain sorting	Poor ⟶ Good
Mineralogy (grain strength)	Strong ⟶ Weak
Phyllosilicate content	High ⟶ None
Tectonic regime	Extensional ⟶ Contractional

Figure 3.3 A) Figure that show the relationship between burial depth and phyllosilicate content. B) Table presenting some of the controlling factors of the degree of cataclasis. Form Fossen et al. (2018)

3.2.2 Kinematics

Deformation bands can also be classified according to kinematics (Aydin et al., 2006). Based on kinematics, deformation bands can be divided into three end-members: simple shear bands, dilation bands and compaction bands (Aydin et al., 2006; Fossen et al., 2007; 2018). Simple shear bands have displacement parallel to the band and show no volume change. Pure compaction bands and pure dilation bands shows displacement perpendicular to the band and include volume changes. The tree end-members are, however, relatively rare (Mollema & Antonellini 1996; Du Bernard et al. 2002; Fossen et al. 2018). Most observed deformation bands are hybrids of these end-members (Fig. 3.4) and fall in between shear bands and compaction bands, but often closer to shear bands (Fossen et al., 2018). Compactional shear bands (CSB), refer to bands with band-parallel movement that additionally involve a small amount of compaction (Fossen et al., 2018). CSB often form conjugate sets that cross-cuts one another (Chemenda et al., 2014).

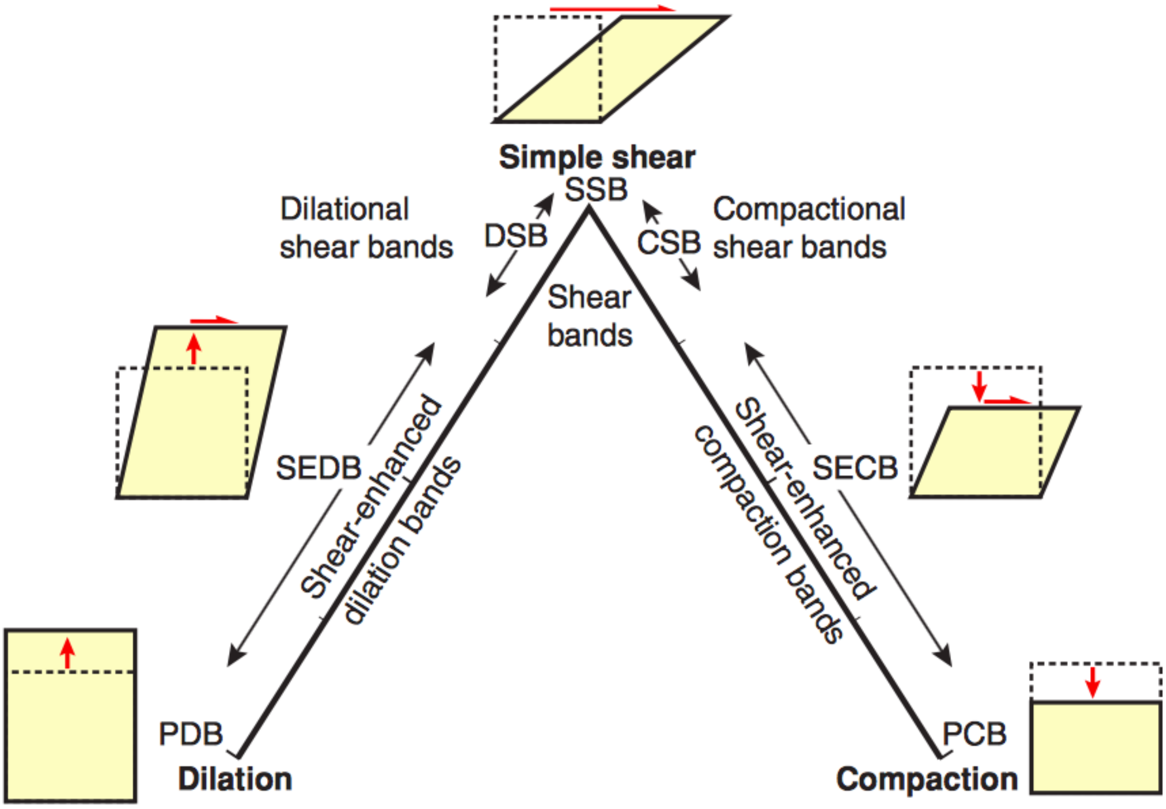

Figure 3.4: Kinematic classification of deformation bands. PCB=Pure compaction bands; PDB=Pure dilation bands; SSB=Simple shear bands; SEDB=Shear-enhanced dilation bands; DSB=Dilation shear bands; CSB=Compactional shear bands; SECB=Shear-enhanced compaction bands. (From Fossen et al., 2018)

3.3 Deformation bands in volcaniclastics

Although deformation bands in siliciclastics, and, to some extent, carbonates, have been extensively studied, less work have been done on deformation of porous and granular volcaniclastic rocks (Soden and Shipton, 2013). Cas and Wright (1987) define the term volcaniclastics as any fragmental aggregate of volcanic parentage, irrespective of origin. The term includes both pyroclastic- and epiclastic deposits. Deformation bands in volcaniclastics usually are found in non-welded tuffs and ignimbrites (e.g. Wilson et al., 2003; 2006; Evans and Bradbury, 2004; McGinnis, et al., 2009). Ignimbrites are pyroclastic deposits made primarily of pumiceous material, phenocrysts and lithic clasts in a matrix of ash from a concentrated, hot particulate flow (Walker 1983; Freundt et al., 2000), whilst tuff is ash deposits with a grain size smaller than 2 millimetres (Fisher, 1961; Cas and Wright, 1987). Tuffs and ignimbrites are often high-porosity rocks (Moon, 1993; Fisher et al. 2006), which make them suitable as hydrothermal and hydrocarbon reservoirs and groundwater aquifers (e.g. Schutter, 2003; Magara, 2003; Lenhardt 2015).

A few studies have been carried out regarding faults and deformation bands in volcaniclastics. (e.g. Dawers and Anders, 1995; Ferril et al., 1999; Wilson et al., 2003; Evans and Bradbury, 2004; Zhu et al. 2011). The broad consensus is that porosity and the degree of welding (sintering of hot glassy particles (e.g. Quane and Russel, 2005) of the volcaniclastic deposits is the primary controlling factor of the mode of failure and mechanical strength (Moon 1993b; Wilson et al. 2003; Evans and Bradbury., 2004; Zhu et al. 2011). Rocks with a low degree of welding and high porosity will mainly deform as deformation bands, whereas welded rock units tend to form fractures and faults during deformation (Wilson et al 2003; Riley et al., 2010). Secondary control mechanisms include post-depositional crystallisation of volcanic glass into crystals that reduce pore space, which again strengthen the mechanical strength of the rock and enhance brittle deformation (Wilson, 2003; 2004). In addition, grain size and shape, density of microcracks, presence of clay, lithophysae and water will influence the properties of volcaniclastics (Moon, 1993a; Wilson, 2003; Avar and Hudyma, 2007; Zhu et al. 2011).

Deformation bands in volcaniclastics are in many ways similar to the deformation bands found in porous sandstone (Mcginnis, (2009). However, there are still limited knowledge regarding the involved deformation mechanisms at work, and how deformation bands evolve in these rocks (Cavailhes and Rotevatn, accepted). Deformation processes as grain crushing, compaction, grain boundary sliding, and shearing is reported from deformation bands in tuffs and ignimbrites (Wilson et al., 2006). Two different explanations for the initiation of the above-mentioned cataclastic processes is proposed. Either cataclasis will initiate around pores in a process of cataclastic pore collapse (Zhu et al., 2011), or in the weak glassy matrix (Wilson et al., 2006). Cataclastic pore collapse is unlike to what have been observed in sandstone, where cataclasis is initiated at grain contacts. Additionally, the damage zone in ignimbrites differ from what is observed in sandstones, as large clusters of deformation bands are rarely observed close to the fault (Riley et al., 2010).

3.4 Fault evolution in porous granular rocks

Several studies concerning fault evolution in porous sandstones have been carried out (e.g. Aydin and Johnson, 1983; Antonellini and Aydin 1994; Shipton and Cowie, 2001; Rotevatn and Fossen 2012; Nicol et al., 2013). As mentioned, compaction and pore space reduction both occur as a porous rock is exposed to stress (Fig 3.4, stage A), which leads to a process of strain hardening due to more grain-contacts and increased friction at these contacts (Aydin and Johnson, 1983). At this initial stage the grains will interlock with one another and cataclasis can initiate as fractures at the grain contacts (Fig 3.4, stage B). As cataclasis and compaction causes a strain hardened zone in the existing deformation band, a new deformation band might nucleate adjacent to the previous one in an undeformed zone with grains that are still easy to move. Eventually, as the process continues a cluster, or a network of deformation bands may form. The occurrence of clusters causes strain hardened networks which can be up to tens of centimetres wide and over hundreds of metres long (Philit et al., 2017). Faults in porous sandstones form in connection with these networks and clusters (Fig. 3.4) and are a response to strain hardening. Shipton and Cowie (2001) suggest that a slip surface first nucleates in localised zones within, or at the margin off, the cluster (Fig. 3.4, stage C), which eventually propagate and link up to form a through-going slip surface (Fig. 3.4, stage D). Once a fault plane is formed, the process of strain hardening is replaced by strain softening as the shear resistance in the rock decreases with a through-going fault plane (Fig. 3.4, stage D) (Rotevatn and Fossen, 2012). The displacement now continues as frictional slip at the slip surface. As a result, the damage zone of faults in porous granular rocks are generally comprised clusters of deformation bands generated prior the progradation of a slip surface. However, investigations done by Schueller et al. (2013) show that the damage zone continues to develop after the establishment of a fault plane, as displacement accumulates.

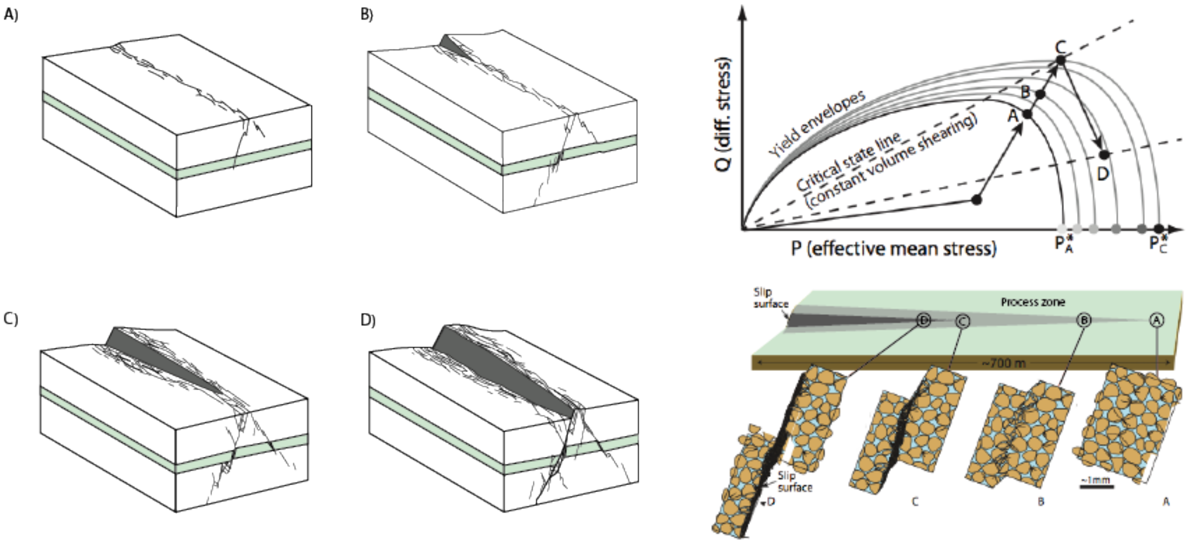

Figure 3.4 Block diagram on the left side: Schematic sketch of the evolution of a fault in porous sandstones. A) Formation of deformation band clusters, patches slipped deformation bands can occur. Deformation happens within deformation bands. B) A thoroughgoing slip surface have started to nucleate from the fault tip. Deformation bands in the process zone increase in density and isolated slip surfaces may develop. C) The slip surface develops to a more thoroughgoing fault where most of the displacement takes place. Some deformation bands are still generated in the damage zone. D) A fully developed fault. The damage zone width

increases with the displacement. Modified from Shipton and Cowie (2001). Figure to the right: Displays the stages of fault evolution through a P-Q diagram (differential stress vs. mean stress) in the upper panel and the microstructural processes in the lower panel. The stages correlates to the stages in the block diagram. Upper panel: P*= Grain crushing pressure at the different stages. Stage A-C display the strain hardening process as the yield envelope get larger. Stage D represents the creation of the fault and strain softening. Lower panel: the microstructural processes at each stage connected to a fault. Modified from Rotevatn and Fossen (2012)

Standard displacement-length relationships for faults is correlated through the equation:

$$D_{\max} = \gamma L^n,$$

Where $D_{\max}$ is the max displacement, γ is depending on the rock properties, L is the length of the fault and n is normally around 1 (Cowie and Scholz 1992a; 1992b; Schultz et al., 2008). However, n will be close to 0.5 for deformation bands due to the deformation mechanism and strain hardening (Schultz et al 2008; Rotevatn and Fossen, 2012). How the D/L-relationship change through the evolution from deformation bands to the generation of a fault is effectively illustrated in Figure 3.5.

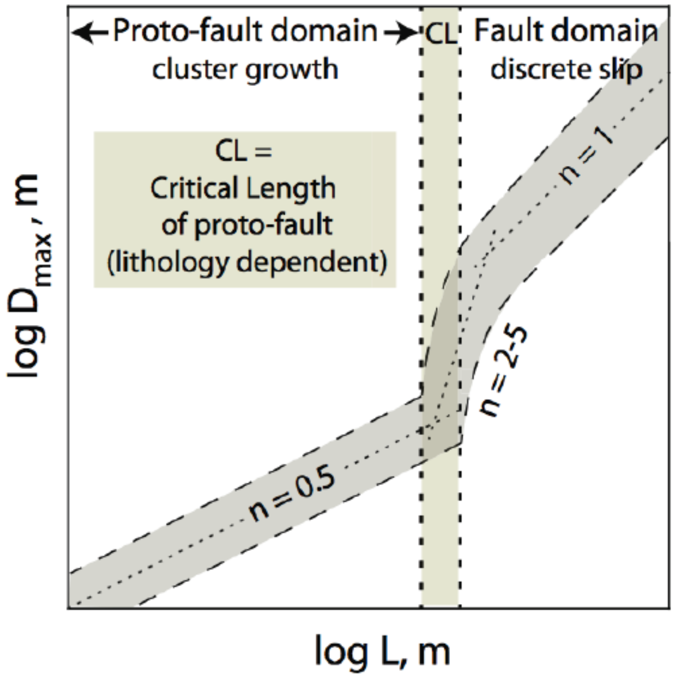

Figure 3.5: The diagram displays an simplified D/L relationship for deformation bands and faults in porous sandstones. From Rotevatn and Fossen (2012).

Deformation bands and fault evolution in porous sandstones have mostly been studied in extensional regimes (Aydin and Johnson, 1993; Shipton and Cowie 2001; Fossen et al., 2018), and less studied in contractional regimes. However, studies indicate that the population of deformation bands in contractional regimes are more evenly distributed than the more densely populated zones of deformation bands in extensional regimes (e.g. Fossen et al 2016; Soliva et al., 2016). Compactional shear bands tend to develop as conjugate sets with a dihedral angle of 35-95° in extensional regimes and with an angle of 40-75° in contractional regimes (Fossen et al 2018).

3.5 Fault zone architecture and nomenclature

A fault zone is comprised of a *fault core* containing one or several principal slip surfaces, cataclasites, gouges or breccias located within a *damage zone* of adjoining fractures (Caine et al., 1996; Schulz and Evans, 1998; Shipton et al., 2006; Childs, et al., 2009). Most of the displacement is accommodated by the fault core and the thickness of the fault core can display large variations along the strike and slip (e.g. Caine et al., 1996; Shipton and Cowie 2001). Larger faults are the outcome of linkage of single faults and form as the fault segments grow and interact (Walsh and Watterson, 1988; Peacock and Sanderson, 1991; Walsh et al., 2002; Childs et al., 2009). These linkage- and overlap zones between fault segments can be somewhere between (i) s*oft-linked* or (ii) *hard-linked* (Walsh and Watterson, 1988, 1991). The segments in (i) soft-linked faults appear to be isolated from one another, but strain and rotation within the rock volume between the segments testifies of fault interaction (Walsh and Watterson, 1991). When two fault segments are connected by visible, often smaller, faults is the fault called (ii) hard-linked (Walsh and Watterson, 1991; Peacock et.al. 2016). This terminology can also be used to name linking structures in deformation bands networks (e.g. Cruikshank et al., 1991; Fossen and Hesthammer 1997).

The damage zone can be defined as the volume of deformed wall rock related to a propagation, initiation and slip along fault. Damage zones develop in response to deformation variations along and between faults segments (e.g. Kim et al., 2004; Peacock et al., 2017). Kim et al., (2004) differentiate between tip damage zone, wall damage zone and linking damage zones (Fig 3.7), and by doing so includes process zones, horsetail tips, drag zones, relay ramps and linking structures in the different damage zones. Studies show that the development of the damage zone is highly dependent on lithology, especially for high-porosity rocks and low-porosity rocks (e.g. Wong et al.,1997; Shipton and Cowie 2003; Schultz and Siddharthan 2005; Johansen and Fossen, 2008). This highlights the importance of mechanical units attributes (e.g. thickness, stiffness, porosity) for fault zone architecture.

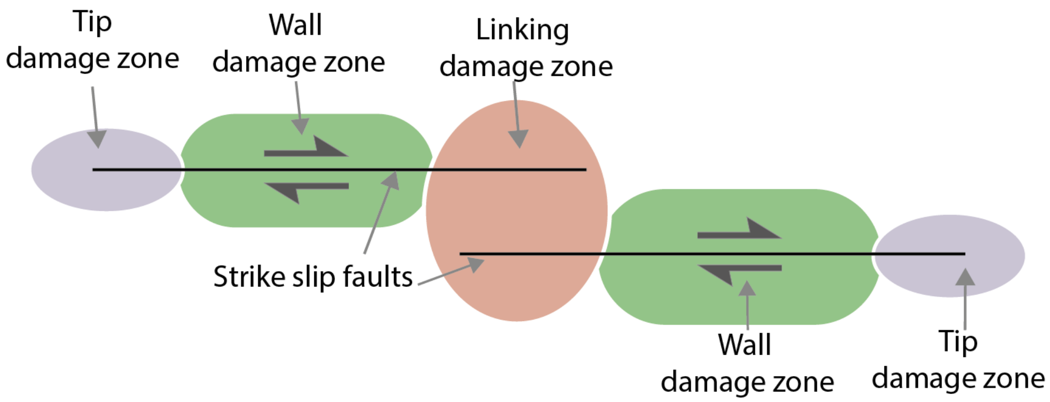

Figure: 3.7: Sketch of three damage zones in map view types related to two interacting fault segments.. Modified after Kim et al. (2004)

3.6 Fracture networks and the use of topology

Fracture network is where two or more fractures are linked and interact to form a network. The term *fracture* is used in this sub-chapter in its broadest sense and may includes any form of discontinuity as joints, faults and deformation bands (sensu Peacock et al., 2016). A fracture network can be described by its geometry as orientation, fracture length, spacing and intensity (Johnston and McCaffrey, 1996; Bonnet et al., 2001) or it can be described by its topology (Peacock et al., 2016). Topology is a method to characterise and visualise a fracture network. It was introduced by Manzocchi (2002) and later developed by Sanderson and Nixon (2015). Topology is a way to quantify the relationship between fractures of the same network in order to visualize geometry and measure fracture connectivity in a network. Quantifying connectivity is crucial as it provides parameters for assessing a reservoir potential for fluid flow (Manzocchi, 2002; Morley and Nixon, 2016). However, a majority of studies that have been conducted, use topology on joint and fault systems where high connectivity usually represents a more permeable zone (e.g. Dimmen et al., 2017; Procter and Sanderson, 2017). In contrast, deformation bands may act as a baffle for fluid flow and therefore, a zone of high connectivity within a network does not necessarily represents increased permeability (Fossen and Bale, 2007).

A fracture network can be divided into branches and nodes (Sanderson and Nixon 2015; Morley and Nixon, 2016). Branches are lines bound by two nodes and represent fractures or a line of discontinuity. Whereas nodes represent intersection points where two branches meet or the ending point of a branch. Three different nodes are used: I-node which represent isolated fracture tips, Y-nodes which represent abutment of two fractures or splaying of a fracture, and X-nodes which denotes fracture intersections (Manzocchi, 2002). Peacock et al. (2016) refer to X- and Y-nodes as *connection nodes*. Branches are classified by the bounding node at each end (Ortega and Marrett, 2002; Sanderson and Nixon, 2015). I-I branches are isolated branches with a I-node at each end. I-C nodes are partly connected branches and have one I-node at one end and a X- or Y-node at the other. The fully connected branches are called C-C branches and have a connecting node at each end. In addition, *unknown* branches are fractures that extend further than the sample area and end-nodes (E-nodes) are nodes in an unidentifiable zone or at the limit of the sample area.

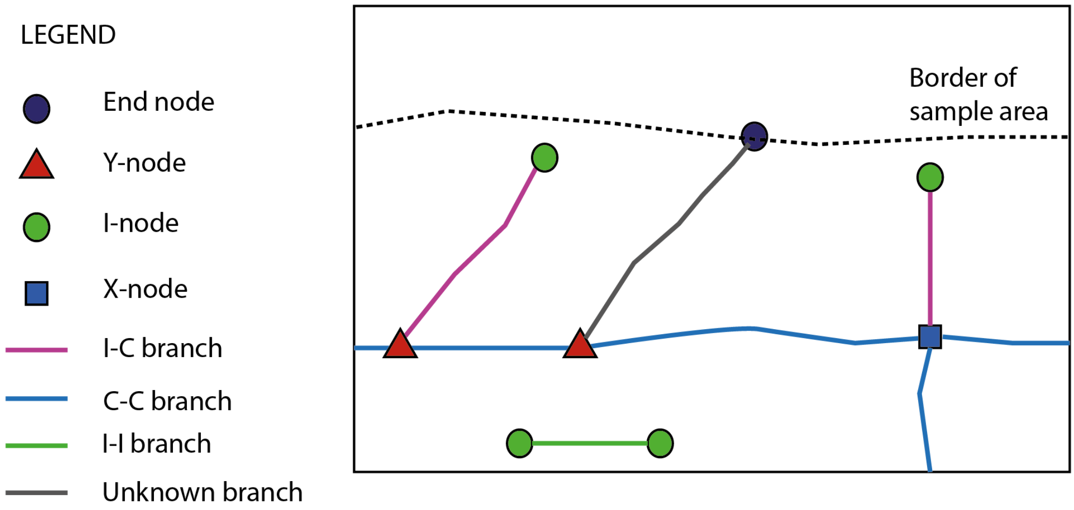

Figure 3.6: Schematic sketch illustrating different nodes and branches. Nomenclature from Sanderson and Nixon (2015)

Using topology, connectivity can be quantified using by the proportion of the different nodes and branches in an area. Connectivity are given by the average connections per branch and can be derived from the equation:

$$C_B = (3N_Y+4N_X)/N_B$$

Where C_B = average connections per branch, N_Y = number of Y-nodes, N_X = number of X-nodes, and N_B = number of branches (Sanderson and Nixon, 2015)

Since one branch, maximum can have a number of two connecting nodes, the C_B ranges from 0-2. A fully connected network will therefore have a C_B of 2, while an isolated network consisting of only I-I branches will have a C_B of 0. There are a number of different ways to portray the results acquired by topological analyses e.g. triangular plots that display the level of connectivity and different density maps over branch and node intensity, 2D intensity and connecting node intensity (Sanderson and Nixon, 2015; Nyberg et al. 2018) The use of topology in this project will be further explained in the methodology chapter (Chapter 4).

4. METHODOLOGY

4.1 Field data and data processing

The findings of this thesis are based on data collected during two field seasons in Shihtiping, Taiwan, in November 2016 and March 2017. Structural data from deformation bands and faults were acquired from different localities, which were selected by their difference in nature, good exposures and accessibility. Stratigraphical logging were carried out in study area A in order to characterise variability of the volcaniclastic host rock, and to make a standardisation of the lithological units. Unmanned Aerial Vehicle (UAV) mapping was carried during the second field season in order to improve the understanding of the study area, and to acquire imagery for fault damage zone topological mapping.

Sedimentological outcrop logging

A stratigraphical and sedimentological log of the tilted and alternating succession was made for this thesis in order to categorize the units and to improve the understanding of the host rock. The log was made based on field observations, in addition to earlier work conducted by Song and Lo (2002) and a volcaniclastic classification scheme from White and Houghton (2006). The units are categorised mainly by their grain size, but also different clast material (e.g. pumice and mafic bombs) are accounted for. The stratigraphical log is made for orientation in the field and to standardise the lithological units for further examinations of the deformation mechanisms. The log (Fig 5.3) is considered representative for the entire study area, due to clear similarities and consistencies between the lithological units that have been recognized in the different study areas. Representative rock samples of each unit were also collected.

Deformation band and fault localities

The structures of interest are located in two different areas, namely study area A and B (Fig. 5.1). A total of 12 localities have been examined systematically; five incipient bands, four mature bands and three faults, which, as discussed later in this thesis, are considered to represent different stages of fault evolution. Eleven of these localities are situated in study area A. One locality (Fault 3) is situated in the study area B and further subdivided into 11 localities. The same measurements were conducted on each locality, which are comprised of:

- Description of the locality.

- General information: strike and dip measurement of the deformation band/fault and coordinates.
- Series of close-up photographs along the band/fault with and without a measuring tape.
- Measurements along the band at each displacement marker:
    - Displacement whenever possible.
    - Thickness.
    - Number of strands.
    - Grain size of the matrix, clast size and nature of clast material.
    - Other notable features.
    - If present: width of the damage zone and spacing between structural features.

Strike and dip measurements were conducted with the application GeoID on an iPhone 6. Calibration and test measurements at of strike and dip at each locality were performed with a Silva Expedition compass including a leveller. Rock samples of deformation bands were also collected in order to conduct microstructural analysis and digital porosity estimations. Six samples from different localities along Fault 3 were also collected. Locally, some insecurities are connected to the measured offset. This is where the offset of a relative thick deformation band or a fault core is based on a stratigraphic boundary. Boundaries between lithological layers may fluctuate and is not always straight, consequently this may cause some uncertainties in the offset measurements.

The close-up photographs are taken with a *Nikon D3100* along deformation bands and faults at each locality and were later stitched together in the software *Panorama Stitcher Pro*. The single photos and photomosaics were later used to make schematic structural maps over the internal structures in the deformation bands and faults. The maps were made by drawing lines on the observable structures directly on the pictures in *Illustrator CC*. However, the internal structures may be under-representative in areas with densely spaced deformation bands and clusters as the they have effectively merged together. Illustrator CC were also used to make other figures and Microsoft Excel where used to make tables and graphs of the collected field data.

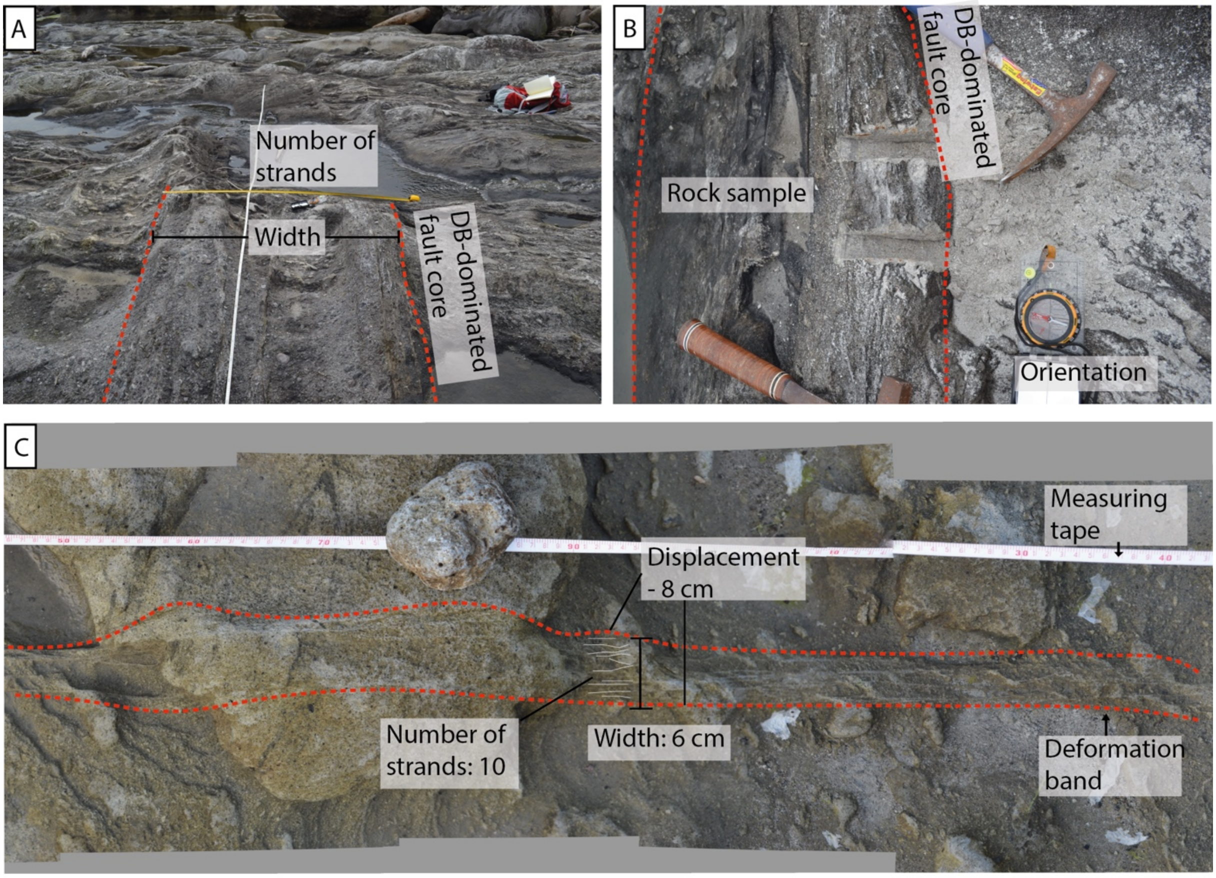

Figure 4.1: Various field photos from fault and deformation band localities. A) Outcrop photo from fault 3, locality 6. Thickness measurements of the fault core were collected with a measuring tape. Number of deformation strands is also counted. B) Photo illustrating how rock samples are acquired with a chisel and a geological hammer. The samples are then marked and wrapped in plastic. C) A photomosaic of field photos of a mature deformation band. A measuring tape is placed parallel with the deformation band and the thickness, number of strands and displacement is collected at each displacement marker.

UAV

UAV mapping was performed by drone (model Phantom Dji 3) during the second field season. Hence, better resolution was acquired in order to conduct large scale topological interpretation of the studied areas. The photos were georeferenced and stitched together into two 3D-models with *Agisoft Photoscan 1.3.2*. The two models are comprised of one overview model of the entire area including the two study areas and one higher resolution model over study area B including Fault 3. A simplified workflow of how the models of the virtual outcrops were made is shown in Figure 4.2, for more details see "Agisoft PhotoScan User Manual: Professional Edition, Version 1.3" (2017). In addition, UAV mapping contributed to an improved understanding of the studied area due to mapping of unreachable islands. This confirmed opposite dipping strata as two N-S tending gentle folds were discovered.

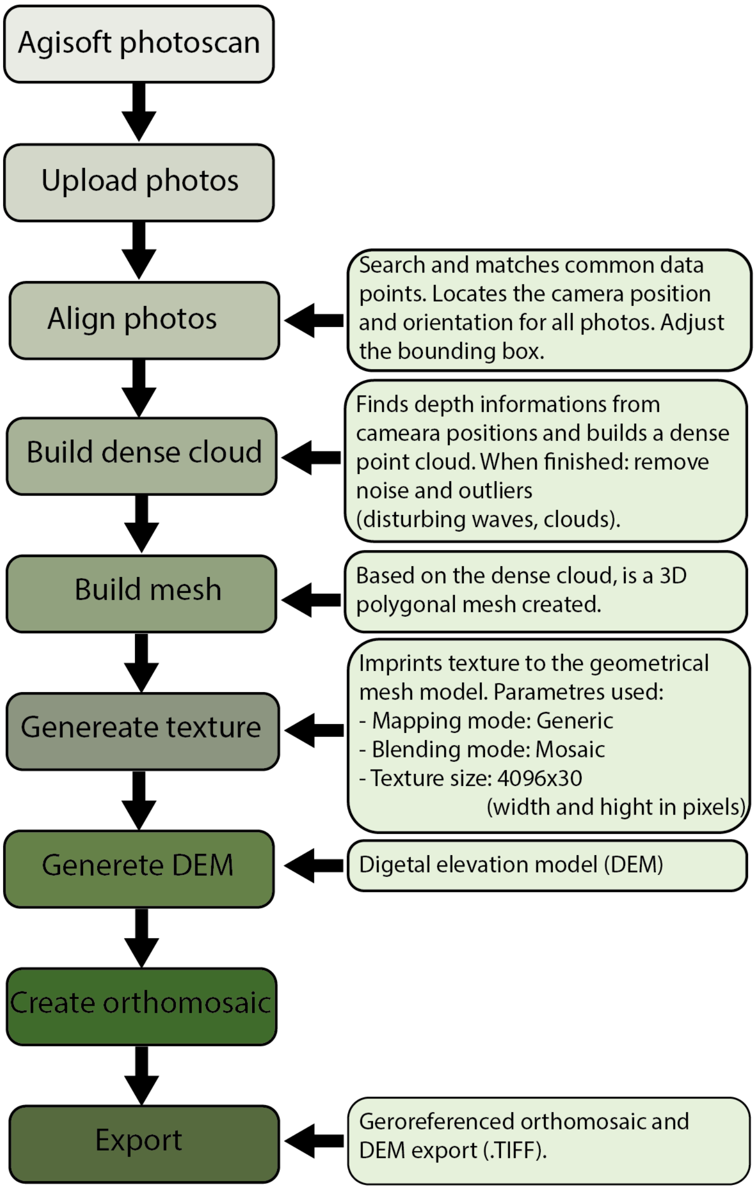

Figure 4.2: Simple workflow of how to generate virtual outcrops in *AgiSoft*.

4.2 Topological characterisation

The UAV models made in *Agisoft* were imported into the software *ArcGIS 10.5* in order to perform topological analysis of the structural network in the two study areas. All observable structural lineaments were digitized by making different feature classes in the software. A feature class is either a point, polyline or a polygon with the same features, and is made to group points and lines with the same characteristics into one specific unit. To illustrate, Y-nodes will be created as one feature class consisting of specific points, whereas I-C branches will be created as a particular polyline. An example of an un-mapped and a mapped network consisting of nodes and branches is given in Figure 4.3 A and B, respectively. Topological mapping was conducted on the UAV model of study area A and B. When the structural systems were mapped as branches and nodes, both topological and geometrical analysis can be carried out. The analysis is done in the open source toolbox *Network GT* which is described by Nyberg et al. (2018). By following the detailed workflow provided by the toolbox, spatial visualisation of the network properties can be done through different maps and plots. The toolbox performs both geometrical analysis of the fracture network as orientations, dividing fractures into sets and fracture size distribution, as well as topological analysis. Figure 4.3C display the interpretation boundary used in study area B, the sample area and grid cells. The network can be sampled through "Network Grid sampling" tool and is sampled within the interpretation boundary (Fig.4.3C). Each grid cell is set to be 2x2 metres and the search radius is set to 4 metres form the middle of each cell. By doing this, the program extracts branches and nodes for each grid cell by using a circle shaped search radius of 4 metres (Nyberg et al., 2018). The extracted branches and nodes can further be used to calculate different topological parameters as density maps over connecting nodes per square metres and branch intensity.

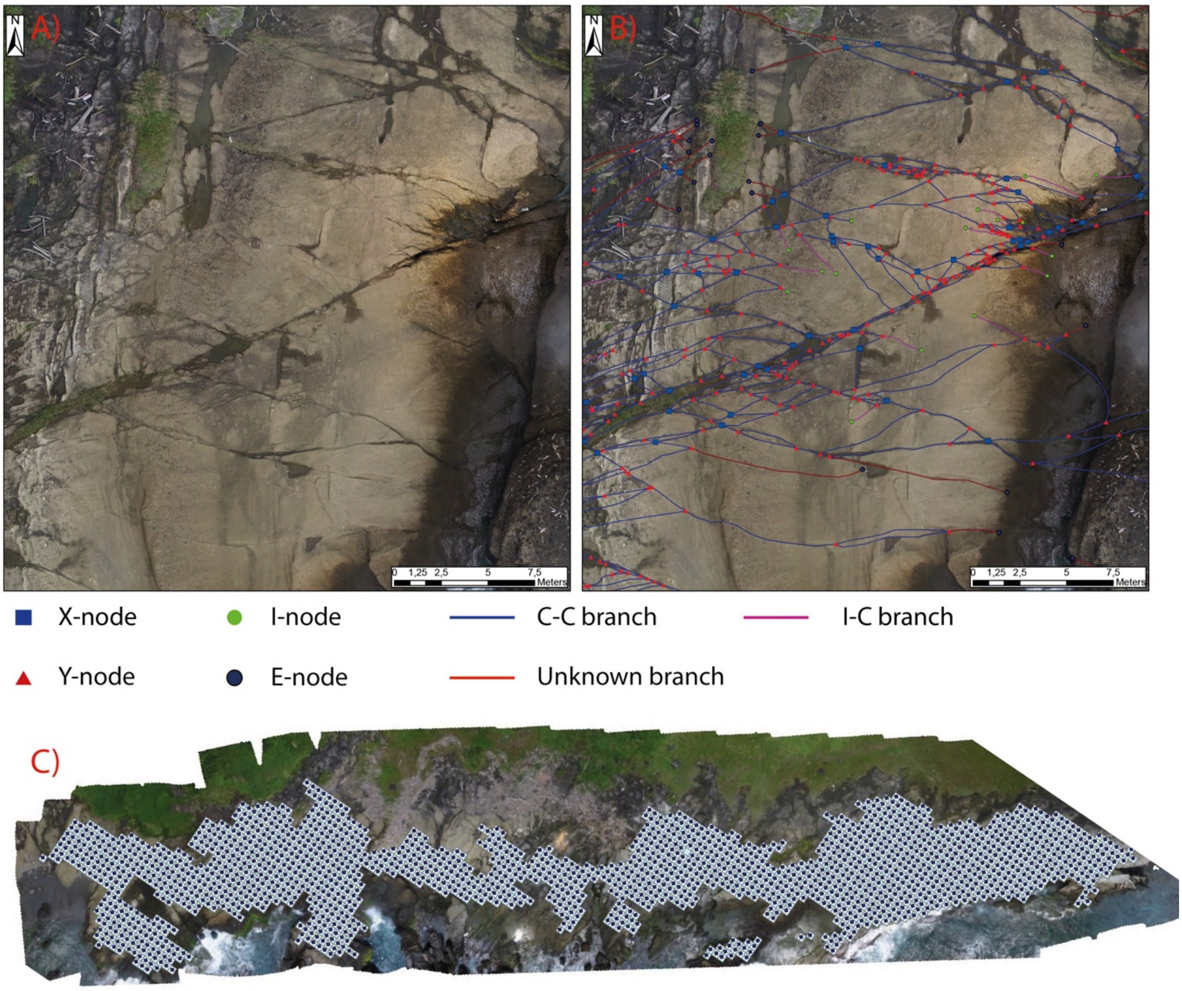

Figure 4.3: A) An un-mapped UAV photograph. B) Displaying the mapped UAV photo from Figure A. C) Displaying the sample area within the interpretation boundary. The sample area is divided into grid cell (2x2 m^2)

Uncertainties

The resolution of the UAV models allows structural mapping at metre-scale therefore including the main structural lineaments. Moreover, topology does not distinguish brittle fractures and deformation bands. Furthermore, this project only offers a 2D analysis of the network in a tilted succession. The fracture network architecture and its related connectivity varies in the subsurface. Measuring distances and length of structures are possible due to georeferencing of the pictures. However, errors of these measurement may occur caused by the accuracy of the georeferencing.

4.3 Microscopic analysis

Rock samples acquired in the field were sent to *Independent Petrographic Services Ltd* in Aberdeen, UK, for preparation of thin sections. The samples were polished down to 30 microns and saturated with blue epoxy, which was absorbed into pore spaces for better visualization of the porosity. All the thin sections were digitalized by using an *Epson Perfection v700 Photo* high-resolution scanner. This was done to ease navigation when using the Scanning Electron Microscope (SEM).

Optical microscope

Thin sections were further investigated by the use of optical microscopes. Two microscopes were used: A *Nikon Eclipse E400 POL*- and *Nikon Eclipse LV100 POL* polarizing microscope. Pictures were acquired by the means of the Nikon Eclipse LV100 POL and the software NIS Elements F and used for microstructural analysis of the deformation bands and fault samples.

Scanning Electron Microscope

Scanning Electron Microscope (SEM) was used in order to achieve higher resolution, increase magnification and improve the accuracy of the porosity measurements. The SEM analysis were conducted at the University of Bordeaux using a *Quanta FEG 250* SEM and at the University of Bergen using a Zeiss Supra 55VP Field Emission SEM. A beam of high-energy electrons is used in a vacuum-tight environment to produce a picture of microstructures in the thin section. The thin sections were coated with carbon in order to make the surface electrically conductive and were analysed by detecting backscattered electrons (BSE). By recording the BSE, the SEM produces grey-scale images. Different atomic numbers in minerals produce different scales of grey colours and by differencing the grey colours from one another, different minerals are detected. Bright minerals reflect a high atomic number, whereas darker areas are caused by lower atomic numbers. Pore spaces will therefore appear black. Identification of minerals can be carried out by an electron dispersive spectroscopy (EDS) detector. The analysis was carried out with a working distance (WD) of 9 millimetres, an accelerating voltage (EHT) of 15 kV and an aperture with a diameter of 60 µm.

Porosity analysis on BSE-SEM images

Two-dimensional (2D) porosity estimations are conducted based on BSE-SEM images through the software *ImageJ* (Ferreira and Rasband, 2012*)*, which allow estimation of both micro and macro porosity. The grey-scale pictures are saved as 8-bit images and a threshold is set in order to separate the black pore space from the grey mineral grains. This threshold is marked in red and adjusted manually by comparing the original image by the binary image so that the red threshold covers the black pore space. When the threshold is set, a binary (black and white) image is created which enables the program to calculate the black pore space areas by pixel counting. The percentage of black pixels in the image can so be transferred to 2D porosity. As the threshold is set manually, an average of four porosity measurements is used of each area of interest (e.g. host rock and deformation band) to avoid errors.

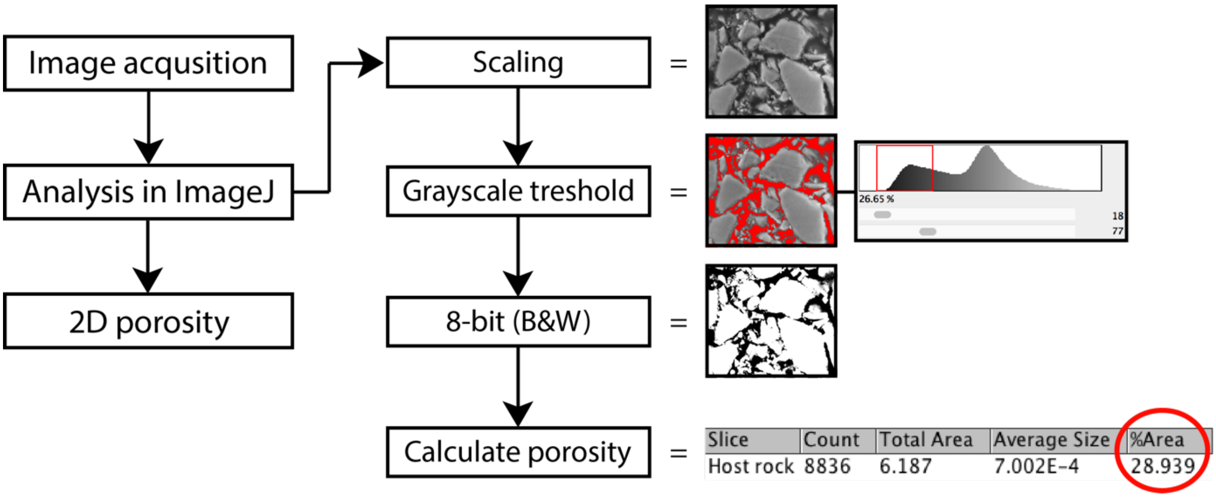

Slice	Count	Total Area	Average Size	%Area
Host rock	8836	6.187	7.002E-4	28.939

Figure 4.4: Figure from Kjenes (2018) of a schematic flow chart of the different steps in the calculation of porosity on BSE-SEM pictures.

Porosity measurements across deformation bands and faults are plotted in diagrams. The diagrams show porosity transections where porosity measurements are done across the thin section, over the host rock and the DB/fault rock, in order to obtain the lateral variability in porosity across the fault rock/DB. Where possible, two areas were measured in the deformed host rock on each side of the DB/fault rock, whereas two to three areas were measured for porosity in the fault rock and DB.

However, the extent of optical porosity estimations is limited as there are several sources of errors. Firstly, the digital porosity that is measured offers only a 2D assessment of the pore space and does not show the real three-dimensional porosity of rock sample. Consequently, particles and pore space that are smaller than 30 microns (the thickness of the thin section) may be excluded from the porosity measurements. This limitation is demonstrated by Figure 4.5.

Moreover, the porous heterogeneity in the rock is not accounted for in 2D porosity estimations. There are large internal variations within one thin section, thus the variations in one rock sample is probably even larger, not to mention the variations within a stratigraphic unit, nor a deformation band. To address this limitation four micrographs of different places in the thin section are used to measure porosity in the host rock samples. Also, several micrographs are used to preform porosity measurements of the deformation bands.

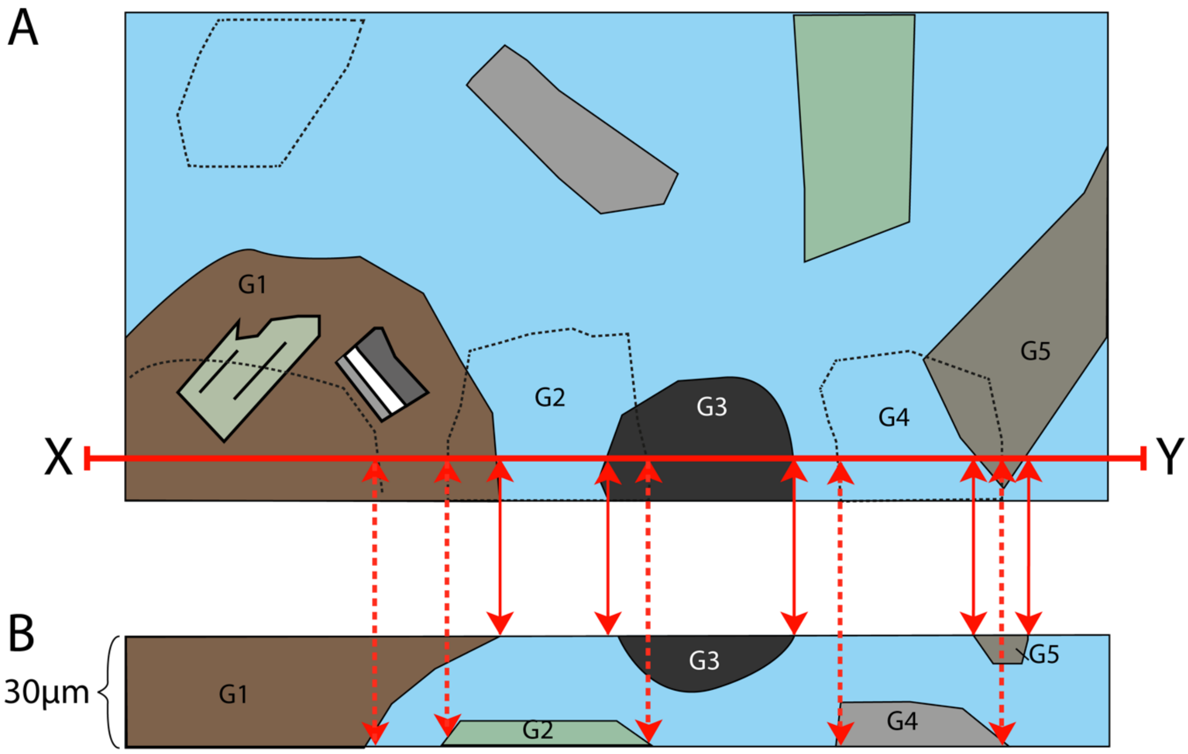

Fig 4.5: Graphic sketch of a thin section in top- and cross-sectional view. G=Grains. Blue colour= Epoxy/Porosity. Dashed lines=Grain boundaries at a deeper level in the thin section. A) Top view of a schematic and fictive thin section displaying grains G1, G3 and G5. B) Cross sectional view of the thin section, from X-Y in A. The profile view shows also grains at a deeper level of the thin section and the pore space between them, which were not visible in the top view in A. Modified from Thorsheim (2015)

5. RESULTS

This chapter includes structural, sedimentological, petrographical, microstructural and petrophysical qualitative and quantitative data, based on field work and related lab work. First, key structural elements, local stratigraphy and host rock properties in the study area are presented (Section 5.1). Next, an overview of the studied structural features is given (Section 5.2). Finally, detailed descriptions of the strike-slip deformation bands and faults forming the focus of this study are presented (Sections 5.3-5.6). The deformation bands (DB) and faults will be sorted into three stages of development based on maximum displacement: (i) Low-displacement incipient bands (D_{max}<5cm), (ii) High-displacement mature bands/clusters (5cm < D_{max} < 50 cm), (iii) Fully developed faults (D_{max} > 0.5 m), in respectively Section 5.3 to 5.5. Scaling of deformation band and fault attributes will be presented in Section 5.6.

5.1 Study area and host rock characterisation

Study areas A and B are located in a folded succession of volcaniclastic rocks, which are situated on the eastern limb of an open N-S trending syncline (Fig. 5.1A and B). Figure 5.1 shows a map of the coastal outcrops of Shihtiping with the main structural elements and the two studied areas outlined.

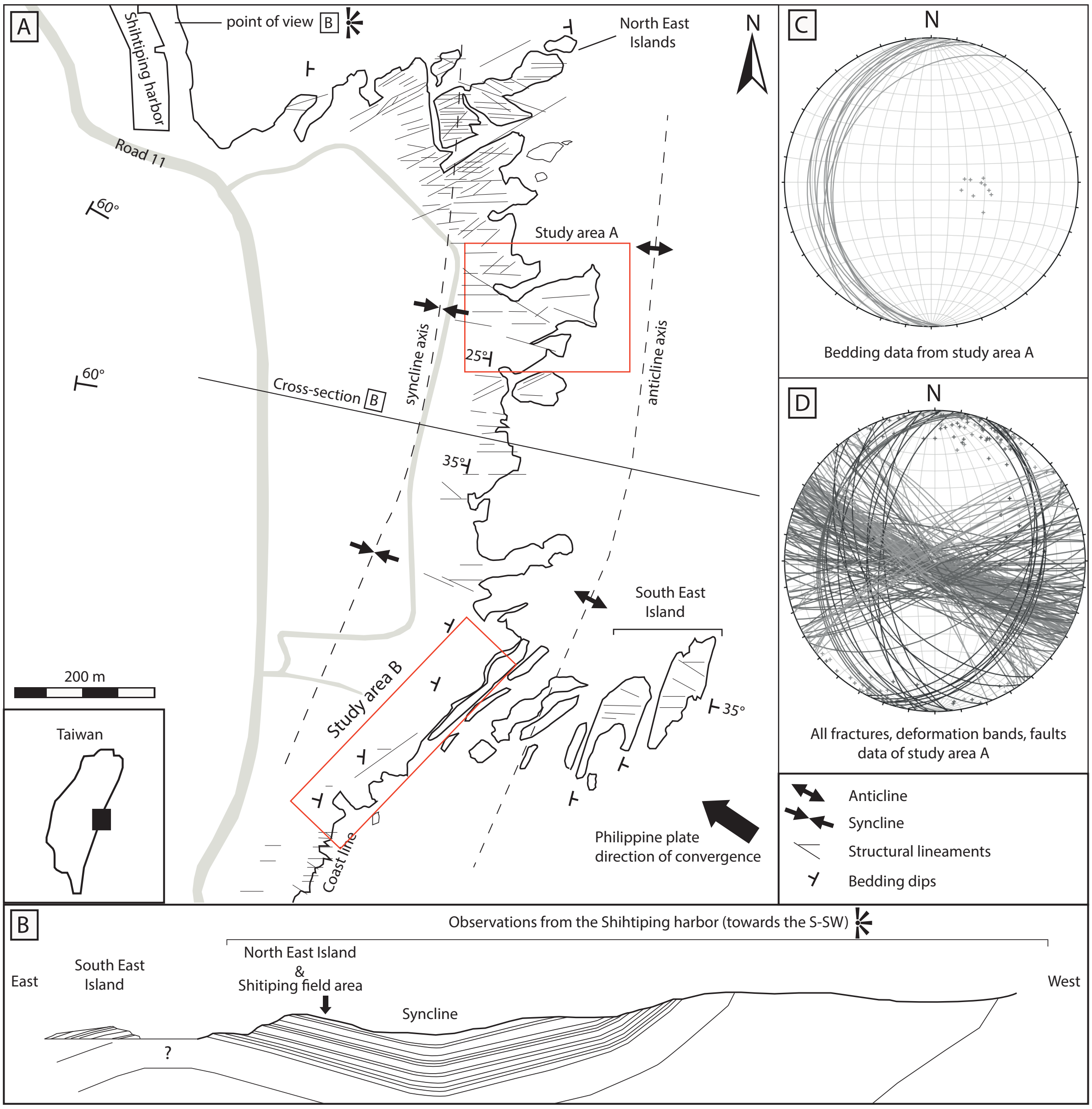

Figure 5.1: Overview figure modified from Cavailhes and Rotevatn (accepted). A) Map over Shihtiping showing the main structural lineaments and with the two study areas A and B outlined in red. Inset map showing location in Taiwan B) A schematic cross section through the study area that shows a syncline and an anticline. Location shown in A. C) Lower-hemisphere stereonet showing the orientation of the bedding in study area A. D) Lower-hemisphere stereonet of fractures, deformation bands and faults from study area A.

The stratigraphy in the study area A is comprised of a tilted succession (26°) of tuffs, ignimbrites and pyroclastic material (Fig.5.2). The ignimbrites consist of white pumice clasts in a fine matrix of ash. The pyroclastic material consists of dark, low-porosity volcanic bombs/lapilli and scoria in a matrix of ash. To describe the host rocks in the study area I follow the previous classification from the study area by Song and Lo (2002) in addition to a volcaniclastic classification scheme by White and Houghton (2006). The following lithologies have been recognised in the study area:

i. Fine to medium tuff
ii. Coarse to very coarse tuff
iii. Fine lapilli-tuff
iv. Medium lapilli-tuff
v. Coarse lapilli-tuff
vi. Polygenic volcanic breccia
vii. Ignimbritic conglomerate

Figure 5.2 displays a cross-section from a key outcrop (locally called Cuesta) in study area A, which shows the stratigraphy of study area (Fig. 5.1). A stratigraphic log of the same succession is shown in Figure 5.3.

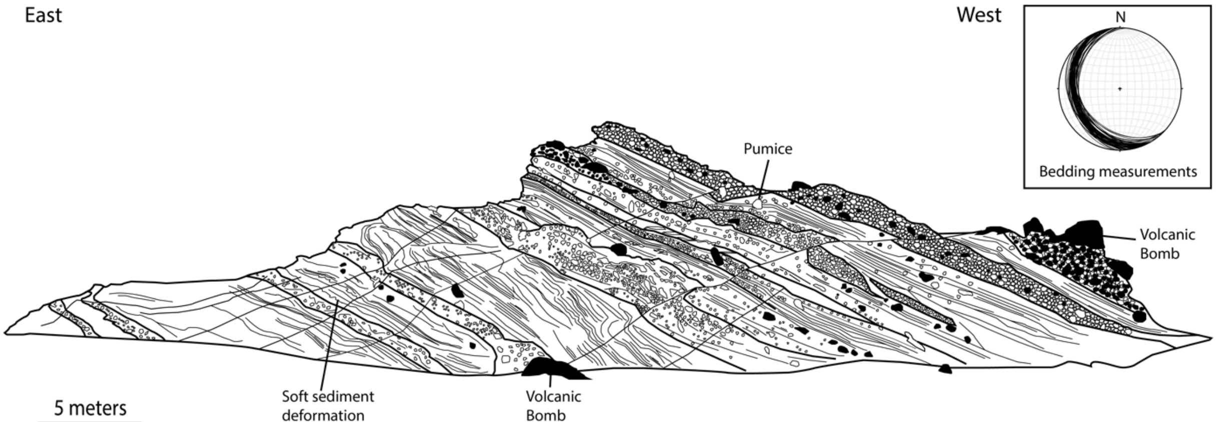

Figure 5.2: Schematic cross-section of the stratigraphy exposed in the studied outcrops. The orientation of the tilted beds is shown by the lower-hemisphere stereonet and is approximately 158/26 (strike/dip). Modified from Kjenes (2018) and Cavailhes and Rotevatn (accepted).

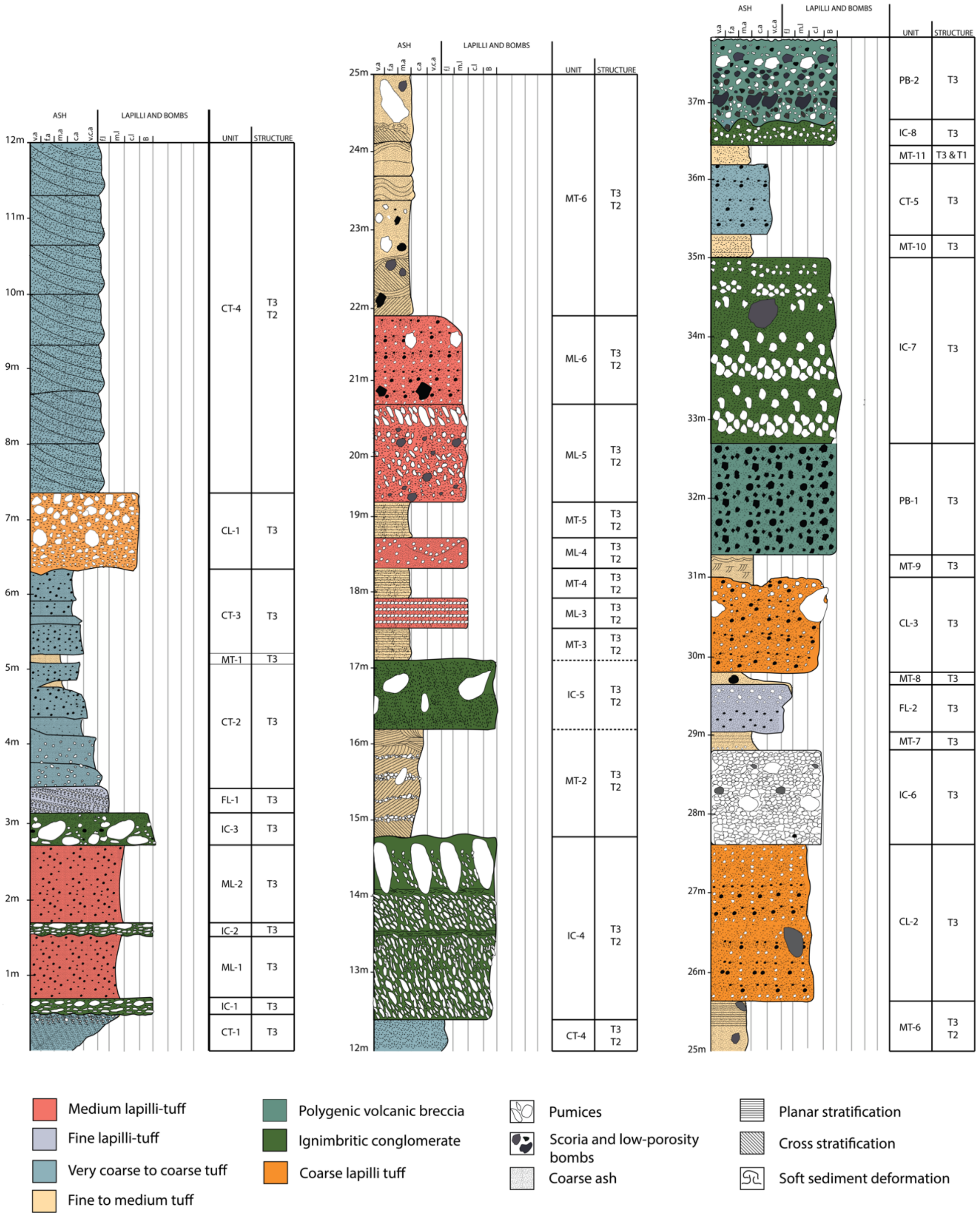

Figure 5.3: Stratigraphic log of the upper part of the Shihtiping White Tuff Member based on field observations. The stratigraphy of the log displays the same stratigraphy shown in Figure 5.2. The unit column shows the name of the units. MT=Medium to fine tuff, CT=Coarse to very coarse tuff, FL=Fine lapilli-tuff, ML=Medium lapilli-tuff, CL=Coarse lapilli tuff, IC=Ignimbritic conglomerate, PB=Polygenic volcanic breccia. The structure column shows the type of deformation band type that is observed in each unit; T1=Type 1 (Pure compaction bands); T2= Type 2 (Reverse compactional shear bands); T3=Type 3 (Strike-slip compactional shear bands).

Fine to medium tuff units are fine to medium grained and characterised by a variety of sedimentary structures such as cross stratification, planar stratification and locally soft sedimentation deformation features (Fig. 5.4A and B). Occasional volcanic bombs and pumice clasts can be found in these layers. The layer thickness of the fine to medium tuffs are generally 10-30 centimetres. However, thicker units with a thickness up to 3.5 metres are also observed, and generally interbedded with local ignimbritic layers. The lateral extent of the fine to medium tuff varies greatly, and commonly pinches out laterally.

Coarse to very coarse tuff units are abundant and generally constitute thicker layers (2-5 m) of cross-stratified tuff (e.g. unit CT-4 in Fig.5.3; Fig. 5.4C). Although thinner (< 1 m) and poorly stratified coarse tuff layers do occur. Occasional scattered fine lapilli of pumice and dark scoria occur in the coarse tuff units.

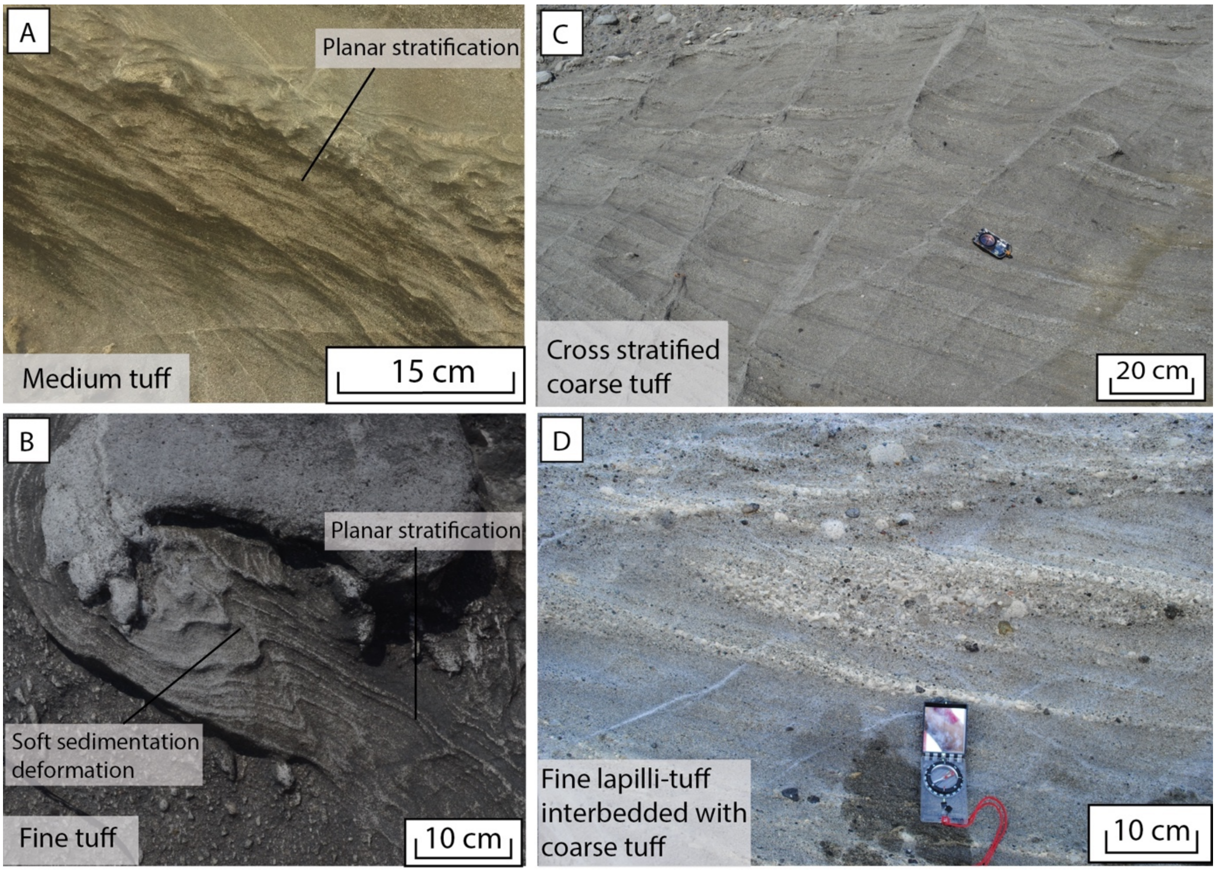

Figure 5.4: Field photographs that illustrate the difference within the tuff layers. A) Picture of a medium tuff unit (unit MT-3) with planar stratification. B) Fine tuff from unit MT-2 with planar stratification and soft sedimentation deformation in association with a pumice bomb. C) Field photo of cross stratified coarse to very coarse tuff (unit CT-4). D) Interbedded coarse tuff and fine lapilli-tuff (unit CT-1).

In the *fine lapilli-tuff,* fine lapilli are the dominating grain size and can either consist of white pumice or mafic scoria (called *polygenic* fine lapilli tuff). The fine lapilli tuffs are locally interbedded with coarse tuffs, as shown in Figure 5.4D.

Medium lapilli-tuff and coarse lapilli-tuff varies between clast supported to matrix supported. The clast composition is also variable, from ignimbritic to polygenic with a combination of pumice, scoria and low-porosity lapilli clasts (Fig. 5.5A)

Ignimbritic conglomerates are recognised in the field by their white/grey colour and big pumice clasts. These units consist of matrix-supported bombs of pumice (> 64 mm), except unit IC-6 which consist of clast-supported pumice. The bombs of pumice range in diameter from 6 to 50 centimetres and are often imbricated. Red and black scoria bombs are also found within the white pumice. The matrix is composed of coarse ash and, locally, fine lapilli. Thin layers of fine to coarse tuff with a limited lateral extent may occur locally. Figure 5.5C shows an ignimbritic conglomerate unit with an interbedded local medium tuff layer.

Two units of *polygenic volcanic breccia* have been recognised in the upper part of the studied succession (Unit PB 1-2 in Fig. 5.3). These units are shown in Figure 5.5D and are associated with a high content of sub-angular, dark and low-porosity bombs (> 64 millimetres) and lapilli (32-64 mm) in addition to rounded pumice clasts. The units are predominantly supported by a matrix of coarse tuff to fine lapilli-tuff.

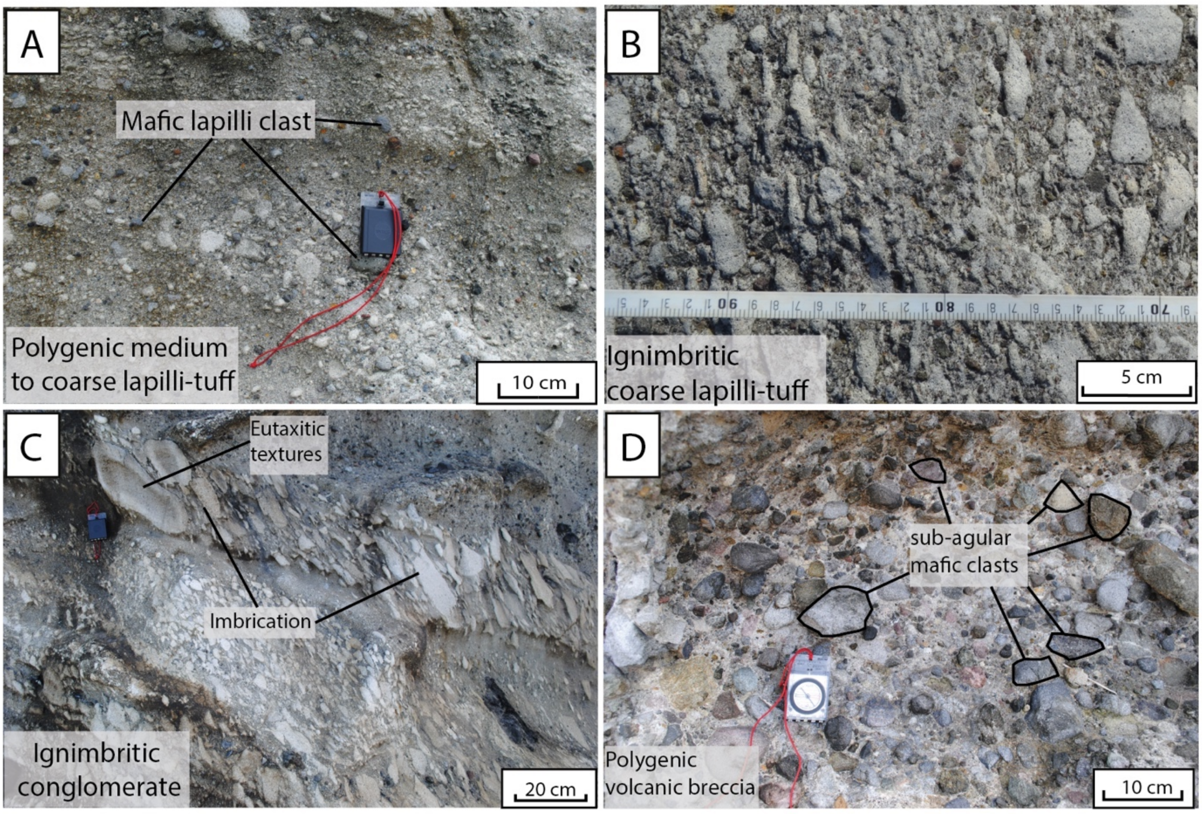

Figure 5.5: Photographs that display the coarser grained units. A) Unit ML-6 with polygenic medium to coarse lapilli. B) Photographs of a representative ignimbritic coarse lapilli-tuff layer (CL-1) with slightly imbricated pumice clasts. C) Ignimbritic conglomerate with variations in clast size (unit IC-4). D) Field photo of unit PB-1 showing the polygenic volcanic breccia units.

Host rock mineralogy, microtexture and porosity

Although the above field-based characterisation of the studied lithologies shows breakdown into seven macro-texturally different units, thin section observations (optical microscope and SEM) suggest that all of the lithological sub-units are mineralogically and micro-texturally quite similar. All the units exhibit a porphyritic texture and consist of (in decreasing order) plagioclase, hornblende, hypersthene (orthopyroxene), augite (clinopyroxene) and iron oxides in a matrix of volcanic glass (Fig 5.6). The grain size of the minerals vary from 0.3 to 3 millimetres. Phenocrysts exhibit a euhedral to subhedral crystal shape, whereas the glassy matrix consists of glass fragments which vary from 0.005 to 0.02 millimetres. Lithic fragments showing a similar mineral assemblage are observed in most of the coarser grained lithologies. Although the previously defined lithological sub-units are texturally fairly similar under the microscope, some textural variability is observed within the sub-units. Pore space, grain size, quantity and size of lithic fragments are the most prominent differences. For illustration, the lithic fragments are generally larger in the polygenic breccia (1 cm) than in other subunits, and the fragments in medium to fine tuff layers is finer-grained (0.1-0.5 mm) and more porous. The differences become evident in the porosity plot where a mean porosity (Fig. 5.7) of 9.57% is found in the polygenic volcanic breccia, and the fine tuff and fine to medium lapilli-tuff have the highest mean porosity readings of 28% and 36%, respectively. However, spatial porosity variations up to 20 % within the same unit is common. For example, the porosity measured in the polygenic volcanic breccia fluctuates between 2.9% and 15% and in the fine to medium tuff, it fluctuates between 20% and 40% (Fig. 5.7).

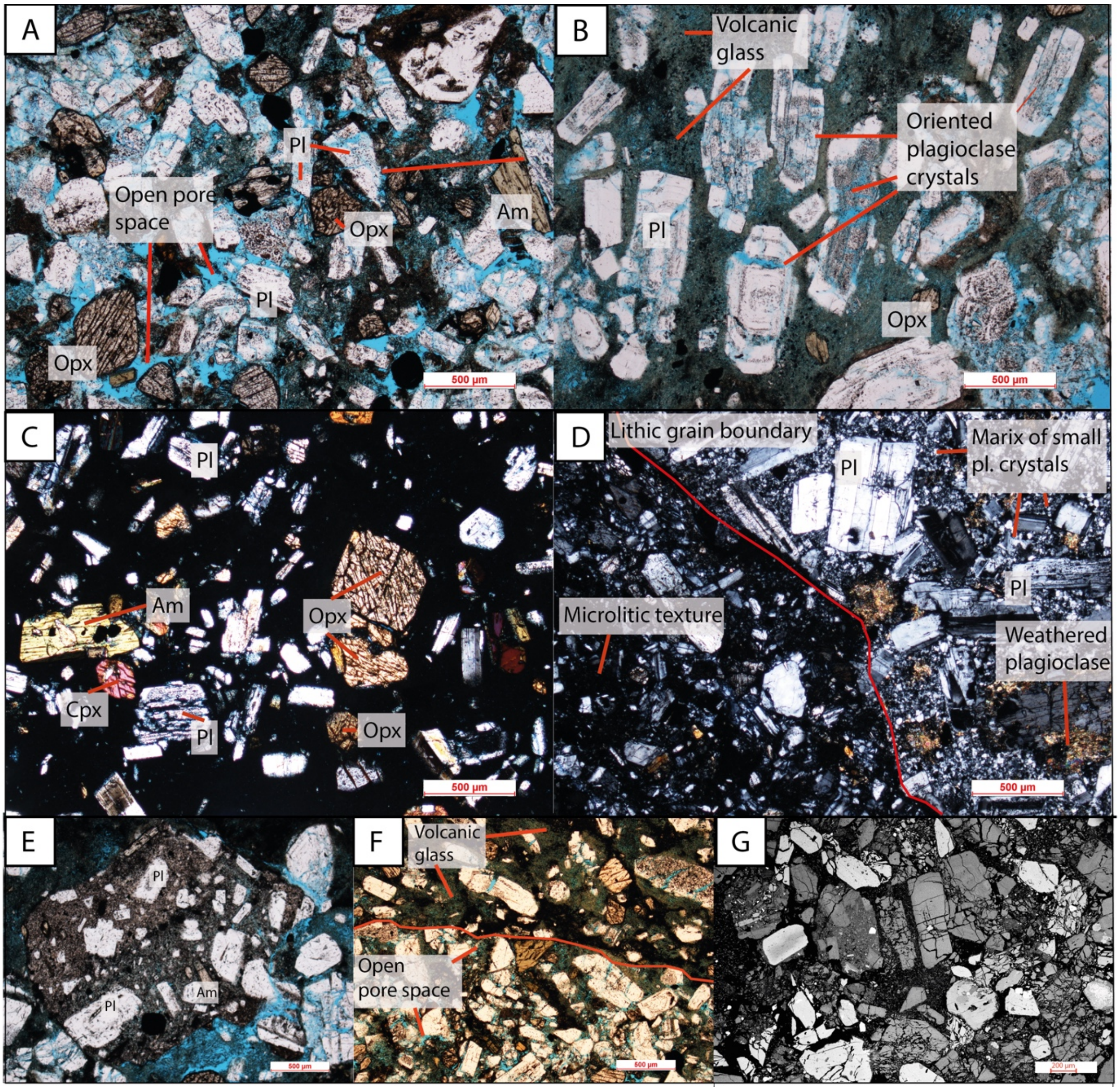

Figure 5.6: Photomicrographs of the host rocks. A) A coarse tuff unit with plagioclase (Pl) hypersthene (Opx) and hornblende (Am) in plane-polarised light (PPL). Blue epoxy represents open pore space. B) Oriented plagioclase crystals in a matrix of glass in PPL from a pumice clast in an ignimbritic conglomerate. C) A medium tuff unit with crystals of plagioclase (Pl) hypersthene (Opx), hornblende (Am) and augite (Cpx) in cross-polarised light (XPL). D) Polygenic volcanic breccia. The lithic fragment exhibits a porphyritic texture with plagioclase crystals in a matrix of fine grained plagioclase crystals. Note the absence of open pore space and glass within the lithic fragment. Also, the matrix around the lithic grain is relatively crystalline in these units. E) An imagery of a lithic fragment in PPL with plagioclase (Pl) and hornblende (Am) in fine grained matrix. Decreased porosity within the lithic fragment is established by the lack of blue epoxy. F) Shows the variation within a fine to medium tuff unit. The upper part has fewer and lager crystals in a glassy matrix, whereas the lower part is clast-supported by more and smaller crystals and have more open pore space. G) Micrograph from SEM (Scanning electronic microscope) displaying high fracture density in the host rock.

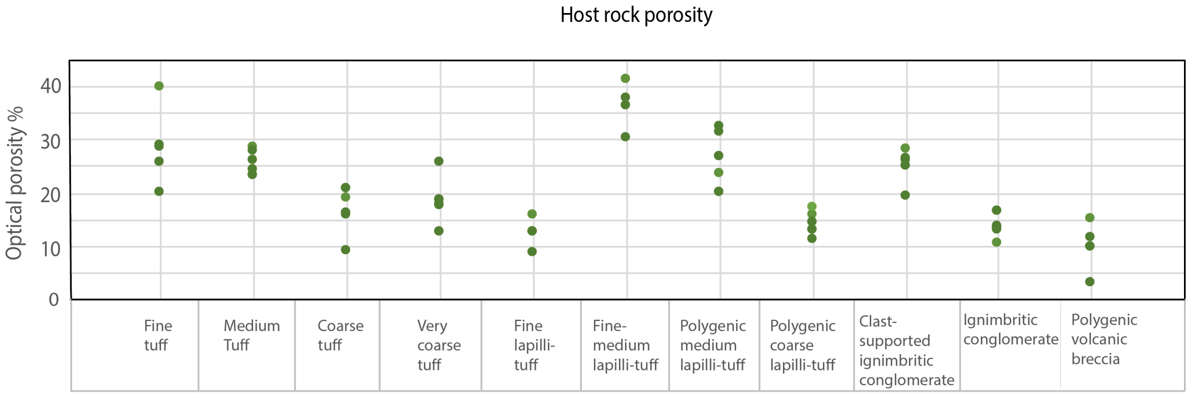

Figure 5.7: Porosity measurements of the sub-units carried out in Image J based on SEM imagery.

5.2 Overview of structures found in the study area

Six different types of faults, deformation bands (DBs) and fractures are found in study area A. Three different types of DBs are classified following Aydin et al. (2006) and Fossen et al. (2007). Therefore, their orientation in relation to bedding, shear movement, distribution in different lithological units, porosity contrast relative to the host rock and dominant deformation mechanism have been taken into account. The following summary is partly based on Cavailhes and Rotevatn (accepted) and Kjenes (2018) in which the different types of DBs and the evidence for their classification are well documented:

Deformation bands:

- *Pure Compaction Bands* (PCBs; Type 1; Fig. 5.8A and B) occur as singular, slightly elevated strands and are limited to unit MT-11, a medium to coarse grained tuff unit. The PCBs exhibit a high dip compared to the bedding. The length of the strands varies from 11 to 80 centimetres with an average length of 31 centimetres, and the thickness diverges from 3 to 15 millimetres, with an average thickness of 7.2 millimetres. Generally, the PCBs are evenly spaced with an average spacing of 2 cm. The bands exhibit no shear displacement but feature a reduced porosity of 34.19% relative to the host rock (Kjenes 2018). Evidence provided by both field- and microstructural studies suggests that the main deformation mechanisms of the PCBs are grain reorganization and granular flow (Fig. 5.8B) (Cavailhes and Rotevatn, accepted). See appendix IV for supplementary field measurements and plots.
- *Reverse-sense Compactional Shear Bands* (RCSBs; Type 2; Fig. 5.8 C and D) are cataclastic bands and comprised of a flat-ramp-flat geometry associated with reverse

offset. Three different segments can be distinguished; flat thrusts, ramp thrusts with additional antithetic back thrusts (Fig. 5.8C). The flat thrusts are sub-parallel (20°-30°) to the bedding and favour lithological boundaries, whereas the ramp thrusts dips 40°-50° and serve as connecting strands between the flat thrusts. The thickness fluctuates from 2 to 9 millimetres in the flat segments, 0.5 to 2 millimetres in the ramp segments, and the back thrust are less than 0.5 millimetres thick (Kjenes, 2018). Occurrence of the RCSBs are restricted to ignimbrite dominated units and tuff units (Fig. 5.3). Maximum displacement occurs in the flat segments and is measured to be 5 centimetres (Kjenes, 2018). Local striated slip surfaces are also most abundant in the flat segments, but minor slip surfaces are also present in the other segments (Fig. 5.8C). Grain size reduction within the RCSBs relative to the host rock is seen both in the field and in microscope and feature a porosity reduction of 55 % relative to the host rock (Kjenes, 2018) Moreover, evidences of grain crushing, as intense grain fracturing along abrupt deformation band boundaries and comminuted mineral grains within the deformation band, establish that cataclasis is the main deformation mechanism in RCSBs (see Fig. 5.8D) (Cavailhes and Rotevatn, accepted; Kjenes 2018).

- *Strike-Slip Compactional Shear Bands* (SCSBs; Type 3; Fig. 5.8E and F) are present in the entire succession as it dissects all of the lithologies in conjugate, mutually cross-cutting sets. The two sets of SCSBs exhibits dextral and sinistral shear displacement, respectively, and the dihedral angle between the sets are approximately 50°. The dextral strike-slip bands strike WSW-ENE, whereas the sinistral bands strike WNW-WSE. Both sets are steeply dipping (average of 78°). SCSBs appear as single strands, clusters or networks of strands (Fig.5.9). The appearance of the SCSBs is dependent on lithology, where the same band may be a one-centimetre thick cluster in a clast supported lapilli-tuff unit and a 10 centimetres wide network, consisting of several strands, in a fine to medium tuff unit. The displacement varies between 1 to 350 millimetres. Patchy striated slip surfaces are locally associated with the SCSBs. Porosity measurements show an average porosity reduction of 60% compared to the host rock (Kjenes, 2018) Observations in optical microscope and SEM show grain reorientation, compaction and grain comminution within the band, hertzian and abrupt grain contacts, and heavily fracturing of minerals along band boundaries. Therefore, cataclasis is found to be the dominant mechanism behind the development of SCSBs (Cavailhes and Rotevatn, accepted; Kjenes 2018).

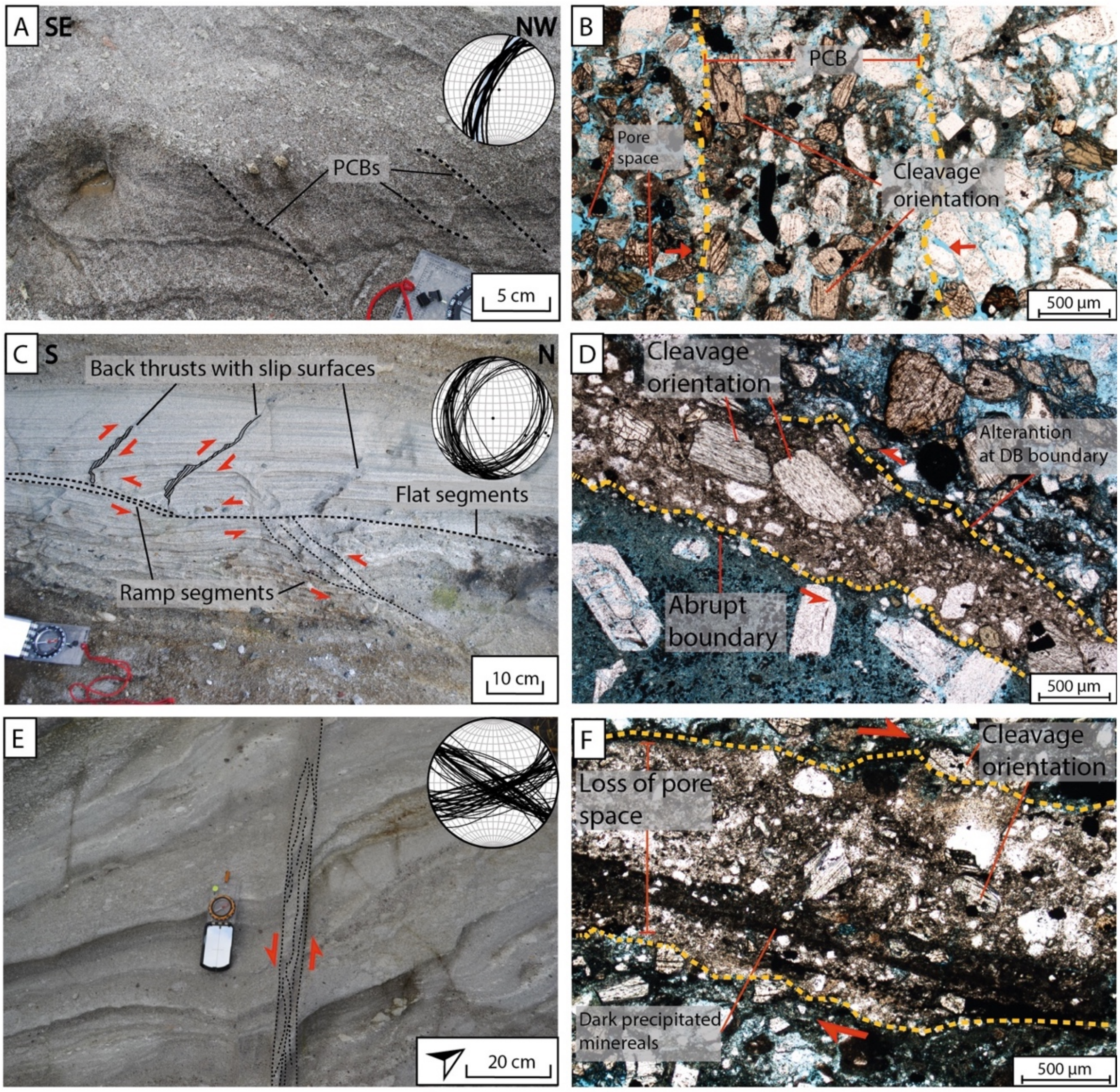

Figure 5.8: Outcrop photographs and photomicrographs of the three types of deformation bands. Kinematic indicators are marked with red arrows. A) Field photo of PCB in a medium to coarse tuff unit (cross-sectional view). The lower-hemisphere stereonet shows the PCBs orientation. B) Imagery of a PCB in plane polarised light (PPL) in optical microscope. Note the compacted zone (marked by a dashed yellow line) of less free pore space and the pyroxene crystals that are oriented parallel to the DB by their cleavage plane. Photo courtesy of Martin Kjenes. C) Outcrop photo in cross-sectional view where RCSBs crop out with flat, ramp and back thrust segments. The lower-hemisphere stereonet shows the orientations of RCSBs. Photo courtesy of Martin Kjenes. D) Photomicrographs in PPL (courtesy of Martin Kjenes) taken of a RCSB located at a boundary between medium to coarse tuff (upper part) and a pumice clast (lower part). E) Field photograph in map view of a representative sinistral SCSB. The lower-hemisphere stereonet displays the orientation to the two conjugate sets. F) Optical microscope picture of a SCSB (marked with a red dashed line) in PPL.

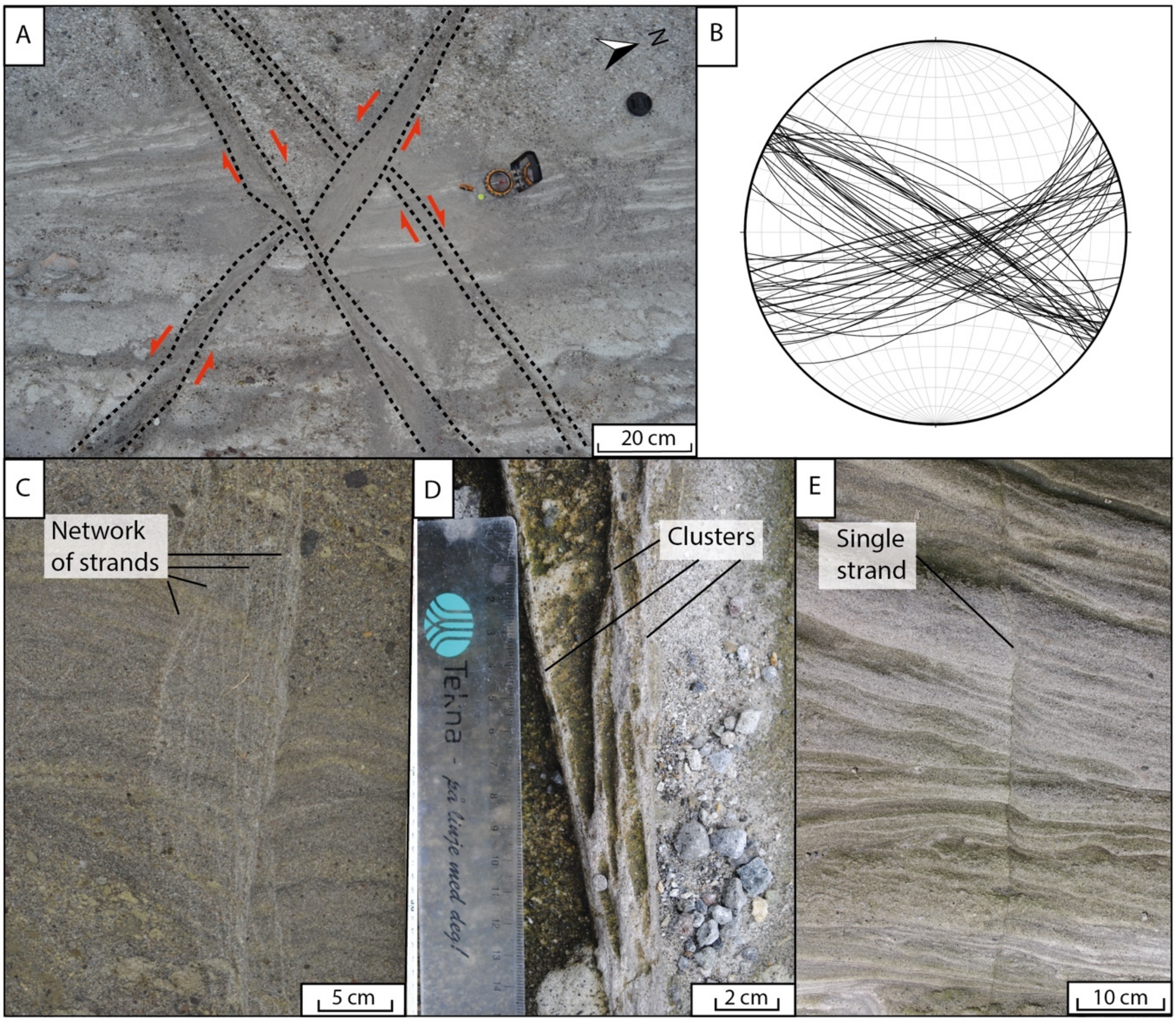

Figure 5.9 Field pictures the outcrop expression of SCSBs (Type 3 bands). A) Cross-cutting relations between sinistral and dextral conjugate SCSBs. B) Lower-hemisphere stereonet of the conjugate sets. C) DB network. D) DB clusters. E) Single-strand DB.

Faults and other types of fractures:

- *Strike-slip faults* exhibit the same orientations as the SCSBs but are distinguished based on larger displacements (>50 cm). In addition, one or several through-going slip surfaces are commonly developed. Horizontal striations at slip surfaces indicates the strike-slip kinematics together with offset markers (as bedding, bombs and older bands). The structural style of the faults appears to be affected by the local lithology, in which they are either dominated by DBs or by brittle shear fractures and slip planes. Generally, the faults are fully developed with a fault core and a damage zone, with localised exceptions. Segments of linking faults are observed in UAV photos and will be reviewed in section 5.5. As is argued later in this thesis, the strike-slip faults are inferred to have developed from deformation bands to fully developed faults; this forms the key topic for this thesis (see Chapter 1).

- *Extension fractures* occur in the damage zone of faults, and in brittle lithologies together with *shear fractures* where granular deformation is not possible (e.g. mafic bombs). The extension fractures are perpendicular to the minimum principal stress axis (σ3), whereas the shear fractures typically develop 20°-30° to the maximum principal stress axis (σ1). Also, *shear opening fractures* are common in low-porosity volcanic bombs.

Based on field observation (cross cutting relations, where the SCSBs cross-cut both the PCBs and RCSBs, orientation relative to the bedding and published material on the regional stress state) Cavailhes and Rotevatn (accepted) and Kjenes (2018) has suggested a possible evolutionary model of the deformation bands in the study area. According to the authors, the three types of DBs formed in sequence during horizontal shortening and progressive burial. The PCBs developed first by granular flow, initiated by horizontal compression. Followed by folding which lead to increased burial and confining pressure which promoted the development of the RCSBs. Lastly, the SCSBs formed after the folding as increased burial caused the vertical stress to exceed the horizontal intermediate stress. Accordingly, the orientation of σ3 and σ2 switched direction. The SCSBs are the most common type of DBs in the study area and dissects the entire succession. Considering the distribution, orientation and kinematics of the conjugate SCSBs it is clear that they correspond well with the orientation and kinematics of the strike-slip faults. Consequently, the SCSBs are related to the strike-slip faults. Hence, the SCSBs and the strike-slip faults will be the focus of interest in this thesis, in which the aim of the study is focused on the evolution from DBs to faults (Chapter 1). PCBs (Type 1) and RCSBs (Type 2) will not be treated further in this thesis and the remaining sections is dedicated to the SCSBs (Type 3), and the strike-slip faults. From here on, SCSBs (Type 3) will simply be referred to as deformation bands (DBs).

DBs and faults are widely distributed in study area A. Figure 5.11A show the distribution of observable dextral (0°-90°) and sinistral (90°-180°) structures (DBs and faults) with their orientation plotted in a rose diagram. The dextral structures exhibit a larger range in orientations from 045° to 075° than the sinistral structures, which exhibit a dominant trend of 110°-120°.

In the following sections, bands and faults are described in an attempt to elucidate the development from single bands to fully developed faults. Doing so, displacement is used as a proxy for the *stage of development* (Fig. 5.10). This allows the subdivision into three bins/stages, which will be described in Sections 5.3-5.6:

(i) Low-displacement incipient bands (D_{max}<5 cm)

(ii) High-displacement mature bands/clusters (5 cm < D_{max} <50 cm)

(iii) Fully developed faults with a through-going principal slip surface (D_{max} > 0.5 m).

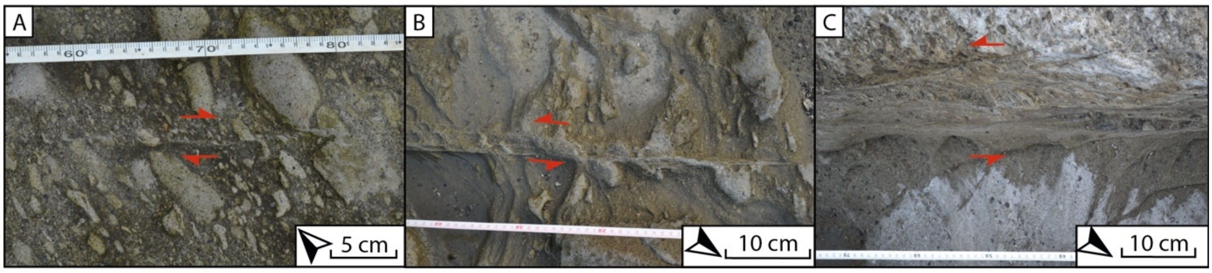

Figure 5.10: Stages of development; A) Low-displacement incipient bands (D_{max}< 5 cm) B) High-displacement mature bands/clusters (5 cm < D_{max} <50 cm). C) Fully developed faults with a through-going principal slip surface (D_{max} > 0.5 m)

Location of the DBs and faults that are studied in detail in study area A is outlined in Figure 5.11B. Where DB 1 to 4 are high-displacement mature bands/clusters and marked in pink, band 5 to 9 are incipient bands and outlined in green, whereas Fault 1 and 2 are marked by yellow lines.

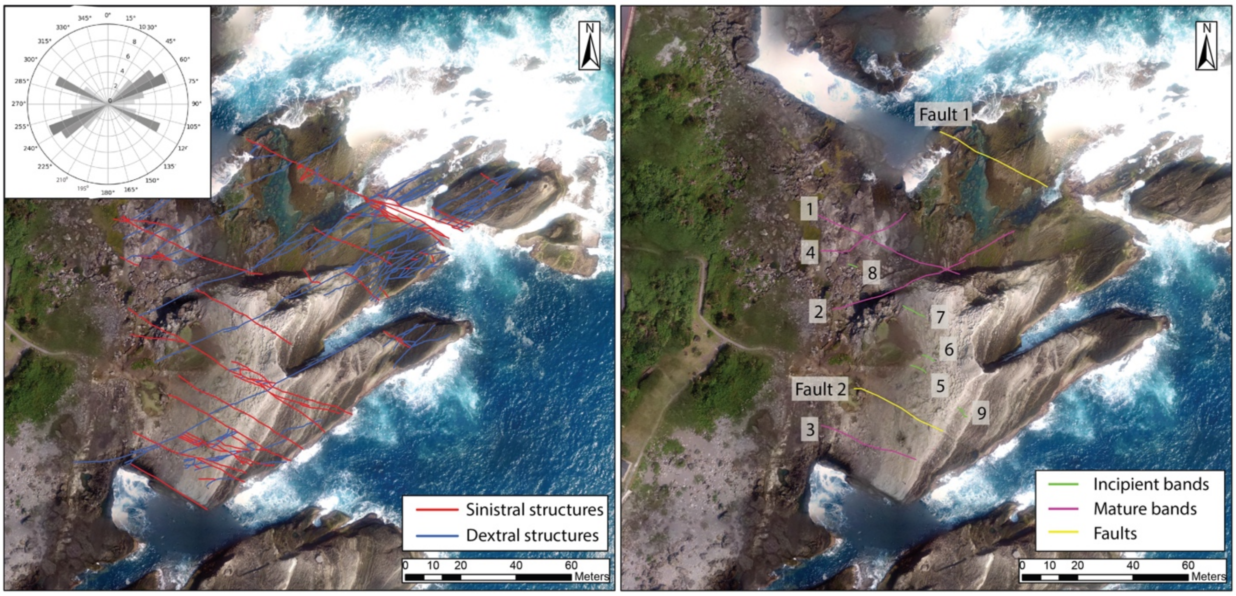

Figure 5.11: A) Unmanned Aerial Vehicle (UAV) photo of study area A. Observable structural lineaments (deformation bands and faults) are outlined (Scale 1:1580). Sinistral and dextral structures are marked in red and blue, respectively. The rose diagram reveals the two predominating trends of the dextral WNW-ESE striking structural lineaments and sinistral ENE-WSW trending structures. B) Locality map of study area A. Two faults are studied within the area and named Fault 1 and Fault 2. Four mature bands (see section 5.5) are studied in detail and given a number between 1 to 4. Lastly, the five incipient bands (see section 5.4) that have closely been examined are given a number between 5 to 9.

5.3 Low-displacement incipient bands (D_{max}< 5 cm)

The incipient bands are comprised of single strands and can be surveyed along their entire length, from tip to tip (Fig. 5.12). The length of the incipient bands varies between 3 to 6.5 metres and the bands rarely comprised of more than three strands. Moreover, the low-displacement bands are commonly segmented, with individual segments being bound together by soft- or hard- linked relay zones. It is distinguished between cumulative and regular width of the incipient bands. As each strand commonly is 1 to 2 millimetres thick, whereas spacing between the strands increases in relay zones which make the associated cumulative width higher. The cumulative width of the relay zones is dependent on lithology. In the polygenic volcanic breccia, the relay zones are less than 3 centimetres wide and 7 centimetres long, while in the medium tuff and in the ignimbritic conglomerate relay zones are up to 12 centimetres wide and 50 centimetres long. As aforementioned, five low-displacement incipient bands are covered (band 5 to 9 in Fig. 5.11B) in this thesis. However, only field data of band five and six are presented in detail herein (Fig. 5.13 -14), where thickness, displacement, number of strands and grain size are systematically collected along the length of each band. Summary figures of band 8 and 9, in addition to grain size distribution along band 5 and 6, are in appendix I.

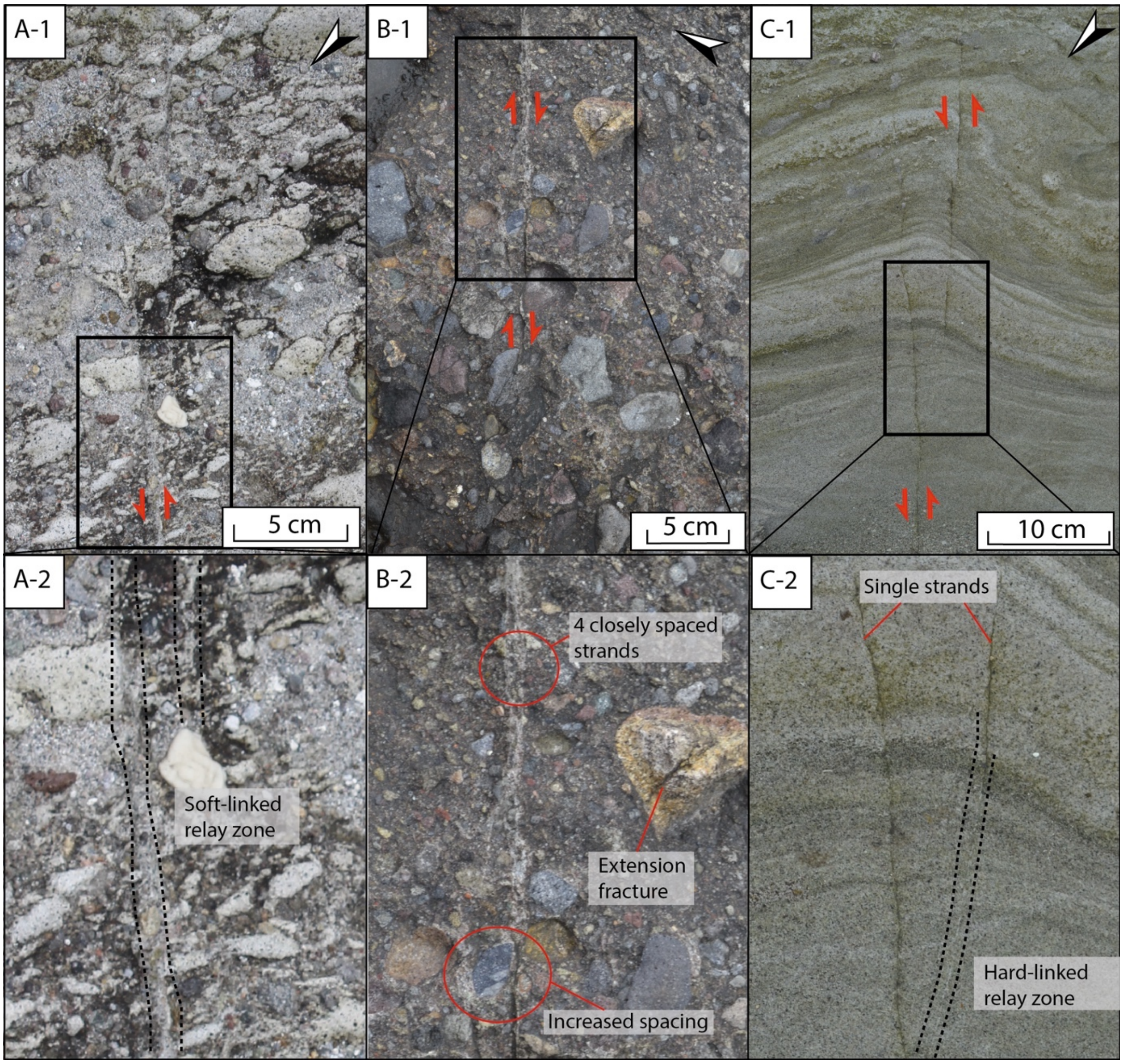

Figure 5.12: Field photos of low-displacement incipient bands. A-1) Photograph of a sinistral incipient band in the ignimbritic conglomerate unit. A-2) A close-up of a soft-linked relay zone. B-1) Field photo of a dextral incipient band in a polygenic volcanic breccia. The band consist if several narrowly spaced strands. B-2) A close-up of the band in B-1. Notice that the band splits into two zones around a mafic lapilli clast. C-1) A photograph of a sinistral incipient band comprised of two linking segments in a stratified medium tuff unit. C-2) A zoom-in on the hard-linked relay zone. The bounding strand is very thin, and barley exposed (marked by the dashed borders).

Figure 5.13 summarises the field observations and quantitative data recorded along band 5. The band is 3.8 metres long and is located on the western flank of the Cuesta. It dissects several tuff units, one ignimbritic coarse lapilli-tuff unit and one matrix-supported ignimbritic conglomerate unit (Fig.5.13c). The thickness of one single strand varies by lithology, but rarely exceeds 1 millimetre. Band 5 generally crops out as a dark line that constitutes a minor (approximately 1 mm) depression in the host rock. The tip point of the DB towards the NW is marked by a red redox front. The band exhibits a sinistral shear displacement, which varies between 0 millimetres at the band tips to a maximum displacement (D_{max}) of 9 millimetres.

Three segments are distinguished and linked together by two relay zones: one narrow (2 cm wide and 9 cm long) extensional relay towards the NW (Fig. 5.13b, marked as relay zone 1), and one wider relay (6 cm wide and 49 cm long) towards the SE (Fig 5.13b, marked as relay zone 2). Relay zone 1 is comprised of two DBs that curve towards each other and join, in which it forms an extensional stepover geometry. The relay zone is located in a cross stratified coarse tuff unit. Relay zone 2 is hard-linked at one end (towards SE) by two thin linking bands, whereas the other free-tip segment dips out in a horsetail arrangement of extension fractures (Fig. 5.13 b). Relay zone 2 is associated with the highest measured displacement (9 mm) and is characterised by an increased number of strands and higher cumulative width. Additionally, relay zone 2 is situated in an ignimbritic conglomerate unit and consists of several thin DBs. While band 5 in the other units, generally is comprised of one thin strand of 1 millimetre. However, in the very coarse tuff unit, the band appears as a thicker strand of 8 millimetres, but this may be due to alteration around the band which makes the band seem to be wider than it is in reality. Moreover, no displacement measurements were conducted in the very coarse tuff unit due to absence of displacement markers.

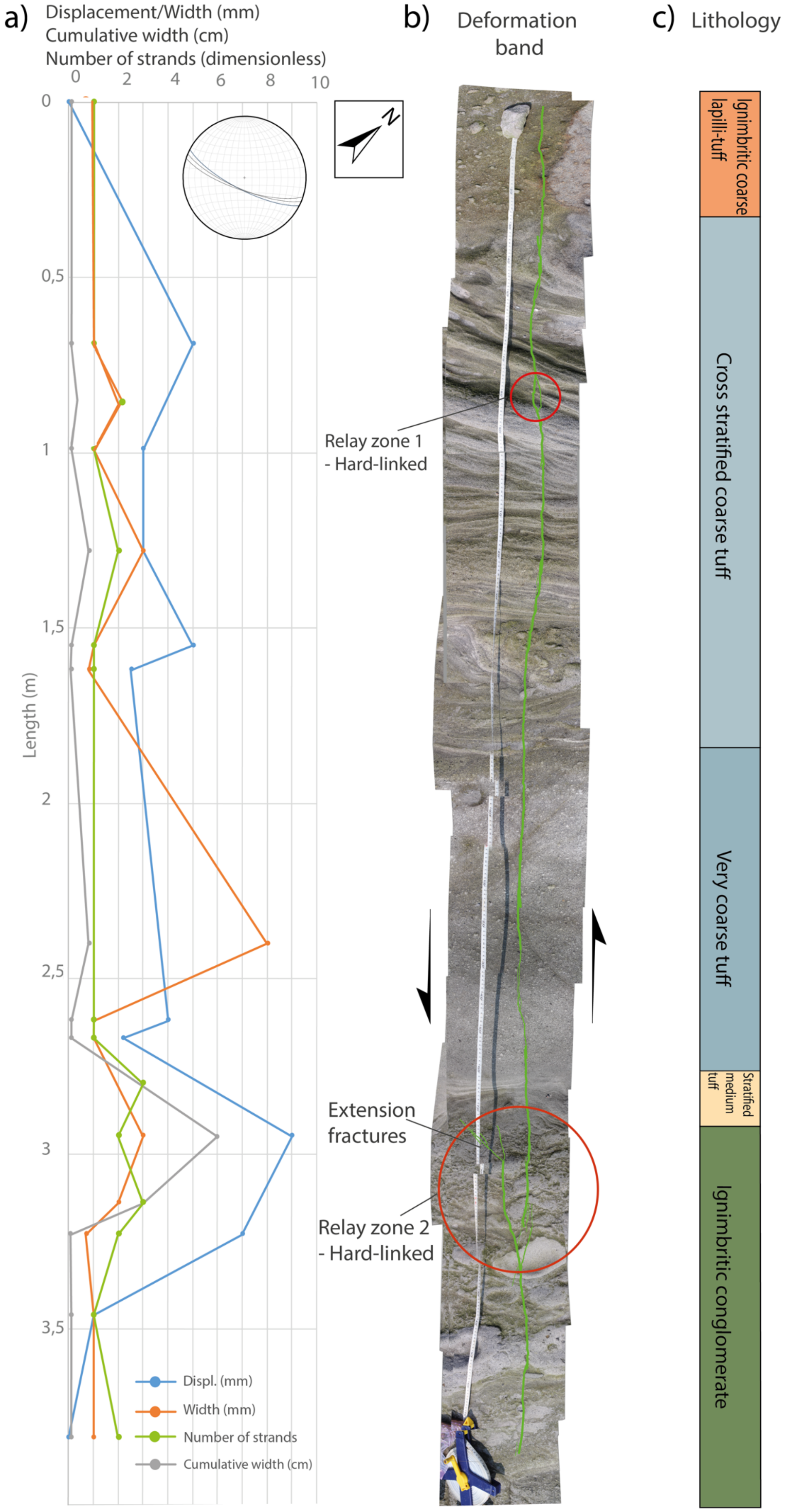
a)
Displacement/Width (mm)
Cumulative width (cm)
Number of strands (dimensionless)
0
2
4
6
8
10
0
0,5
1
1,5
2
2,5
3
3,5
Length (m)
Displ. (mm)
Width (mm)
Number of strands
Cumulative width (cm)
N
b)
Deformation band
Relay zone 1
- Hard-linked
Extension fractures
Relay zone 2
- Hard-linked
c)
Lithology
Ignimbritic coarse lapilli-tuff
Cross stratified coarse tuff
Very coarse tuff
Stratified medium tuff
Ignimbritic conglomerate

Figure 5.13: Summary figure of band 5; the location of band 5 is shown in Figure 5.11A. The top of the figure point towards the NW, A) A diagram over different parameters along the band. Displacement and width are measured in millimetres, cumulative width is displayed in cm and the number of strands is dimensionless. The lower-hemisphere stereonet shows the orientation of band 5. B) Photomosaic over band 5 with green line drawings illustrating the DB. Kinematic indicators are displayed by black arrows. Zones of interest is highlighted with red circles. C) A block diagram of the lithology along the band.

Figure 5.14 summarises the quantitative data and field observations of band 6. The band is 3.6 metres long and is situated a couple metres to the north of band 5. Similar to band 5, band 6 exhibits a sinistral shear movement and crops out a slightly low relief dark line. It dissects four different units: two tuff units, one fine lapilli-tuff unit and one ignimbritic conglomerate unit. The displacement distribution fluctuates between zero displacement at the band tips to 6 millimetres at the central part of the band. Band 6 consists of four segments where two segments are divided by a clast-supported fine lapilli unit where the band is not seen (Fig. 5.14b). Relay zone 1 links up two of the segments into a narrow (0.5 cm wide and 5 cm long), hard-linked lens shape and may be connected to a change in lithology from fine lapilli tuff to medium tuff. Relay zone 2 are wider (6.5 cm) and longer (40 cm) than relay zone 1 and is hard-linked at the northwestern end by one single linking strand (Fig. 5.14b). The southeastern part of the relay it consists of one free tip with one associated extension fracture. This relay zone is associated with D_{max} and increased cumulative width between the strands. As with band 5, the maximum displacement of band 6 is located in connection to a relay zone.

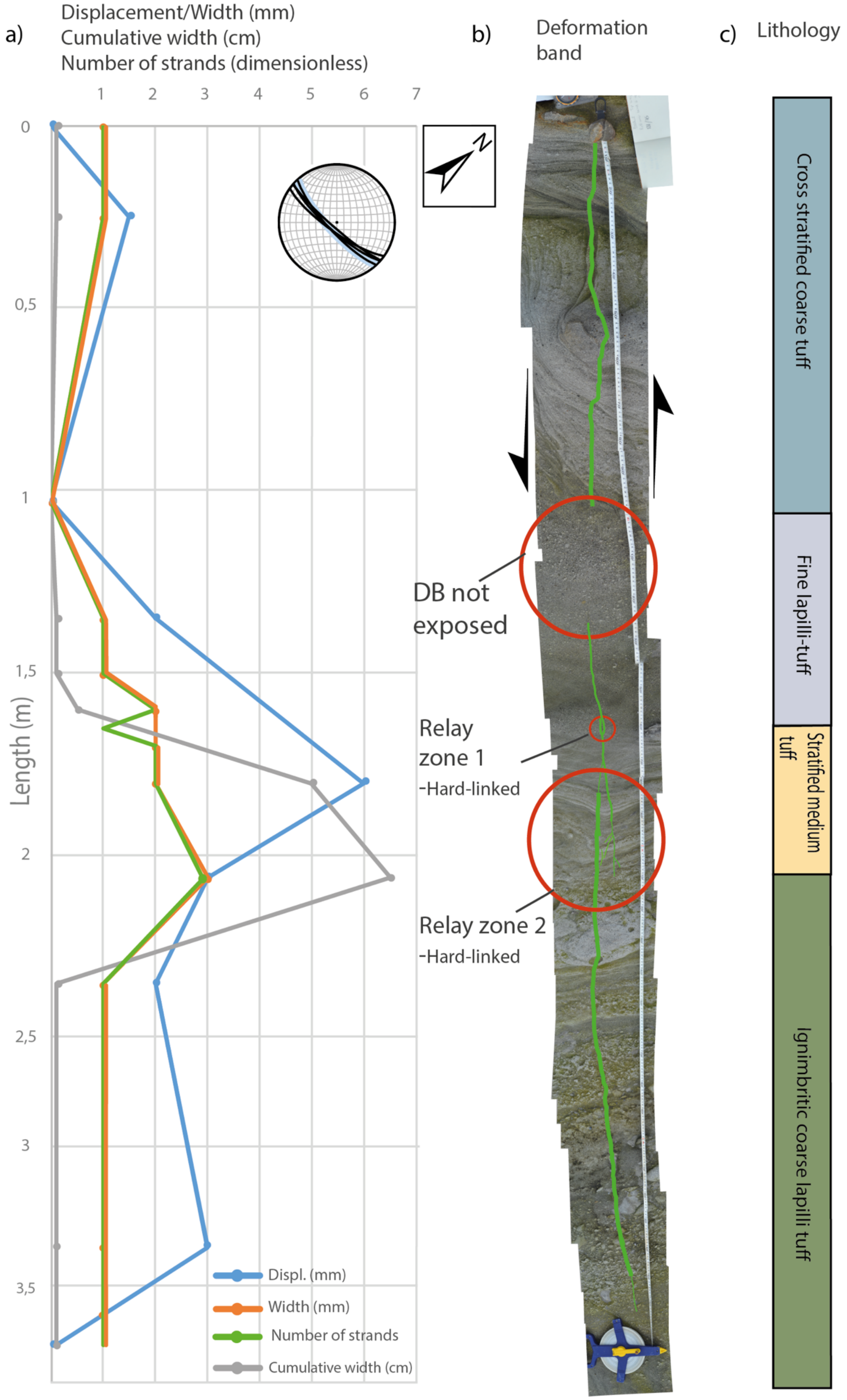
a)
Displacement/Width (mm)
Cumulative width (cm)
Number of strands (dimensionless)
1
2
3
4
5
6
7
0
0,5
1
1,5
2
2,5
3
3,5
Length (m)
N
Displ. (mm)
Width (mm)
Number of strands
Cumulative width (cm)
b)
Deformation band
DB not exposed
Relay zone 1
-Hard-linked
Relay zone 2
-Hard-linked
c)
Lithology
Cross stratified coarse tuff
Fine lapilli-tuff
Stratified medium tuff
Ignimbritic coarse lapilli tuff

Figure 5.14: Summary figure of band 6: the location of band 6 is shown in Fig 5.11B. The top of the figure point towards the NW a) A diagram showing different parameters along band 6. Displacement and width is measured in mm, cumulative width is displayed in cm and number of strands is dimensionless. The lower-hemisphere stereonet shows the orientation of band 6. b) Photomosaic over band 6 with green line drawings illustrating the DB. Relative movement is displayed by black arrows and zones of interest is highlighted with red circles. c) A block diagram of the lithology along the band.

Microstructural investigation of incipient bands reveals highly comminuted material within the band (Fig. 5.15). Larger mineral grains inside the band are heavily fractured (Fig. 5.15A). Especially extension fractures are noticeable in the minerals inside the band. Moreover, locally open areas with increased porosity and fractured mineral grains with a weak sigmoidal shape are present within the DB (Fig 5.15B). Volcanic glass shards appear to be heavily comminuted inside the band, as seen in Figure 5.15C. Minerals adjacent to the band are also affected by fracturing (Fig. 5.15A) and dark precipitated minerals (probably iron oxides) are present at DB boundaries and inside the band (Fig. 5.15E). Porosity measurements highlight a porosity decrease from 25-30% in the adjacent host rock to 6 to 16% within the band, depending on where the measurements are conducted.

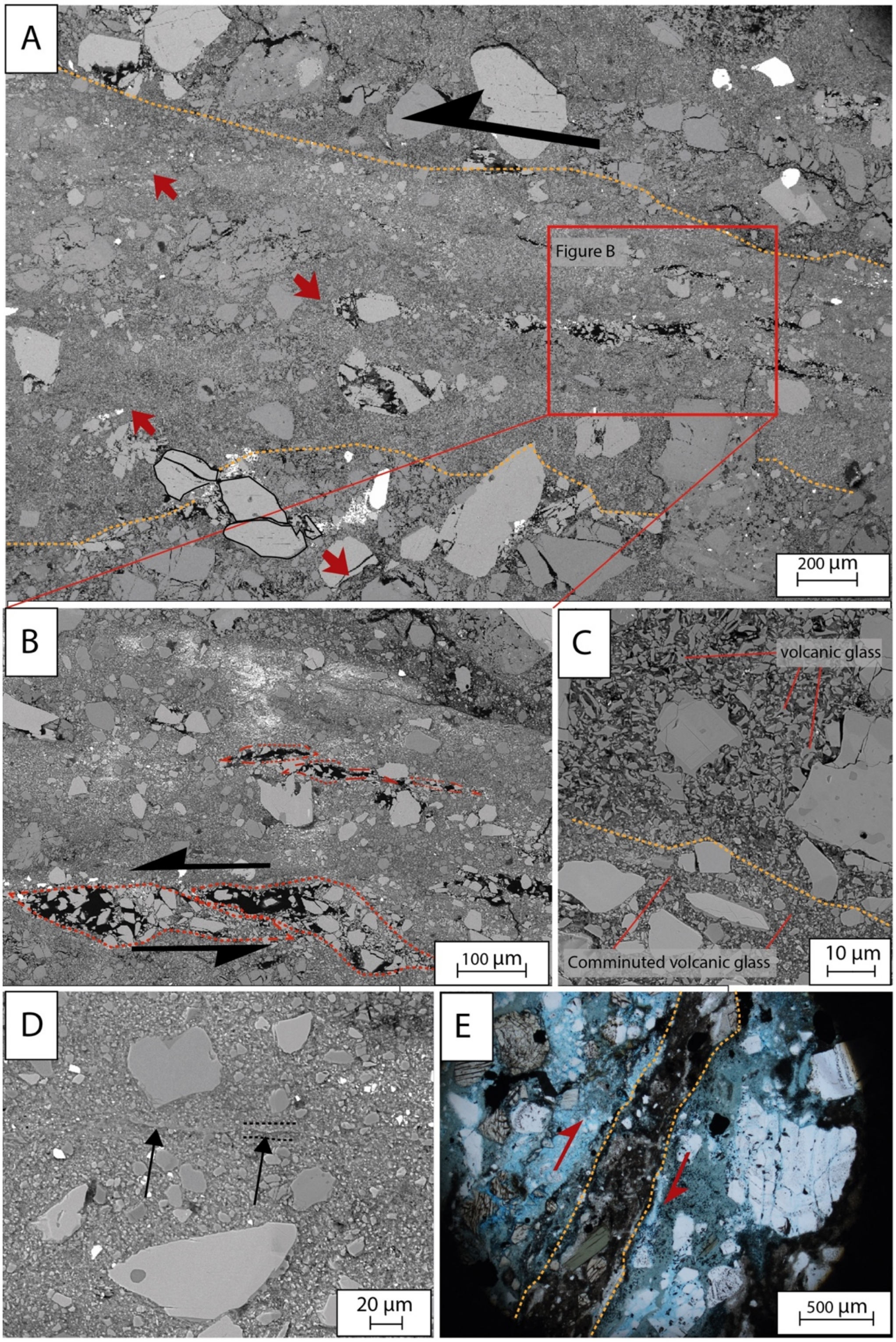

Figure 5.15: Micrographs of an incipient band. DB boundaries are marked by dashed yellow lines. A) A BSE-SEM microphotograph of a part of an incipient band. Mineral grains are affected by extension fractures. B) A zoom-in BSE-SEM micrograph of an incipient band, location outlined in Fig. A, showing sigmoidal shaped and open voids filled with fractured minerals. C) BSE-SEM photograph displaying volcanic glass shards on the outside of the band, and comminuted glass within the DB. D) A BSE-SEM micrograph showing a band-parallel discontinuity within an incipient band. E) A microphotograph in PPL showing an incipient DB. A lot of dark precipitated minerals are observed at the DB boundaries and inside the band. The DB contain fine grained material and a few larger mineral grains where the cleavage is oriented parallel to the band.

5.4 High-displacement mature bands with local slip surface development (5 cm < Dmax <50 cm)

The dm-displacement mature bands are characterized by maximum offset in the range of 5 to 50 centimetres. However, the DBs in the study area are have a maximum offset in the range of 15 to 32 centimetres. The mature DBs commonly comprised of multi-strand networks or clusters of deformation bands. The minimum length of the studied deformation bands is 67 metres. However, the total length of the mature bands is unclear as they extend beyond the studied outcrops. Well-exposed sections of the mature bands (up to 67 metres) were documented and are described below. The thickness of these bands varies from 0.5 to 60 cm and is highly dependent on lithology (Figs. 5.16-5.19), in addition to relay zones where the maximum thickness of 60 centimetres are observed (Fig. 5.19B). Locally, patches of striated slip surfaces occur generally within the DB clusters, but minor slip surfaces are also observed in DB networks. Four mature bands were studied (band 1 to 4 in Fig. 5.11B); summary diagrams of data collected along DB 1 and DB 2 are presented in Figures 5.16 and 5.18, whereas local details from DBs 1 and 2 and shown in Figures 5.17 and 5.19, respectively. More details from the DBs 1, 3 and 4 are found in Appendix II.

Figure 5.16 shows the displacement distribution, thickness variations and strands along DB1 (Fig. 5.11B). The data is collected from a 47-metre-long segment and the lithological units are illustrated in the block diagram. The displacement along the band varies from 5 to 18 centimetres along the band, and the thickness distribution is characterized by two maxima, both of which are associated with dark, low-porosity bombs (Fig. 5.16B). In general, the sudden increase of width of the DB is associated with the low-porosity bombs as the strands are deflected and splay out to "avoid" the bomb. As seen in Figures 5.16B and 5.17D, where the band passes the outer margin of the bomb, the bombs are heavily fractured by extension fractures and some shear fractures. Occasionally, the band will dissect a low-porosity bomb, but then expressed as extension fractures (striking E-W) and locally also as shear fractures in the bomb itself (Fig 5.16C). In contrast, where the DB dissects bombs of pumice no fractures are observed, and the band crops out as a DB network (Fig. 5.16D). The polygenic lapilli tuff to breccia units are commonly associated with a few densely spaced DB strands, whereas the tuff and ignimbritc units commonly have more strands over a wider zone (Fig. 5.16A). An exception is at 25 metres where a striated slip-surface crops out in a clast-supported ignimbritic coarse lapilli-tuff unit (Fig. 5.16E). The band at this point is characterised by a dense and narrow cluster with a local slip surface.

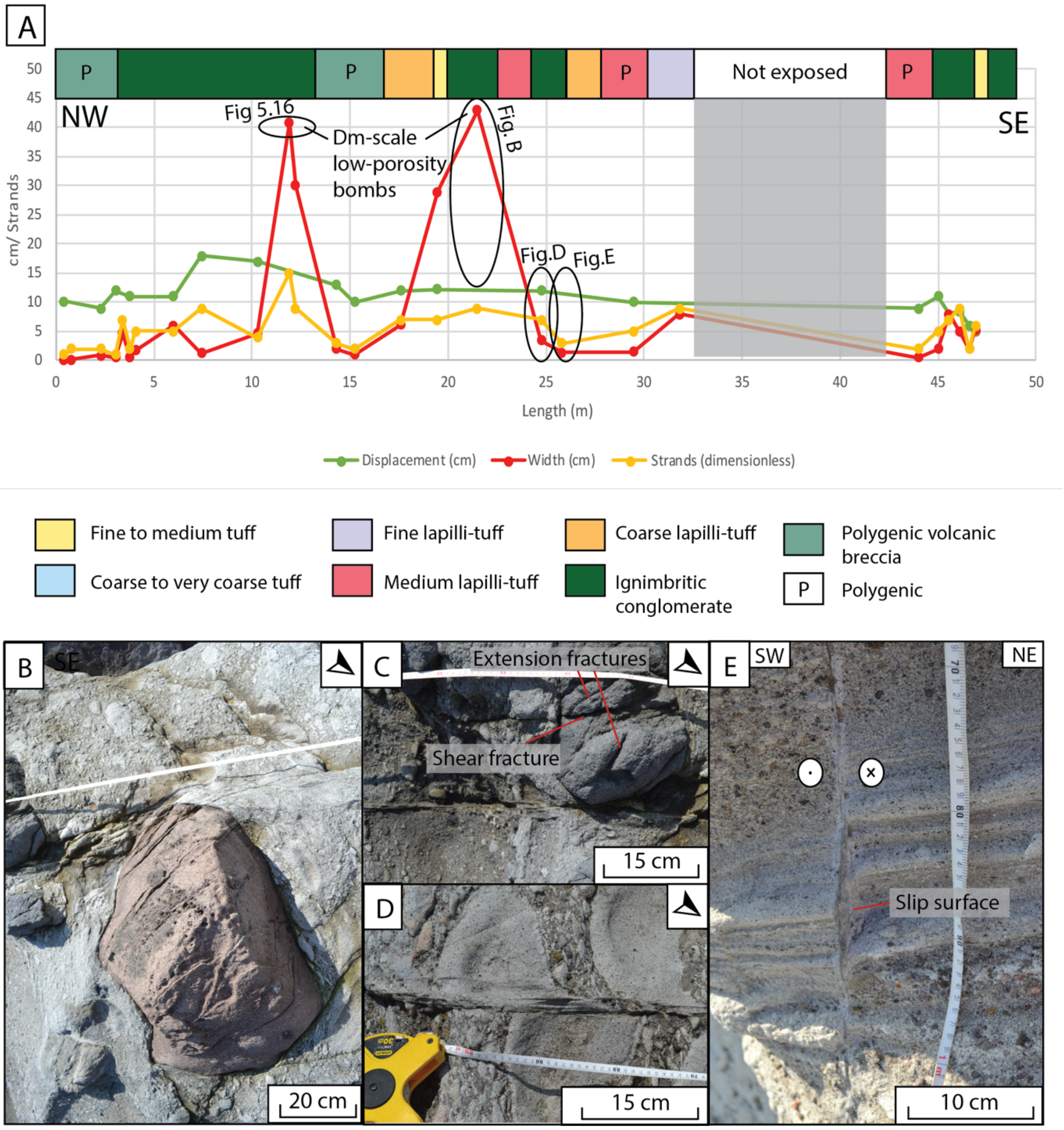

Figure 5.16: Summary of the field data from the DB 1. A) A diagram showcasing the displacement (green plot), width (red plot) and number of strands (yellow plot) collected alongside band 2. The block diagram presents the lithology that the band dissects. B) Outcrop photo of the interaction between the DB and a mafic bomb. C) Shear and extension fractures in a mafic bomb as the bomb is dissected by the deformation band. D) Field photo of a sheared pumice clast. DB development within the pumice. E) Cross sectional view of a cluster with a developed slip surface with striations.

Figure 5.17A displays a more detailed section from DB 1 (location marked in Fig 5.16), Figure 5.17B shows a line drawing of the band with associated lithology, and Figures 5.17 C and D presents close-up photographs of areas of interests. The displayed section extends over two lithologies: ignimbritic conglomerate and polygenic volcanic breccia. In the volcanic breccia unit (marked in turquoise in Fig. 5.17B), slip has been localized onto several, relatively dispersed, patches of slip surfaces, whereas extension- and shear fractures are the dominating structures in the low-porosity volcanic bombs (Fig. 5.17C). However, a few DBs are found in the matrix of coarse tuff.

Deformation in the ignimbritic conglomerate is expressed by DBs (marked in green in Fig 5.17B). The majority of slip is distributed between two clusters (pointed out on Fig. 5.17D). Where the cluster towards southeast accommodates an offset of approximately 8 centimetres, and the northeastern cluster exhibits an offset of approximately 4 centimetres. The total offset of the band at this point is not known, but the nearest known displacement is measured to be 16 centimetres. Accordingly, an offset of roughly 4 centimetres is distributed on the rest of the DB strands in the ignimbritic conglomerate. The spacing between the two clusters in the ignimbritc conglomerate increases towards the dark, low-porosity bomb, as the width of the DB zone expands from 8 to 26 cm (Fig 5.17 B). ENE-WSW striking linking DBs tie the two clusters together. On the southernmost “stoss side” of the bomb, a narrow zone of elevated relief of the ignimbritic conglomerate appears to be accreted (Fig. 5.17D). Intense fracturing of the mafic bomb occurs on the southeastern side. Most of the fractures in the bomb are extension fractures and strike E-W. Although, two fractures oriented parallel with the shear direction and are classified as shear fractures.

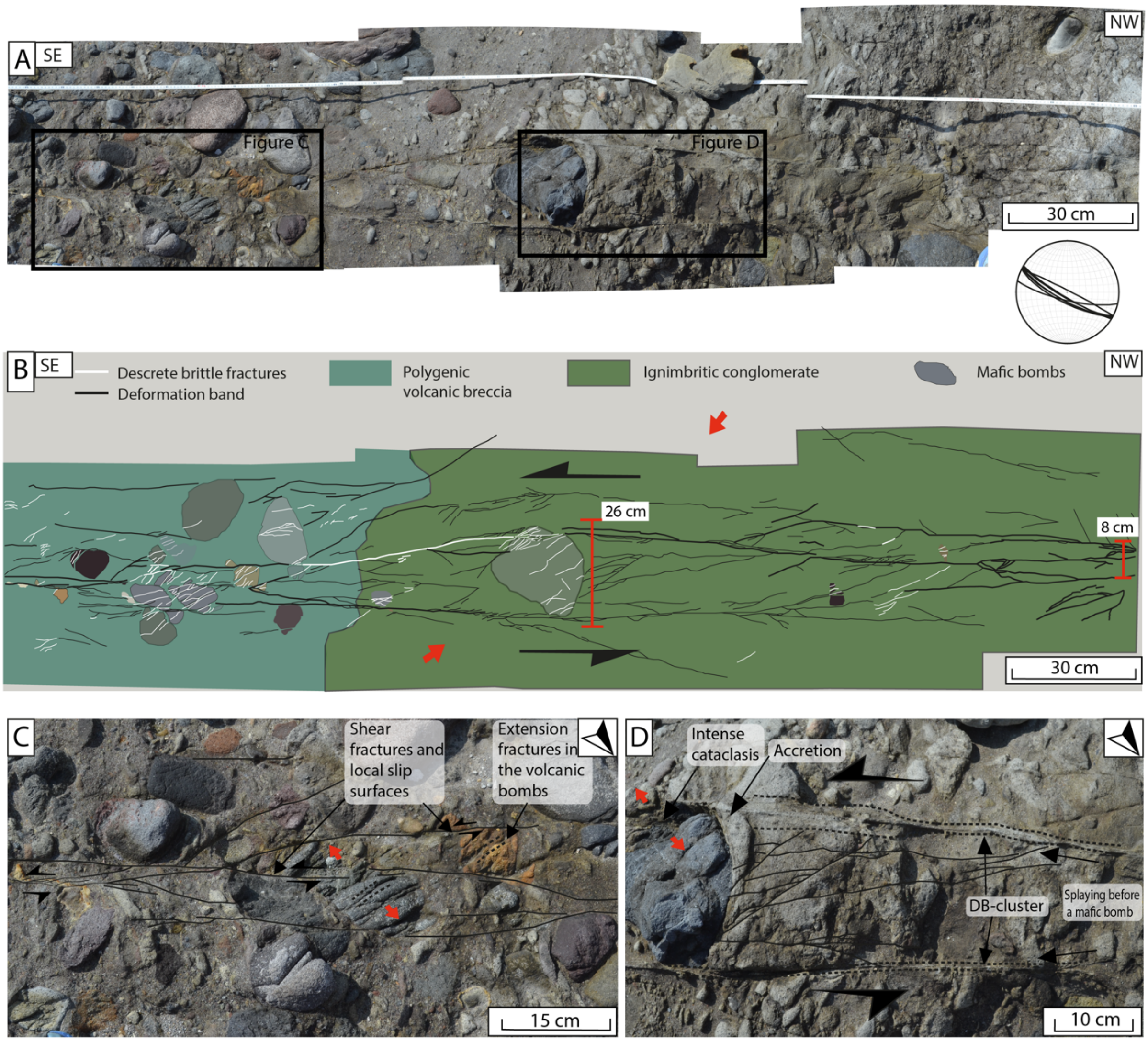

Figure 5.17: A) Photomosaic of a section of DB 1. The lower-hemisphere stereoplot displays the orientation of the band. B) A line drawing of the deformation band from A with lithology. C) Picture from the field showing the deformation in the polygenic volcanic breccia. D) A close-up photo of the different structures, and a mafic bomb in the ignimbritc conglomerate.

The displacement distribution, width, number of strands and lithology along DB 2 (67-metre-long) is presented in Figure 5.18. DB 2 exhibits a dextral shear movement and the displacement along the band varies from 5 to 30 centimetres. The width fluctuates between 2 and 59 centimetres, and the number of strands ranges from 2 to 27. Moreover, DB 2 includes two main segments linked together by a soft-linked relay zone (Fig. 5.18B). An interesting feature in the plot is the coinciding peak in the all the three graphs after 40 metres. These peaks correlate to the relay zone (Fig. 5.18B) where the band steps through several DB strands towards the north**.** The maximum displacement (30 cm) of DB 2 is measured in this relay zone and is cumulative value (meaning that the displacement is the sum of offset measured at several strands) for the whole zone. Additionally, the peaks coincide with a fine and stratified tuff layer (Fig. 5.18A). The highest number of DB strands are generally associated with tuff and ignimbritc layers (Fig. 5.18A). Whereas the DB in the polygenic units are narrow and comprised of a few strands (Fig 5.18A).

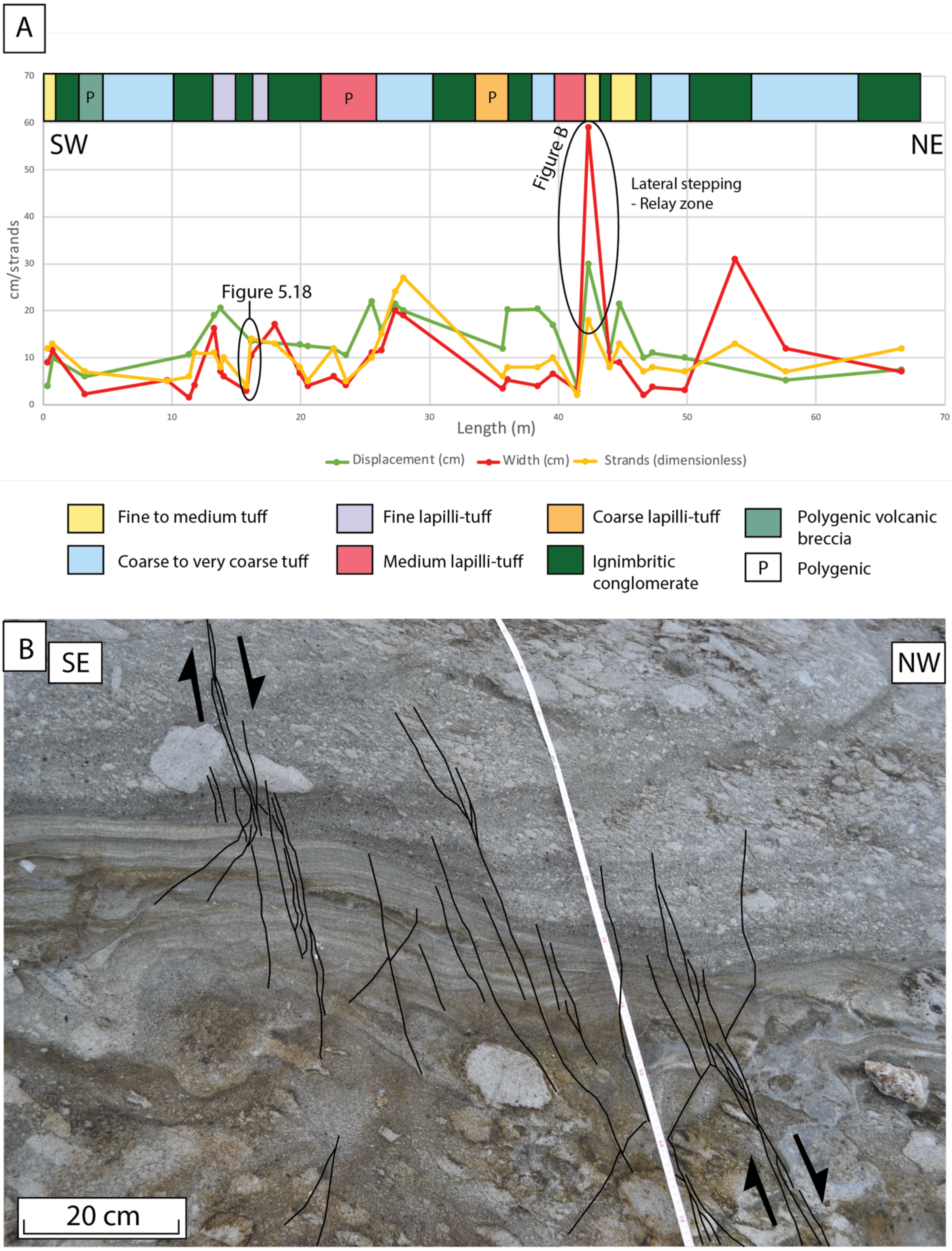

Figure 5.18: Summary of the field data from DB2. A) A diagram that present the displacement (green plot), width (red plot) and number of strands (yellow plot) collected alongside DB2. The block diagram presents the lithology that the band dissects. B) A field photo of the left-stepping and soft-linked relay zone. Black line drawings indicate DBs.

Figure 5.19 shows an example of the different structural styles of a close-up section of the DB 2 (location marked in Fig. 5.18A). The displayed section of DB 2 in the photomosaic (Fig. 5.19A) dissects several units; ignimbritic conglomerate, polygenic fine lapilli-tuff, fine to medium tuff and medium lapilli-tuff (Fig 5.19B). The structural style of the DB exhibits large variation within the presented three metres of the photomosaic (Fig. 5.19A). Within the polygenic fine lapilli-tuff, only a few strands crop out as an elevated cluster (0.5 cm thick) (Figs. 5.19B and C). The cluster accommodates all of the shear displacement of roughly 13 centimetres. Further towards NE, in the fine to medium tuff and medium lapilli-tuff, more strands appear around the cluster. Hence, displaying a wider deformation zone. In the ignimbritic conglomerate towards the NE, the band is characterised by a wide (around 32 cm) DB network (Fig. 5.19B). The network constitutes a negative relief compared to the host rock and the shear displacement is distributed across the network by several strands (Fig. 5.19D). Each strand accommodates 0.5 to 2 centimetres offset.

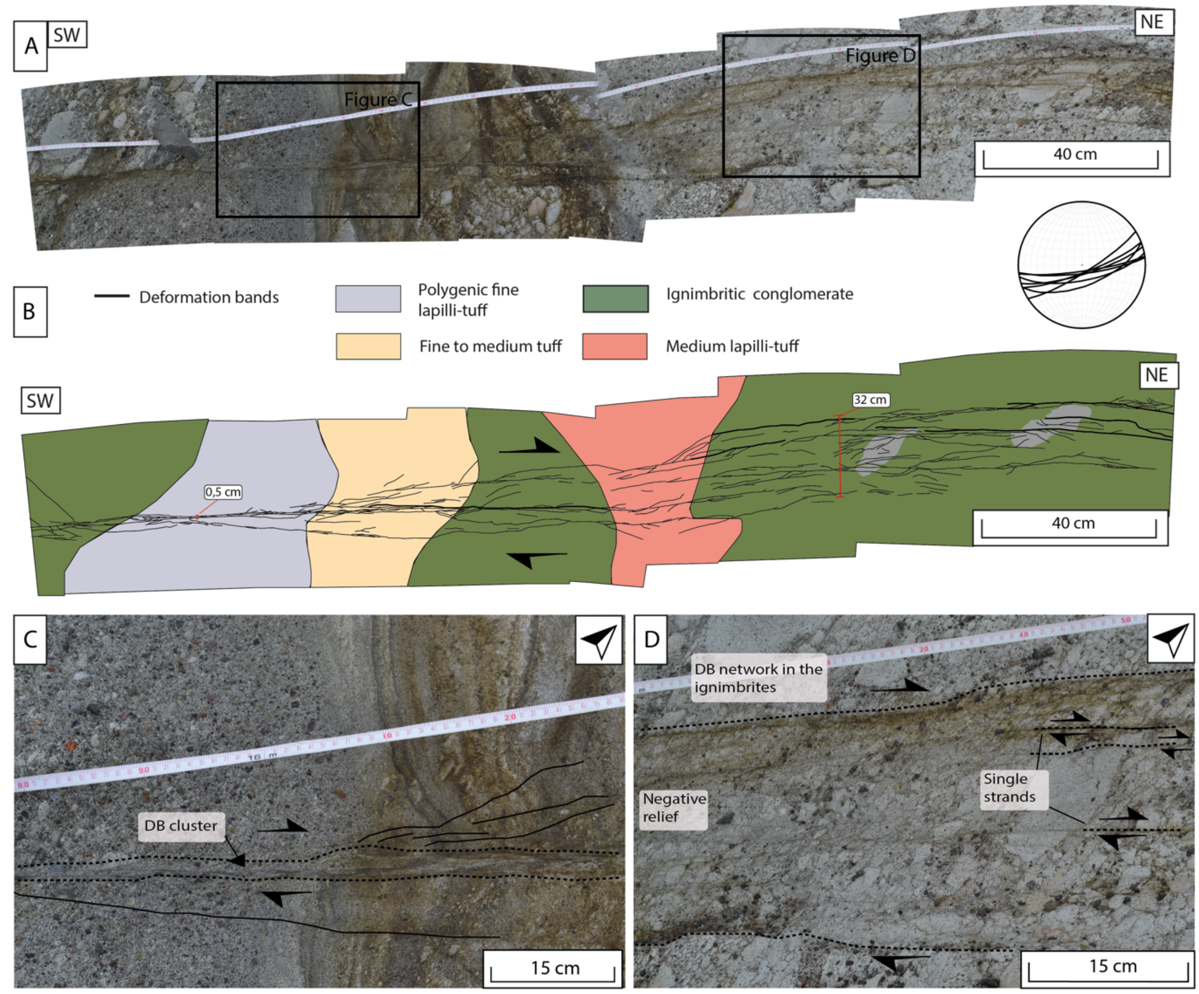

Figure 5.19: A) Photomosaic of a section of the dextral DB2. The lower-hemisphere stereoplot displays the orientation of the band. B) Line drawings of the deformation band from Figure A with lithology and arrows as kinematic indicators. C) Picture from the field showing a DB cluster in polygenic fine lapilli-tuff and fine to medium tuff. D) A close-up photograph of the DB network in clast-supported ignimbritic conglomerate.

5.5 Fully developed faults (D_{max} > 0.5 metres)

Fully developed faults are characterised by a relatively consistent and clear fault core (*sensu* Caine et al. 1996) with some local exceptions, and the studied faults feature offsets ranging from 0.5 to 2.6 metres. Generally, one or several thoroughgoing slip surfaces accommodate the shear displacement. As presented in the following, a well-defined damage zone (*sensu* Caine et al., 1996; Peacock et al. 2017) is present in some lithologies, while the damage zone (DZ) is less distinct or not fully developed in other units. Three faults have been mapped: two sinistral faults at study area A and one dextral fault at study area B. Two faults (Faults 1 and 2 in Area A; see Fig. 5.11B) have been surveyed manually (on the ground, in the field) along their exposed lengths, which amount to 33 and 37 metres, respectively. A third fault (Fault 3 in Area B; see Fig. 5.1) was mapped over a significantly longer area as the fault was exposed for an along-strike length of 332 m; for this fault, a UAV was used to complement the data collection and documentation of the fault. The main focus has been on Fault 3; below, Fault 2 is presented jointly and briefly (see Appendix III for more information about Fault 1), before a more detailed description and documentation of Fault 3 is presented.

In Area A (Fig.5.1), the northern fault (Fault 1; Fig 5.11B) have a D_{max} of 1.83 metres and a minimum offset of 1.20 metres, and an outcropping trace length of 33 metres. The southern outcropping fault in Area A (Fault 2; Fig 5.11B) displays a maximum shear displacement of 2.60 metres and a minimum of 1.70 metres within a trace length of 37 metres. The thickness of the fault cores varies between 3.5 to 53.5 centimetres and the width of the damage zones range from non-existent to 2.6 metres.

The variable structural style of the faults in study area A is illustrated by Figure 5.20, and commonly includes thick DB networks and clusters, with through-going slip surfaces. The displayed section of Fault 2 (Fig. 5.20 D and E) consists of one main segment in the SE and splays out to two segments towards the NW in the polygenic volcanic breccia (marked in turquoise in Fig. 5.20E), as the fault steps left-laterally.

In the polygenic volcanic breccia unit, the fault exhibits a wide zone of extension fractures and the slip is partitioned onto two dispersed principal slip surfaces (Fig 5.20G). In addition, minor slip surfaces accommodate minor shear displacement and are located in-between the principal slip surfaces. A dense network of DBs, including up to five densely spaced slip surfaces, characterises the deformation in the ignimbritic conglomerate (marked in green in Fig 5.20E). One principal slip surface has been recognised in the DB network cutting the ignimbritic conglomerate. Several other minor slip surfaces in the DB network distributes the rest of the displacement.

The damage zone is also widespread in the form of extension fractures in the low-porosity bombs in the volcanic breccia. While the damage zone in the ignimbritic conglomerate units generally consist of sparsely separated single DBs. This variable appearance of the damage zone is evident in Figure 5.20A where metre-scale low-porosity bomb (diameter of 2.6 metres) is heavily fractured by both extension and shear fractures, while only a few DBs crops out in the damage zone in the surrounding ignimbritic conglomerates.

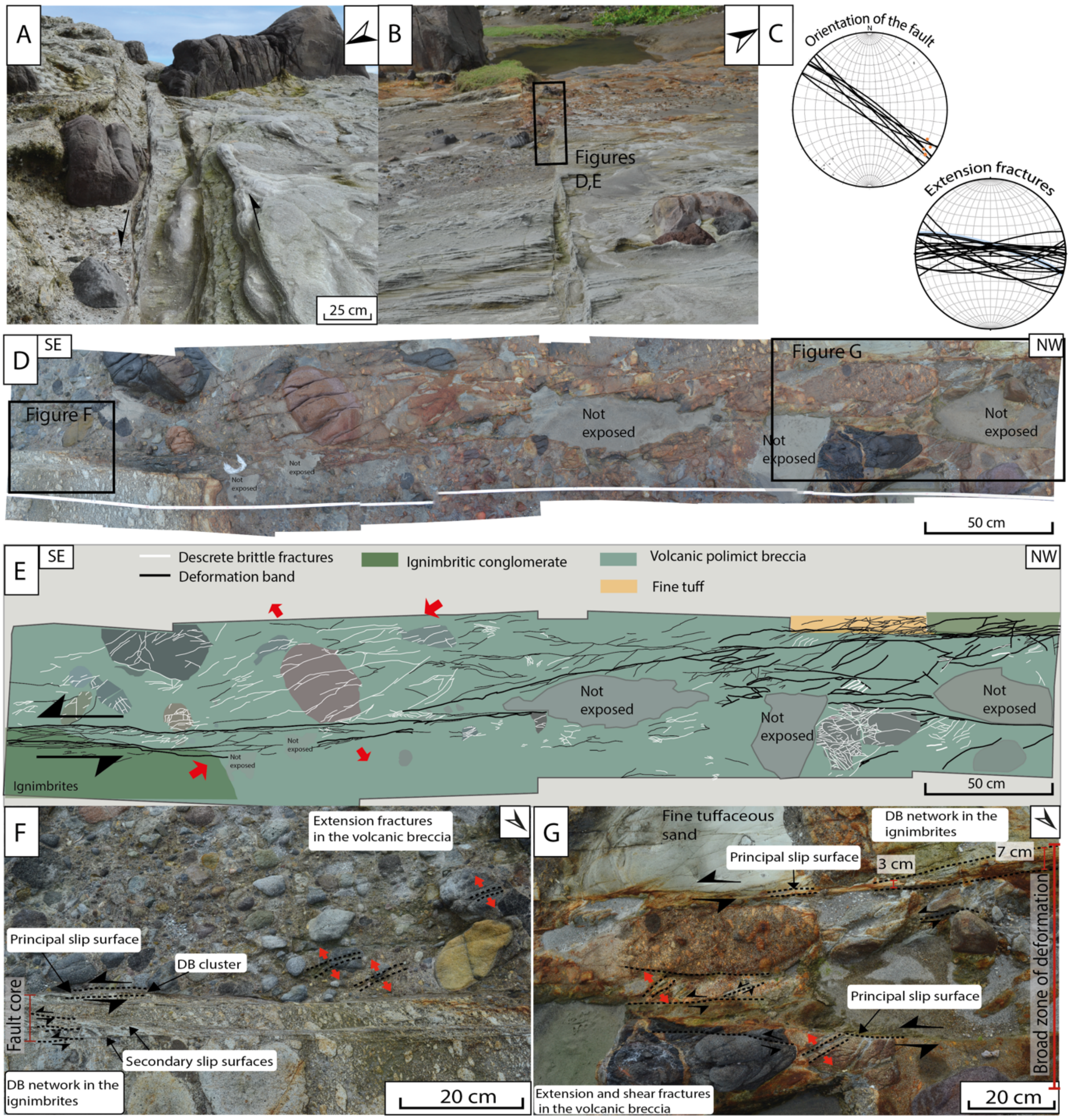

Figure 5.20: Summary figure of sinistral fault 2. A) Outcrop photograph from fault 2, displaying brittle deformation (extension and shear fractures) in the damage zone in mafic volcanic bombs (the biggest is 2.6 m wide) and two principal slip surfaces in the fault. B) Field photo over Fault 2 towards NW. The location of Figures D and E are outlined in black. C) One lower-hemisphere stereoplot over the main orientation of the fault, yellow lines mark the orientation of the striations measured on slip surfaces. The other plot displays the orientation of the extension fractures. D) Photomosaic of a section of fault 2 with location of figure F and G marked in black. E) A line drawing of the structural lineaments of the fault with lithology. F) Outcrop photograph that show a DB network with several clusters and slip surfaces. Note the extension fractures in the polygenic volcanic breccia. G) A close-up photo of the deformation structures. Two main slip surfaces are observed with increased spacing compared to figure F. Shear and extension fractures dominate the mafic bombs. The southwestern cluster increase in thickness when entering the ignimbritic conglomerate.

The studied fault zone in Area B (Fig 5.1), Fault 3, is mapped onto UAV imagery and presented in Figure 5.21. The fault zone consists of a widespread fault zone around a central high strain zone comprised of either a fault core with discrete slip or a zone of intense deformation banding where the shear is distributed throughout the zone.

Fault 3 is a dextral strike-slip fault trending NE-SW dips ~80° towards the SE. The damage zone consists of structures (deformation bands and small faults) that can be divided into two groups; dextral in blue (0-90°) and sinistral in red (90-180°) (Fig. 5.21a). The red sinistral lineaments are striking NW-SE and are regarded as antithetic structures relative to the main (dextral) fault. The damage zone thus consists of synthetic (dextral) and antithetic (sinistral) single bands, clusters and networks of DBs, and/or small faults. In addition, there are WNW-ESE striking extension fractures. The exposed part of the fault (332 metres) is comprised of three left-stepping main segments (Fig 5.21B). Contractional steps (marked with red circles and labelled in Fig. 5.21B) connect the segments together and comprises areas of increased structural complexity within the damage zone. Such areas are termed linking damage zones (*sensu* Kim et al. 2004) The two linking damage zones are characterised by a high concentration of connecting nodes (high amount of connecting nodes per grid cell; see Fig. 5.21C). Meaning that the structures in the area are highly connected by frequent intersections. Moreover, the contractional steps are comprised of short lineaments and a larger amount of antithetic structures, in contrast to the wall damage zone of the fault segments, where the damage zone is comprised of longer and, preferentially, synthetic structures.

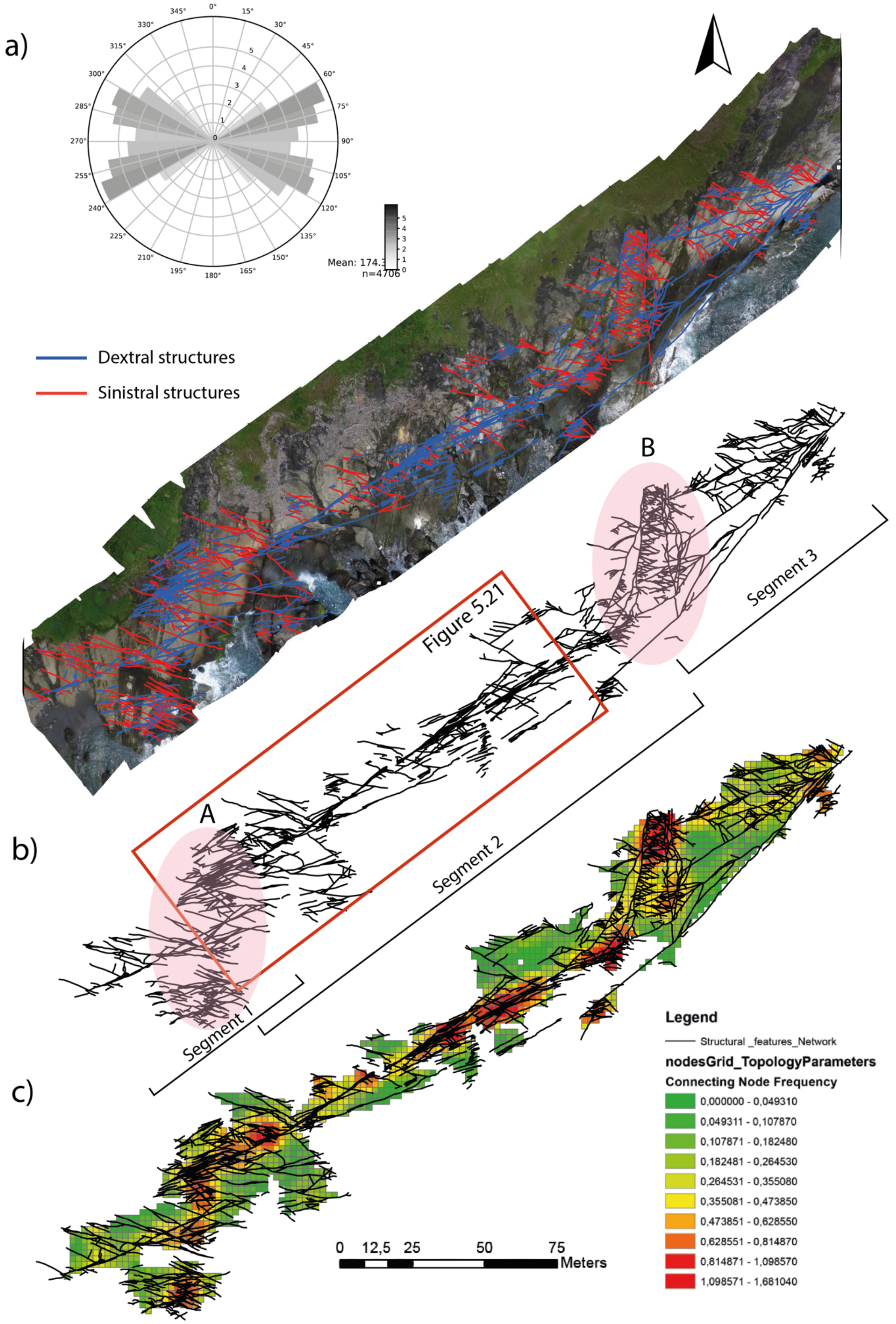
a)
0°
15°
30°
45°
60°
75°
90°
105°
120°
135°
150°
165°
180°
195°
210°
225°
240°
255°
270°
285°
300°
315°
330°
345°
0
1
2
3
4
5
Mean: 174.3
n=4706
Dextral structures
Sinistral structures
b)
A
B
Figure 5.21
Segment 1
Segment 2
Segment 3
c)
0
12,5
25
50
75
Meters
Legend
Structural _features_Network
nodesGrid_TopologyParameters
Connecting Node Frequency
0,000000 - 0,049310
0,049311 - 0,107870
0,107871 - 0,182480
0,182481 - 0,264530
0,264531 - 0,355080
0,355081 - 0,473850
0,473851 - 0,628550
0,628551 - 0,814870
0,814871 - 1,098570
1,098571 - 1,681040

Figure 5.21: a) An UAV model over study area B made in Agisoft with mapped sinistral (red) and dextral (blue) structures. A rose diagram over all the mapped structures shows the prevailing structural trends. b) Line drawings of the fault zone with local the contractional steps A and B marked in red. Location to figure 5.21 is marked by a red rectangle. c) A map that quantifies the connectivity from 0 to 2 in each grid cell. Where 2 is fully connected fracture network and 0 is completely isolated one.

Segment 1 is 76 metres long, whereas segment 2 is 180 metres long. The contractional step A is characterised by a high intensity of connecting nodes and branches and has roughly an equal portion of antithetic and synthetic structures (Fig. 5.21). However, the structures generally exhibit a larger range in orientations and tend to have more E-W orientations than what is observed in the wall damage zone (*sensu* Kim et al 2014; Peacock et al., 2017) of the main segments at distance from the contractional steps. The SW part of Segment 2 is characterised by a broad zone of deformation near contractional step A, with a broad damage zone. The segment changes character towards the NE, away from contractional step A, where the slip is accommodated by one or several closely spaced slip surfaces and the damage zone is comprised of a few scattered structures. Even further to the NE, near the central part of segment 2 (Fig. 5.21C), there is a new peak in connecting node frequency, but it is not linked to a relay zone. This part of the fault is located in an alternating sequence of ignimbritic conglomerate and tuffs, where there is no clear boundary between the fault core and damage zone, as the strain is distributed over a wide zone of deformation bands (see Fig. 5.24). Most of the structures in the central area of segment 2 are synthetic to the main fault, and few antithetic structures are mapped in connection with this zone (Fig 5.21A).

The contractional step B, between segment 2 and 3, (Fig. 5.21B) is characterised by short, and generally antithetic (Fig 5.21A), shear fractures and DBs bound by three linking N-S striking minor reverse faults. This complex linking damage zone constitutes a peak in connecting nodes frequency (Fig. 5.21c). The outcropping part of segment 3 is measured on the UAV model to be around 79 metres long. The damage zone of segment 3 is characterised by a wide zone of synthetic DBs and a well-defined fault core is not recognised. Moreover, the orientation of the synthetic structures changes from an average of 055° in segment 2 to 044° in segment 3.

135 metres of segment 2 is investigated in detail (marked by a red square in Fig. 5.21B). The offset of the studied fault segment fluctuates between 0.7 and 2.66 metres (Fig. 5.23) and is distributed either in (i) a wide zone of intense deformation banding (up to 2.2 m wide) with or without short discontinuous slip surfaces, or (ii) onto one or several discrete slip surfaces and may include fault rocks (cataclasites). A distinct damage zone consisting of extension and shear fractures is associated with the discrete slip-dominated fault core. To examine the variable structural style of the fault in detail, representative examples from the different styles are presented in the following. Localities 1 to 6 and 11 (Fig. 5.22) are characterised by a zone of

intense deformation banding and are located in alternating tuffaceous and ignimbritic lapilli-tuff to conglomerate layers. Whereas localities 7 to 10 (Fig.5. 22) are slip surface-dominated and situated in a polygenic unit with grain size ranging from fine lapilli to bombs. All localities and rock samples are marked on the structural map in Figure 5.22.

Figure 5.22: Line drawing of the studied segment 2 and damage zone with localities and sample positions. Location shown in Fig 5.20B by the red rectangle.

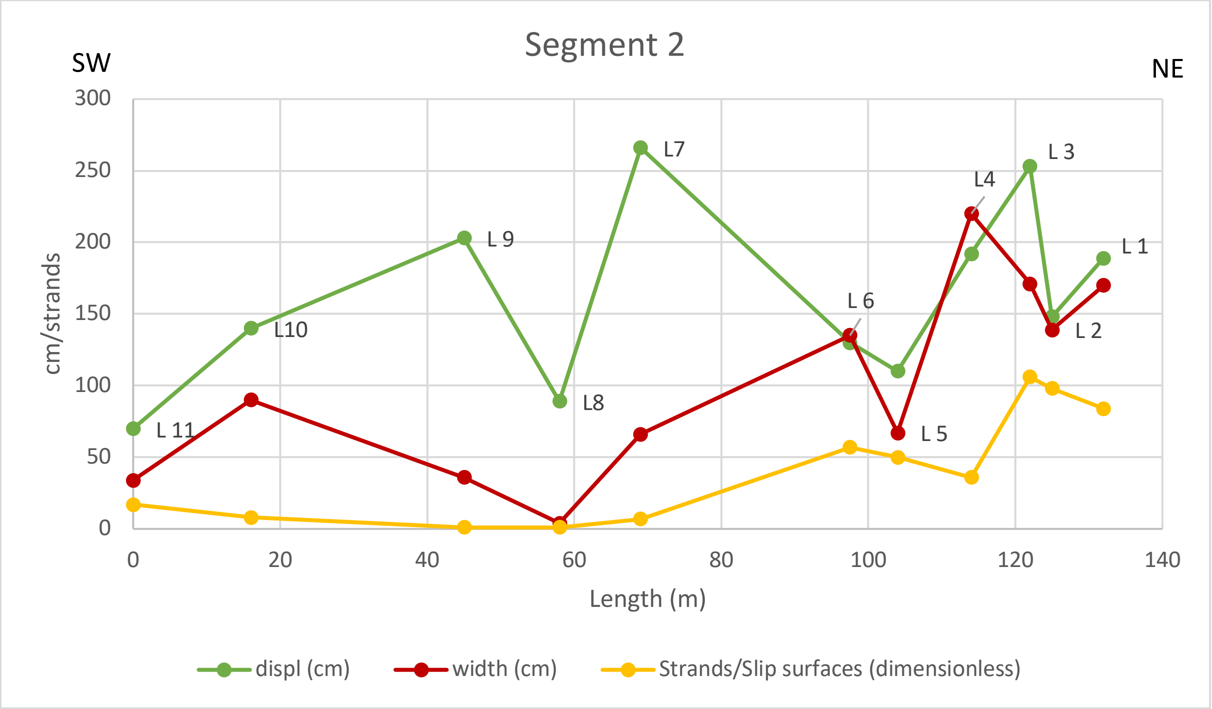

Figure 5.23: A chart of the displacement (green plot), width (red plot) and number of strands (yellow plot) collected along the studied section of segment 2. L# = Localities number. For location se Fig. 5.20B; location marked by the red rectangle, and Fig 5.21 for the positions of the localities.

Fault core dominated by distributed shear

The fault is characterised by densely spaced DB clusters and networks where the fault dissects the ignimbritic tuff to conglomerate layers (Fig. 5.22). The shear-offset in these locations ranges from 1.10 to 2.53 metres (Fig. 5.22) and is distributed by a severely deformed DB zone. Moreover, the width of the shear-zone that varies between 0.67 to 2.2 metres (Shear zone on Fig 5.22). Any discrete fault core is hard to distinguish as the displacement is accommodated by a large number of DBs throughout the area, as seen on Figure 5.21. The DB-clusters and networks are resistant to weathering as they crop out as elevated thick bands compared to the host rock. Figure 5.24 displays four examples from the DB-dominated parts of the fault. Discrete slip surfaces are observed locally in the middle of thick clusters of deformation bands (Fig.5.24 B;C;E) and constitutes a depression in the cluster or host rock. As seen on Figure 5.23A most of the slip is localised onto the slip surface (Fig. 5.24B) in the one cluster where sample 1 is collected. The other clusters without a visible slip surface accommodate less displacement. Generally, the ignimbritic units are dominated by widely-spaced thick DB clusters (5 to 10 cm thick) and the tuff layers are deformed as a broad DB network (up to 1 m). The fault is characterised by a zone of intense deformation banding in which the offset is distributed by a high DB-density zone, comprised of 50 to 110 DBs. In the high intensity DB zones many of the DBs have amalgamated together to form thick clusters (between 7 to 14 clusters in the zone) (Fig. 5.24 A-D). At locality 5, as the one shown in Figure 5.24C, slip surfaces are not present.

Near the tip of segment 2 (towards the SW; at locality 11), the fault zone is characterised by wide damage zone comprised of DBs, surrounding a localised slip zone that most likely consists of slip surfaces (Fig.5.24E). The zone of localised slip is weathered down and covered by vegetation and scree (Fig. 5.27). Thus, extensive investigation of the slip surface could not be carried out. The zone of localised displacement accommodates an offset of 0.7 metres which is the lowest displacement measured at fault segment 2. However, the shear offset of the whole fault zone (width=5.81 metres) including the damage zone, is measured in the field to be 2.5 metres. Although, UAV imagery implies that the damage zone in this area is probably more extensive than what has been measured in the field. Networks of deformation bands dominate the broad damage zone (Fig. 5.24 E). These DBs in the damage zone crops out as lighter colour bands with a slightly elevated relief. Generally, the DBs shows a similar orientation as the fault, whereas local stands, and occasionally networks, are oriented ENE-WSW. Average spacing between the strands in the damage zone towards southeast is 6.30 centimetres, while the average spacing in the northeastern damage zone is 3.24 centimetres.

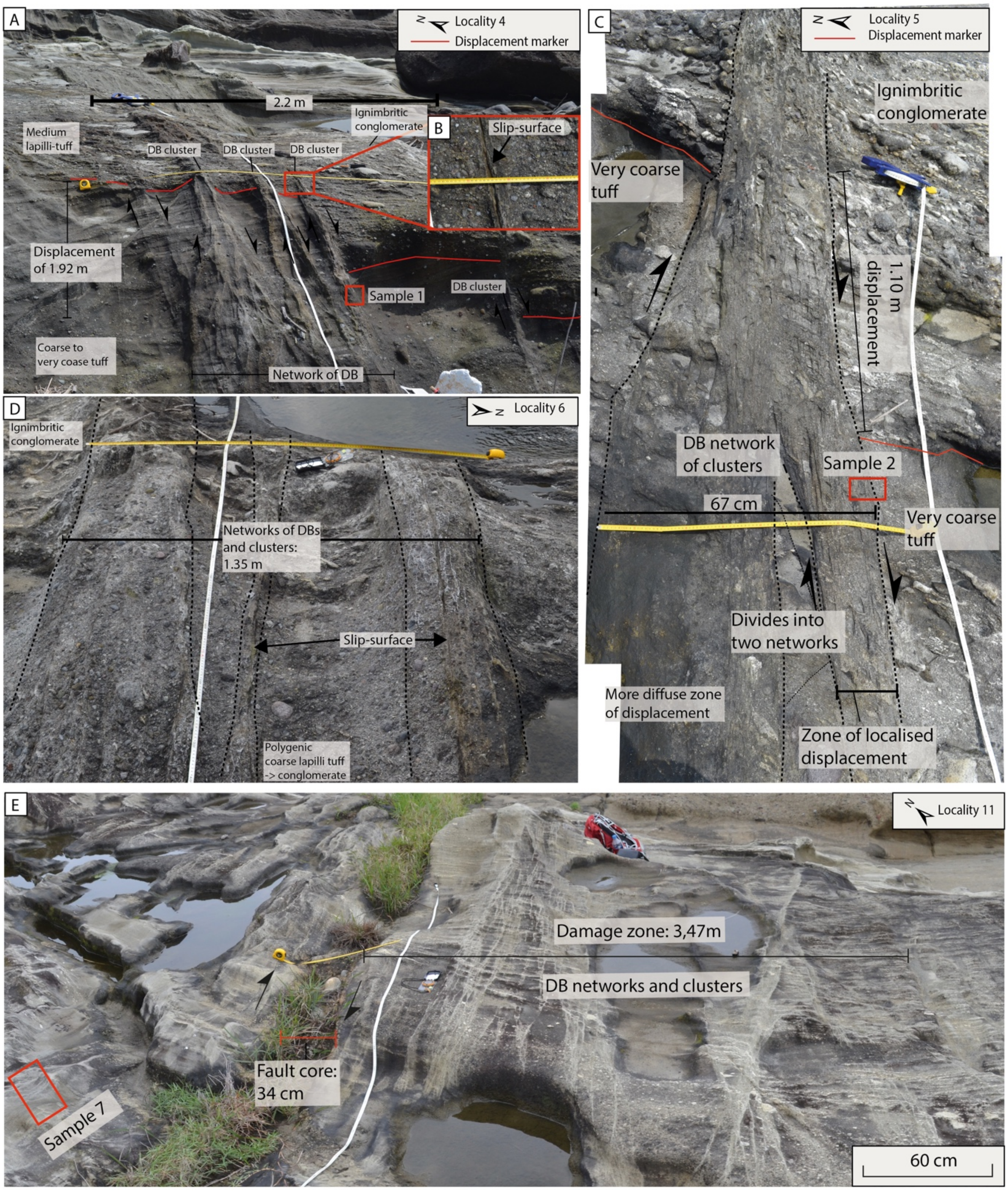

Figure 5.24: Outcrop photographs from DB-dominated parts of the fault. A) Field photo from locality 4. Five thick DB clusters accommodate the shear displacement in the ignimbritic conglomerate, while the displacement is distributed in a wide network of DBs in the very coarse tuff. The two clusters towards the south accommodates most of the displacement. The sample location of sample 1 is outlined in red. B) A zoom-in on the slip surface. Location marked by a red square in A. C) Photograph of locality 5. The displacement of 1.10 metres is accommodated by a dense network of clusters and bands. A very coarse tuff layer work as displacement marker and sample location of sample 2 is marked in red. D) Outcrop photo of locality 6. The fault core is divided into three zones. One broad network of deformation bands toward the

south, a dense cluster with local slip surface development in the middle, and a DB network with a through-going slip-surface towards the north. E) Outcrop photograph of locality 11 and broad zone of formation banding around a localised slip zone. The actual slip surface is covered in vegetation. Sample location of sample 7 is outlined in red.

Rock samples from the DB-dominated parts of the fault reflect field observations and consist either of thick clusters (Fig 5.25) or closely spaced thin, single strands (Fig 5.26). Analyses done in Scanning Electron Microscope (SEM) show a decrease in grain size and increased compaction within the cluster (Fig 5.25D). Also, the grain size distribution is more sorted within the cluster. However, relatively intact and large grains (up to 0.5 mm) are located inside the crushed and compacted DB. Porosity estimation done in ImageJ on BSE-SEM pictures reveals a reduction from 12% in the deformed host rock to 1.6% within the cluster. However, close-up pictures of the matrix (zoomed 750x) discloses large internal variations of grain sizes and the degree of compaction inside the DB cluster (Fig 5.25 E; F; G). Consequently, the micro-porosity will vary throughout the cluster.

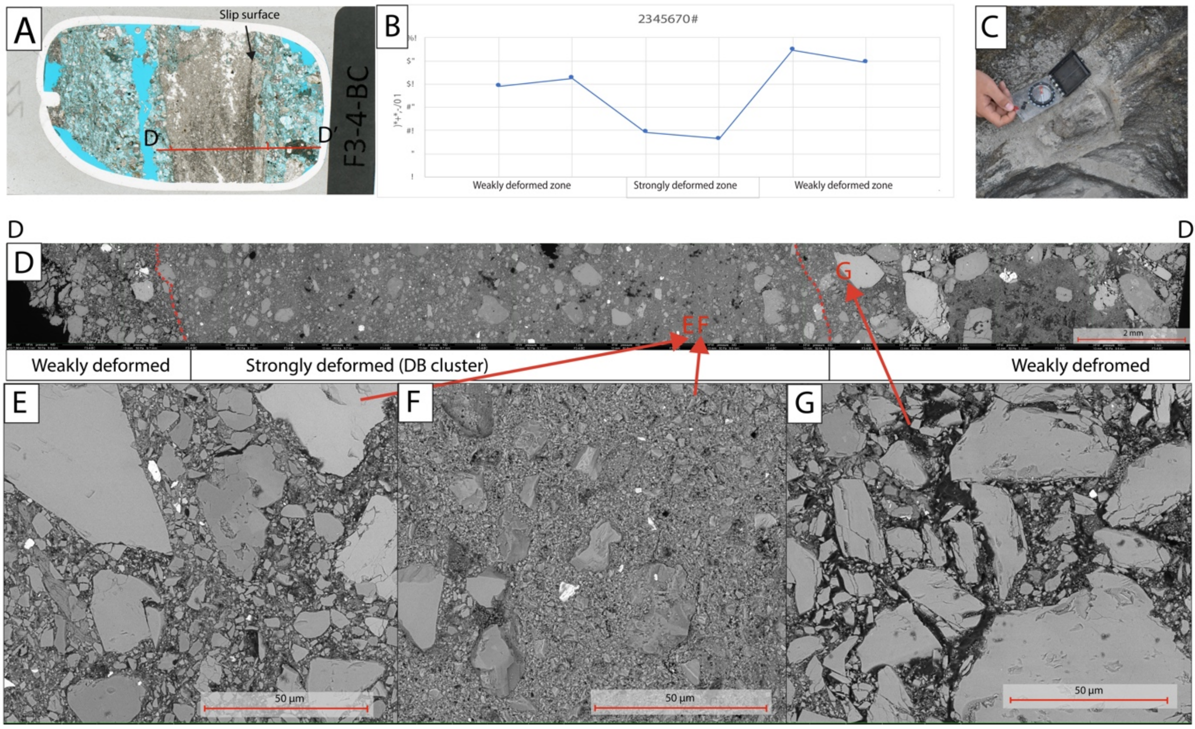

Figure 5.25: Summary of the observation done from sample 1 from locality 4. A) Thin section of sample 1. Red line marks the location of the photomosaic shown in Fig. D. B) Optical porosity measurements from BSE-SEM pictures over the photomosaic in Figure D. C) Field photo of the sampled DB cluster. D)A photomosaic of BSE-SEM pictures of the DB and the deformed host rock. Black colour represents pore space. E) A close-up photo of the matrix in the DB. Red arrow marks the location F) A close-up photo of the matrix close to the slip surface in the DB. Red arrow marks the location. G) A close-up photo of the matrix in right adjacent to the DB. Red arrow marks the location.

A DB network in the damage zone was sampled from locality 11 (Fig.5.24E). A photomosaic of SEM images taken across a single strand in the DB network, is shown in Figure 5.26B and displays a reduction in porosity from 27% to 8.7% (Fig. 5.26A). Especially the glass fragments of the matrix seem to be more crushed and packed together than the subhedral to euhedral crystals (Fig. 5.26D; E).

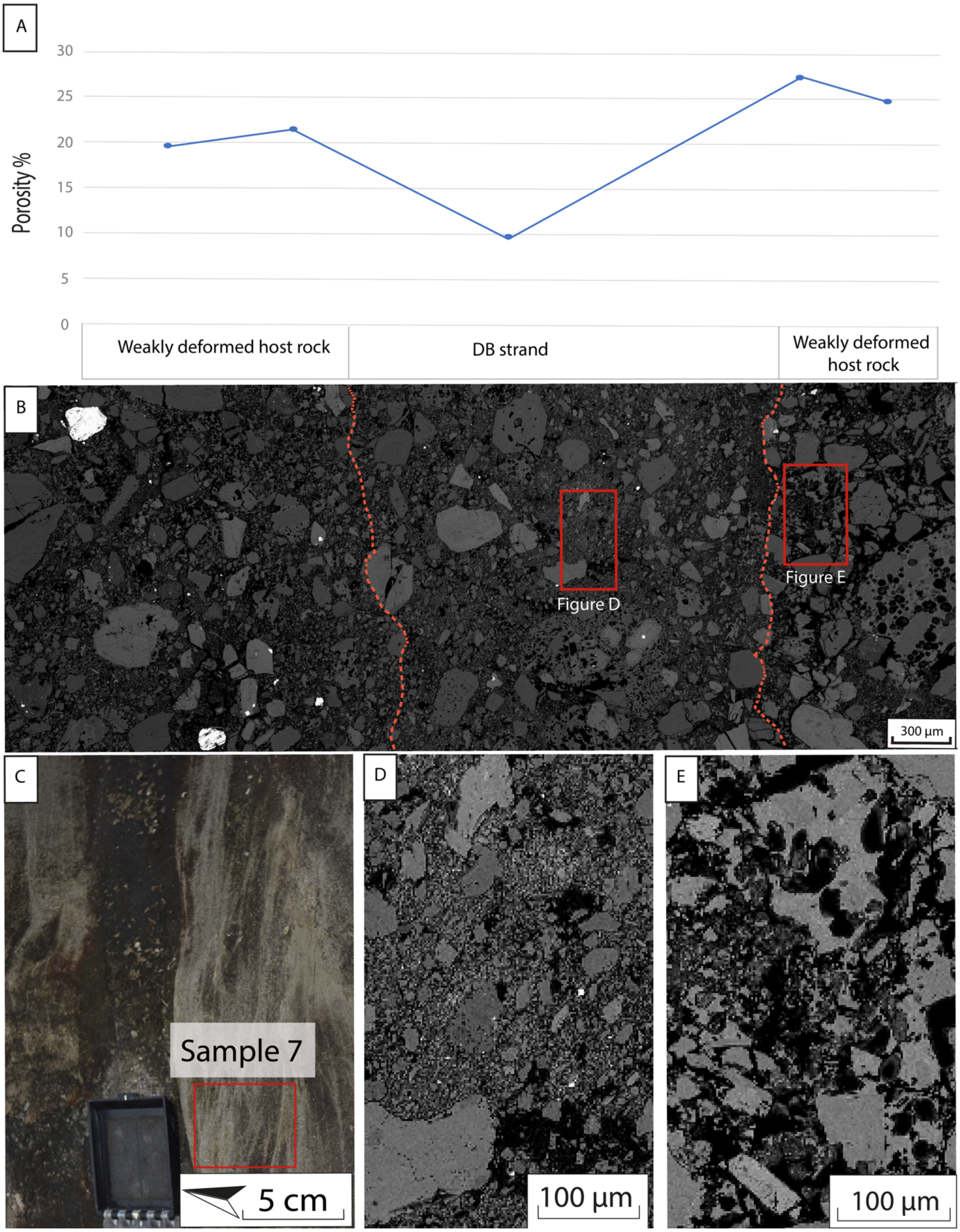

Figure 5.26: A) Optical porosity measurements from BSE-SEM images over the photomosaic in Fig. B. B) A Photomosaic of BSE-SEM images taken over a single DB strand. Black colour represents pore

space. C) Field photo from the sample location. D) A close-up of the matrix in DB strand. Location outlined in red in Fig B E) A close-up of the matrix outside the DB. Location marked in red in Fig B

Fault core dominated by discrete-slip

In contrast to the DB-dominated parts of the fault, a distinct fault core comprised of single or several slip surfaces characterise the fault further to the SW. In this area the fault dissects polygenic lapilli-tuff to breccia layers (Fig. 5.27). The shear offset is accommodated by one principal slip surface (Fig.5.27 A; B; C) or several slip surfaces (Fig. 5.26 D and E). The damage zone is expressed by extensional fractures and a few, thin DBs. The fault is prone to weathering in these parts and therefore few good exposures of the fault core exist along the strike of the fault. Consequently, some uncertainties are related the presence of fault rocks and true thickness of the fault core, which could be less than what has been measured in the field, at many localities. The width measurements range from 4 centimetres (one slip zone including fault rocks) to 90 centimetres (in a zone of 8 slip surfaces). Thin zone of cohesive cataclasites are present (Fig. 5.27 B) and are composed of crushed crystals (50-100um) within an ultrafine matrix (50-90%) (Fig 5.28 A and C, *sensu* Sibson, 1977). The second lowest displacement measured (89 centimetres) at segment 2 is measured in the polygenic unit (at locality 8, see Fig. 5.26 A;B;C) where the offset is accommodated by one discrete slip zone in the vicinity of a cm-scale cataclasite rock volume (Fig. 5.27B). Conversely, the highest offset measured (2.66 metres) is situated ten metres towards the NE (at locality 7) in a similar polygenic unit but then distributed over several slip surfaces (Fig. 5.26D). Heavily fractured lenses of the host rock are observed in-between the slip surfaces (Fig. 5.26D and E)

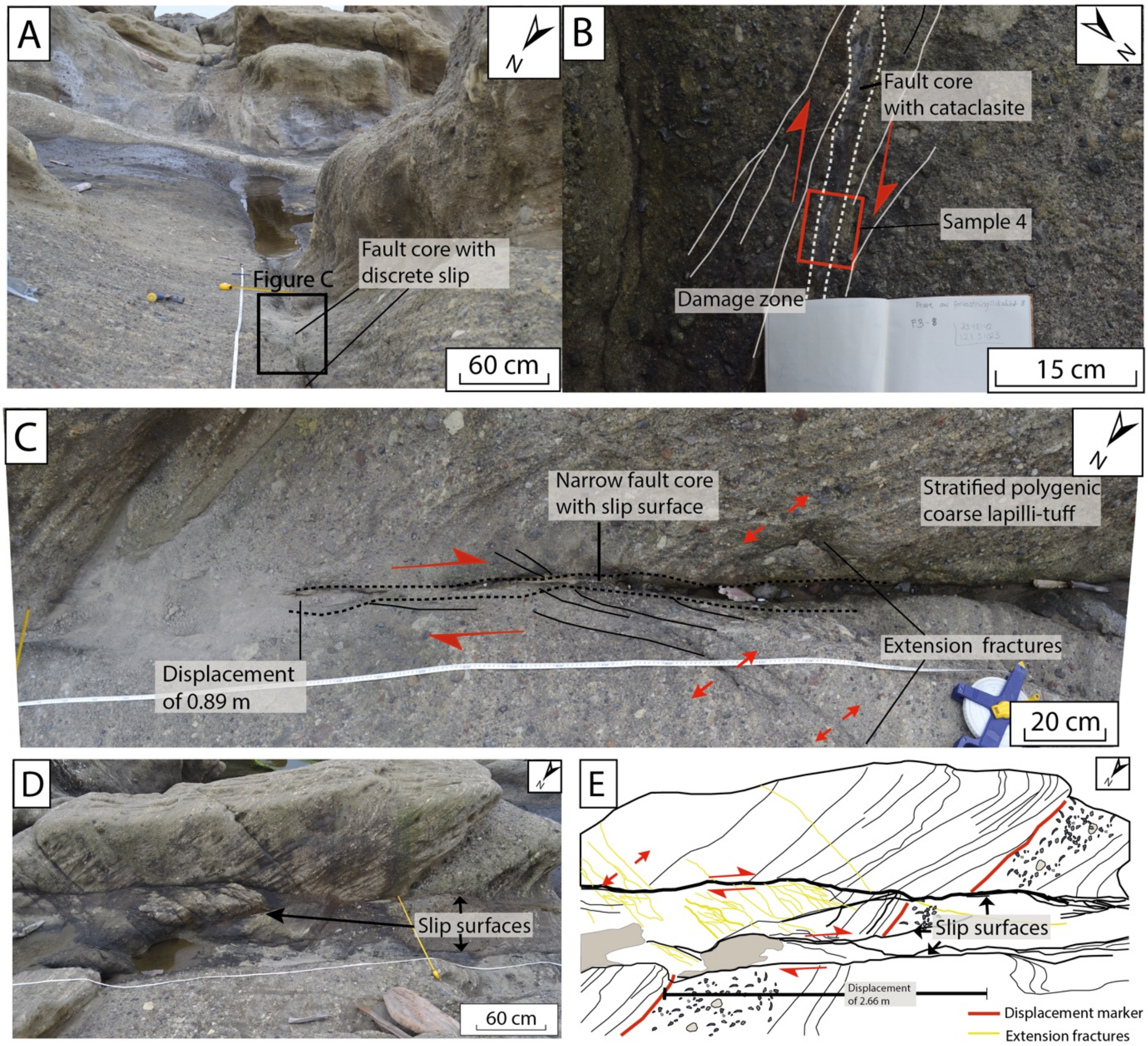

Figure 5.27: Outcrop pictures from brittle parts of the fault. A) Outcrop photo from locality 8 that show a narrow zone of deformation with only one main slip surface. The fault represents a local depression in the terrain. The location of figure C is marked with a black square. B) A close-up photo of the slip surface which consists of dark and microcrystalline material. Thin strands of DBs are developed in the immediate vicinity of the slip surface. Sample 4 is taken from this locality. C) A photomosaic taken along the narrow and brittle fault core which is weathered and covered in scree. The damage zone is mainly characterised by extension fractures. D) Field photo from locality 7 that display a fault zone with several slip surfaces and highly fractured rock lenses within the zone. E) A schematic interpretation from figure D. A layer of polygenic volcanic breccia works as displacement marker.

Some difficulties occurred when sampling the slip surfaces as they generally were weathered and partly incohesive. However, some samples of slip surfaces can be used for further microstructural investigation. Analysis done in both optical microscope and in SEM of thin sections from the fault core display large internal fault rock variations (Fig 5.28). An abrupt boundary between the compacted, fine-grained fault rock (cataclasite) and the deformed host rock are commonly observed. However, foliations are found in the fault rock (Fig. 5.28 A) and adjacent to the cataclasite (Fig. 5.28B). The grain size distribution is poorly sorted in the deformed host rock as the grain size ranges from 0.2 millimetres to 1 millimetres. Both intergranular fractures and local transgranular fractures are common in the deformed host rock. The deformed host rock may be characterised as a fine crush microbreccia (*sensu* Sibson, 1977). The fine crush microbreccia is highly porous (16-30%) (Fig. 5.28 D and E). In contrast, the cataclasite consists of a compact mass of very fine particles (Fig. 2.28F) with a few larger minerals (50 to 100 micron). Strike-parallel fractures are abundant in the thin sections, together with smaller perpendicular fractures (relative to the strike of the fault). The porosity measurements done in the cataclasite reveals a porosity of around 10 % and is mainly due to fracture porosity.

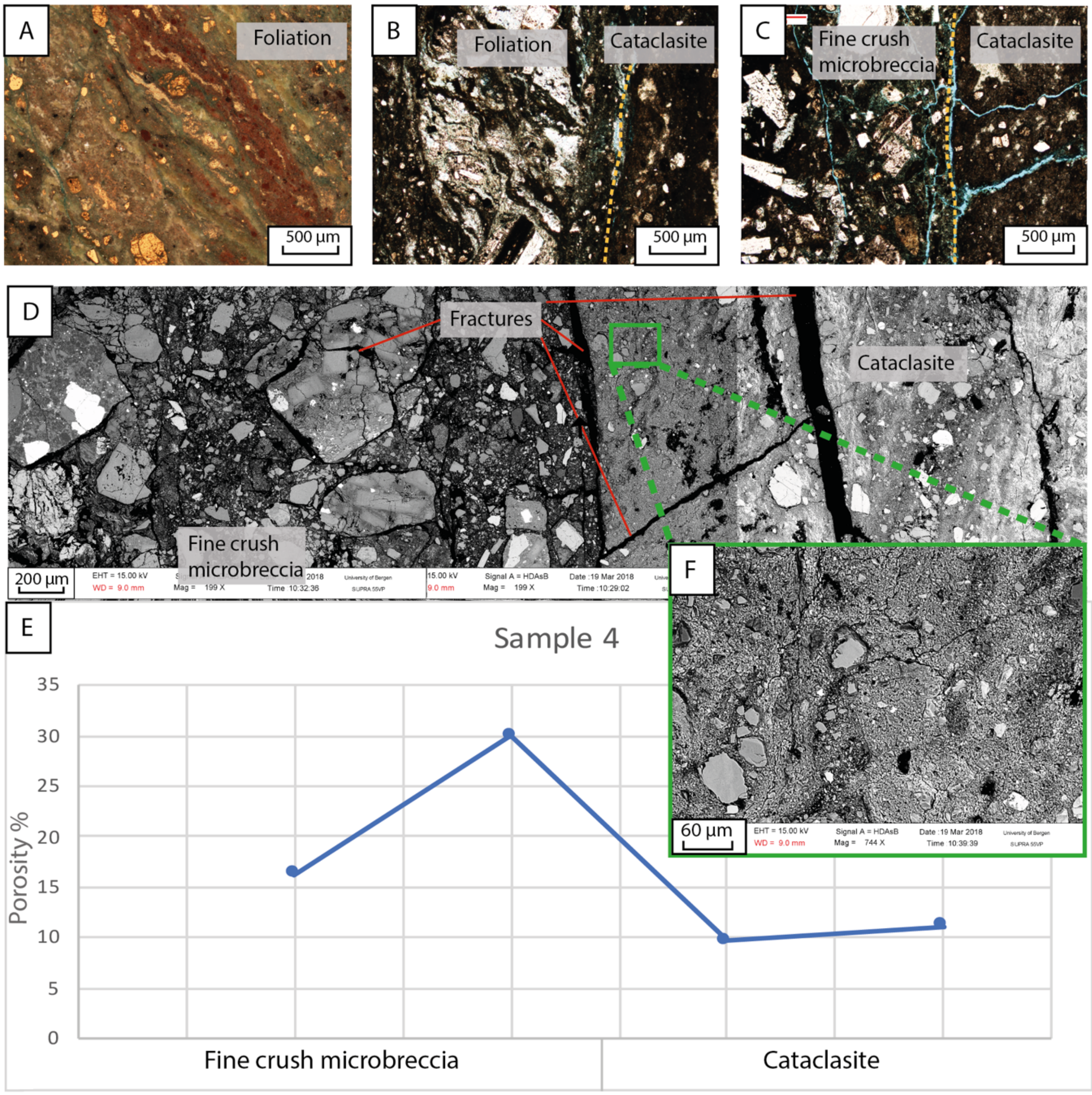

Figure 5.27: A) Microphotograph in PPL of foliations within a fault rock. B) A microphotograph in PPL of foliations adjacent to a cataclasite. C) An imagery done in optical microscope in PPL of a cataclasite and a fine crush microbreccia with an abrupt boundary and fractures. D) A photomosaic of BSE-SEM pictures of a fault plane and the deformed host rock B) Optical porosity measurements from BSE-SEM pictures over the photomosaic in Figure A. C) A close-up photo of the matrix in the fault plane. Black colour represents pore space.

Porosity estimations of the fault samples

The plots in Figure 5.29 show optical porosity estimations made on SEM images perpendicular to the DB or fault rock. The location of the samples is shown on the locality map in Figure 5.22. Sample 1, 2 and 7 are from the DB-dominated part of the fault with distributed shear and samples 3-5 are from the fault core with discrete slip. All the transections show a clear porosity declination from the deformed host rock to the DB/fault rock. The lowest porosity is detected in the DB cluster in sample 1 (1.68%) (Fig. 5.29a) and in the fault rock in sample 5 (4.02%) (Fig. 5.29e). Sample 4 (Fig. 5.29d) stands out as the measurements acquired from the fault rock boundary show a clear increase in porosity, which can be explained by a high density of fractures. Samples 4 and 5 are both from locality 8, but display different porosity values, as sample 5 has a generally lower and more uniform porosity profile. Plot G (Fig. 5.29g) shows the mean porosity (of the two to three porosity measurements) in the DB or fault rock for each sample along the fault, from SW to NE. The horisontal axis in plot G consists of the different sample numbers.

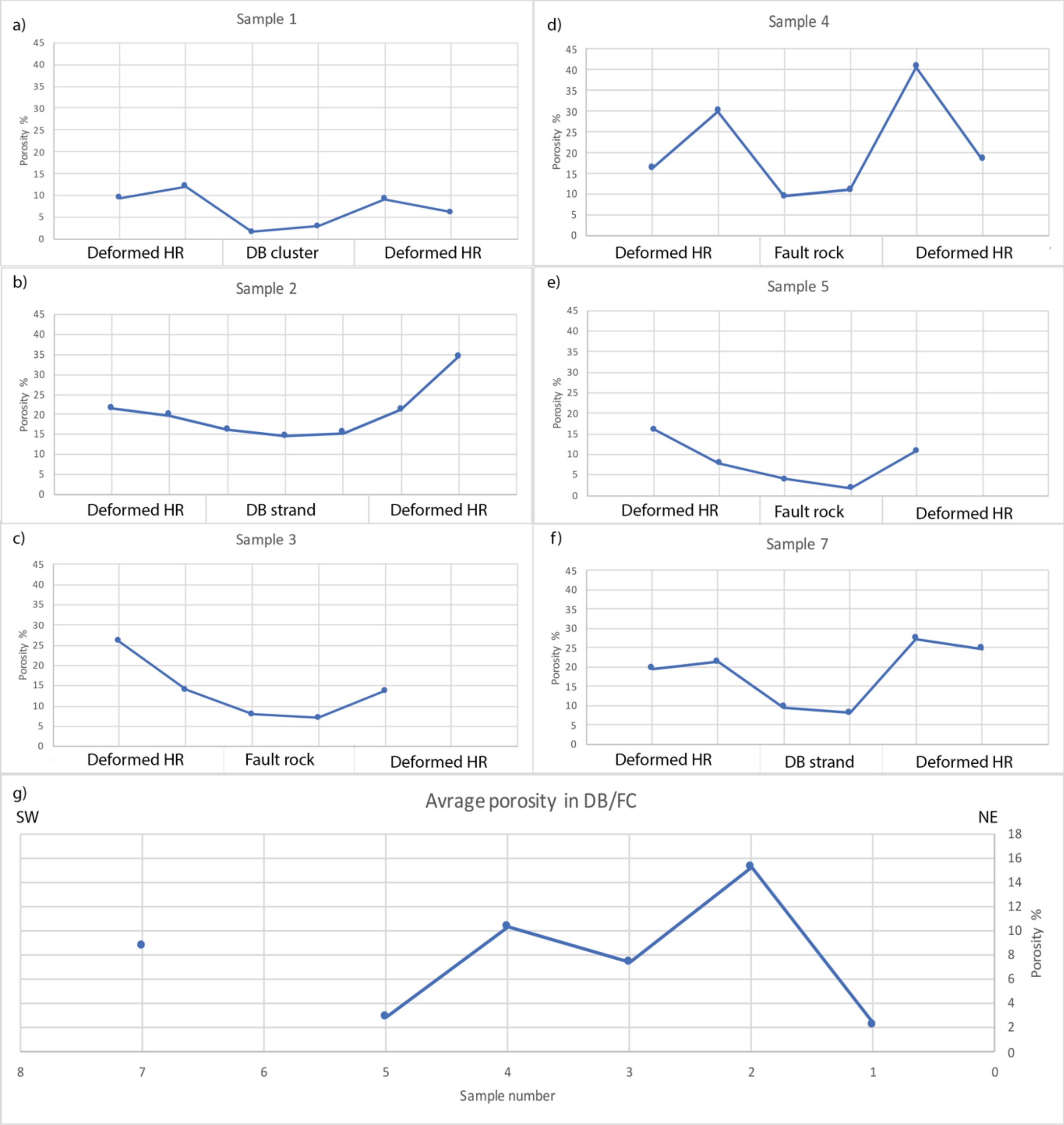

Figure 5.29: Tables over optical porosity measurements from each sample along the fault. Sample location is shown in Fig 5.21. Five to six areas of the samples were measured. Where possible, two measurements of the deformed host rock at each side of the DB or slip surface, and two porosity measurements were done on different areas within the DB or fault rock. The horizontal axis is comprised of HR=Host rock, DB strand/cluster or fault rocks. a) Porosity measurements from sample 1 taken at locality 4. DB cluster b) Porosity measurements from sample 2 from locality 5. DB network. c) Porosity measurements from sample 3 from locality 7. Fault core dominated by discrete slip. d) Porosity measurements from sample 4 from locality 8. Fault core dominated by discrete slip. e) Porosity measurements from sample 5 from locality 8. Fault core dominated by discrete slip. f) Porosity measurements from sample 7 from locality 11. DB network in the damage zone. g) Plot of the mean porosity in the DB or fault rock (of the two to three porosity measurements) for each sample along the fault, from SW to NE. The horizontal axis in plot g consists of the different sample numbers.

5.6 Scaling relations

To investigate the relationship between displacement, width of the DBs and faults, and the number of strands through the different stages of development (from incipient bands to faults), are three different log-log plots are presented in Figure 5.30 to 5.32. Incipient bands are marked by green dots, mature bands are pink, and faults are yellow. The plot displayed in Figure 5.30 shows the correlation between displacement and width at each stage of development. There is a positive relation between the width and displacement for the DBs and faults as they partly follow a power law. However, the scatter plot reveals large variations which causes the degree of fit (R^2) to be 0.6407.

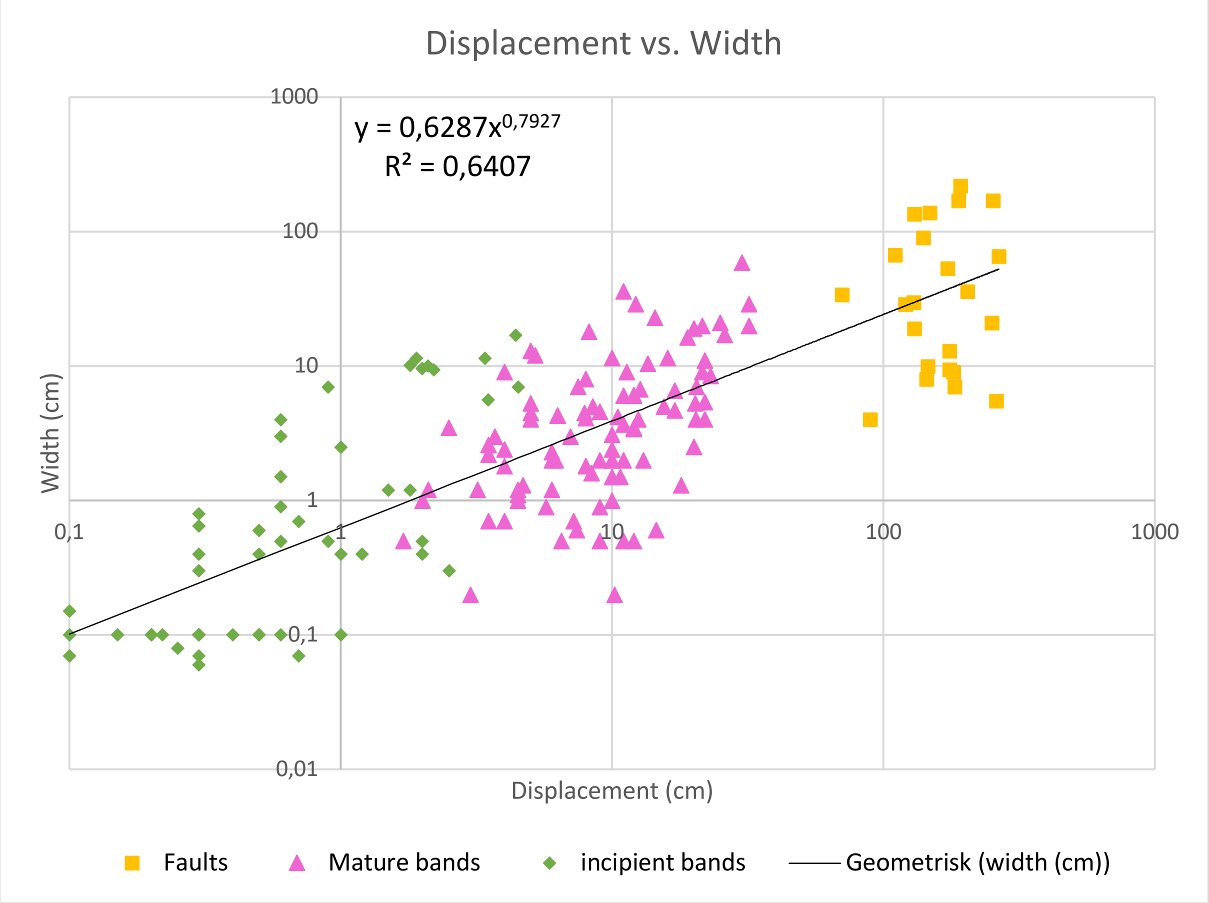

Figure 5.29: Log-log scatter plot showing the relationship between displacement and width of incipient bands (green dots), mature bands (pink dots) and faults (yellow dots).

Figure 5.31 displays the relationship between displacement and strands (including merged DB clusters and slip-surfaces). The plot follows a fairly strong power law for the DBs, while the faults display a larger scatter of points. When removing the fault data points which is not associated with any deformation bands and is comprised of only one slip surface the R^2 value increases (Fig. 5.32).

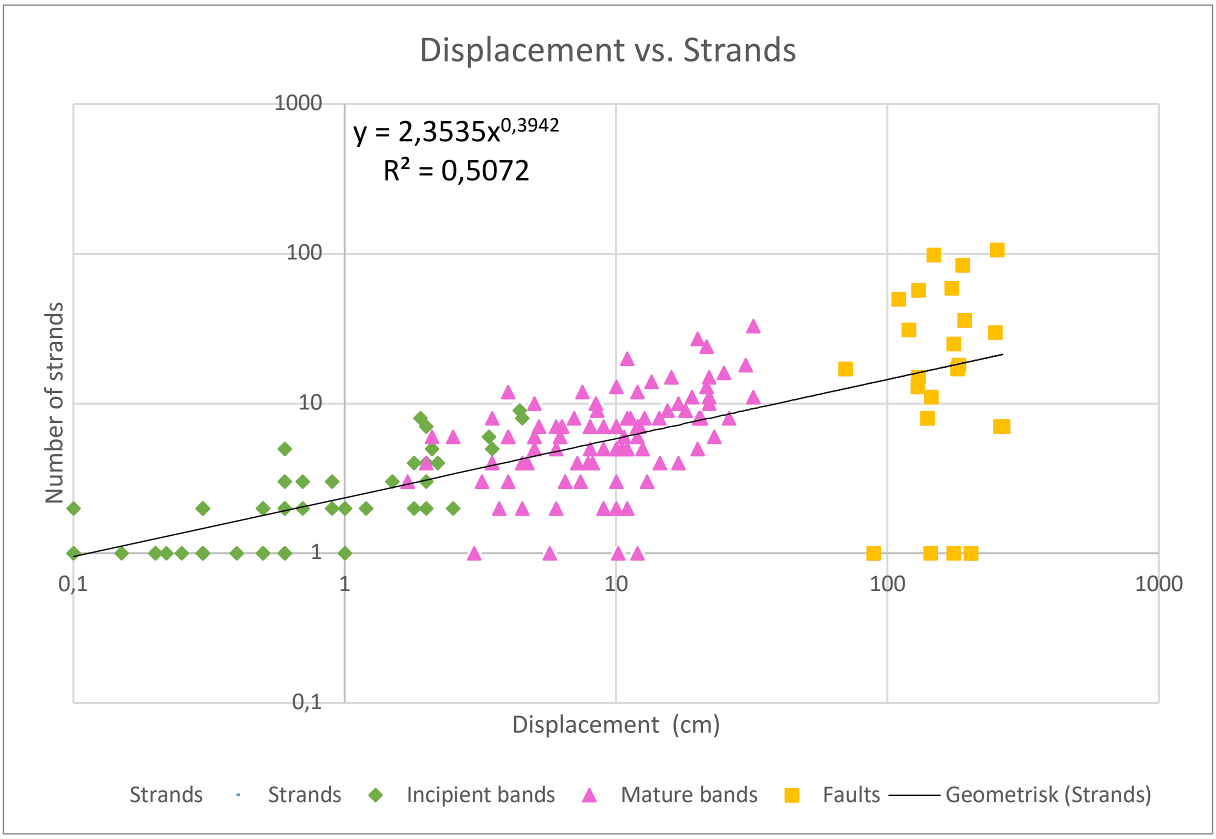

Figure 5.31: Log-log scatter plot showing the relationship between displacement and strands of incipient bands (green dots), mature bands (pink dots) and faults (yellow dots).

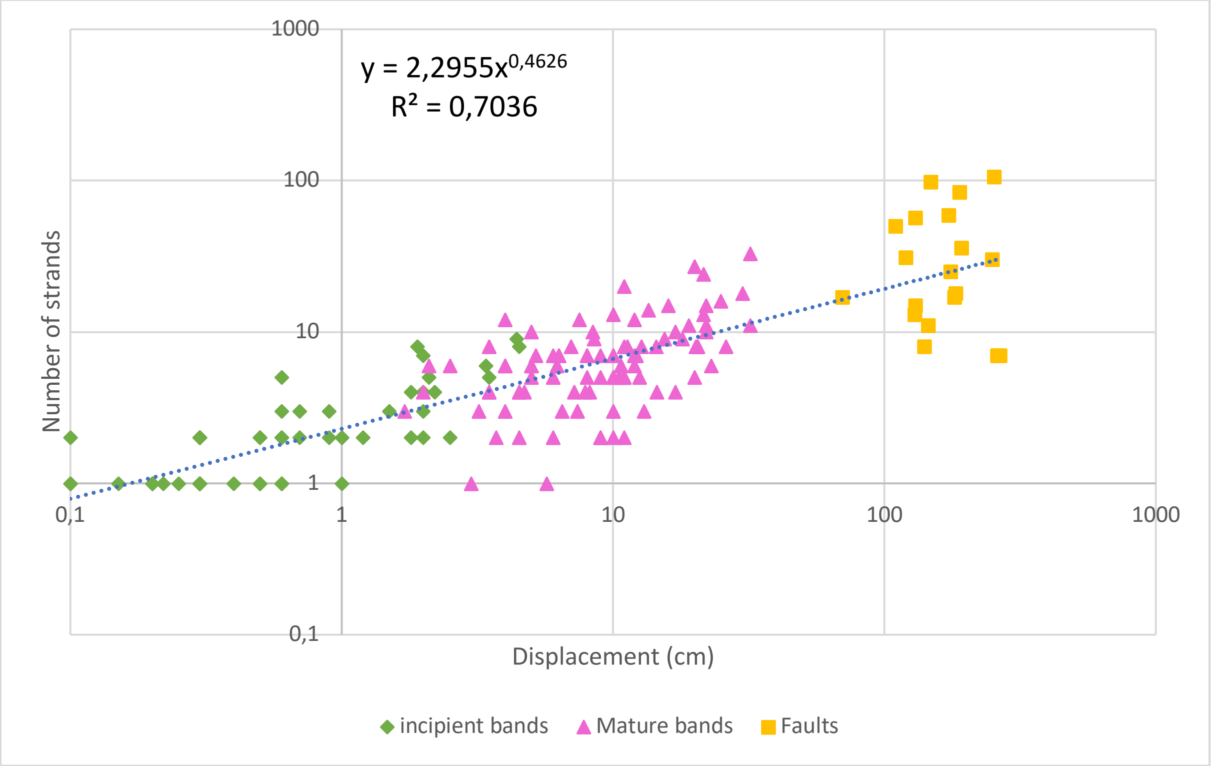

Figure 5.32: Log-log scatter plot showing the relationship between displacement and strands of incipient bands (green dots), mature bands (pink dots) and faults (yellow dots), single stranded faults is in the presented plot removed.

6. DISCUSSION

The aim for this study has been to gain insight into fault formation in volcaniclastic rocks, by elucidating the evolution from incipient deformation bands to fully developed faults. Additionally, an aim has been to acquire a better understanding of controlling factors of the variable architecture of deformation bands and faults. In this chapter, the data presented in the foregoing chapters will be interpreted, discussed and compared with existing work on fault development in other lithologies as well as volcanics/volcaniclastics.

6.1 From incipient band to fully developed fault: evolution of deformation bands dominated faults in volcaniclastic rocks

The sequential development of single deformation bands into zones of deformation bands and, finally, into faults was pointed out by Aydin and Johnson (1978). Deformation bands that accommodate small offset are widely known to exhibit the potential to be precursors and characterise the early stages of fault development and slip accumulation (e.g. Aydin and Johnson 1978; 1983; Antonellini and Aydin, 1994, Shipton and Cowie 2001; Rotevatn et al., 2008; Tondi et al. 2012). Using displacement as a proxy for the stage of development, a three-stage model is here presented for the evolution of deformation band-dominated faults in porous volcaniclastic rocks: i) Formation of individual bands with limited compaction and shar accommodated through granular flow and cataclastic flow mechanisms, ii) displacement accrual and, to some extent clustering, and nucleation of patchy slip surfaces. Accommodated though a combo of cataclastic flow and discrete brittle failure/slip, and iii) formation of a through-going slip surface and accumulation of significant (>0.5 m) shear displacement, accommodated predominantly by brittle discrete failure/slip, with cataclastic flow taking the back seat at this stage.

Stage 1-Initial stage

The initial stages of fault development in volcaniclastics can be exemplified through the studied incipient bands. The fault initiation is marked by small deformation bands with mm-cm-offset and comprised by one or a few thin deformation band strands (generally 1 to 3). Frequent segmentation and short length characterise the incipient bands and the first stage in the fault evolution. The displacement profiles in Figure 5.13 and 5.14 and appendix I are similar to what have previously reported by Fossen and Hesthammer (1997), in which the displacement maxima are located near the central parts of the structure and often connected to relay zones. Asymmetry in some of the profiles is either connected to relays or could be related to lithological differences and non-planar surfaces (Fossen and Hesthammer, 1997). When considering the relationship between length and maximum displacement, the incipient bands seem to follow a power-law relationship (Fig 6.1), which could be consistent with growth whereby a band accumulates displacement and length synchronously. However, the deformation bands are underdisplaced compared to similar-length faults (e.g. Hesthammer and Fossen, 1997; Tondi et al 2012). Linkage and interaction of deformation bands could cause rapid length growth and thereby explain this relationship. Accordingly, linkage and interaction are important processes at this initial stage. Observation from the field (Fig. 5.13 and 5.14) suggests that splaying fractures at the band tips, linking bands and more complex structures are formed related to linking of two bands. Stress perturbation and stress rotation may be caused by interacting stress field of two approaching bands (e.g. Schultz and Balasko, 2003: Okubo and Schultz, 2006), which in turn may trigger band linkage and the ensuing breaching of soft-linked relay structures.

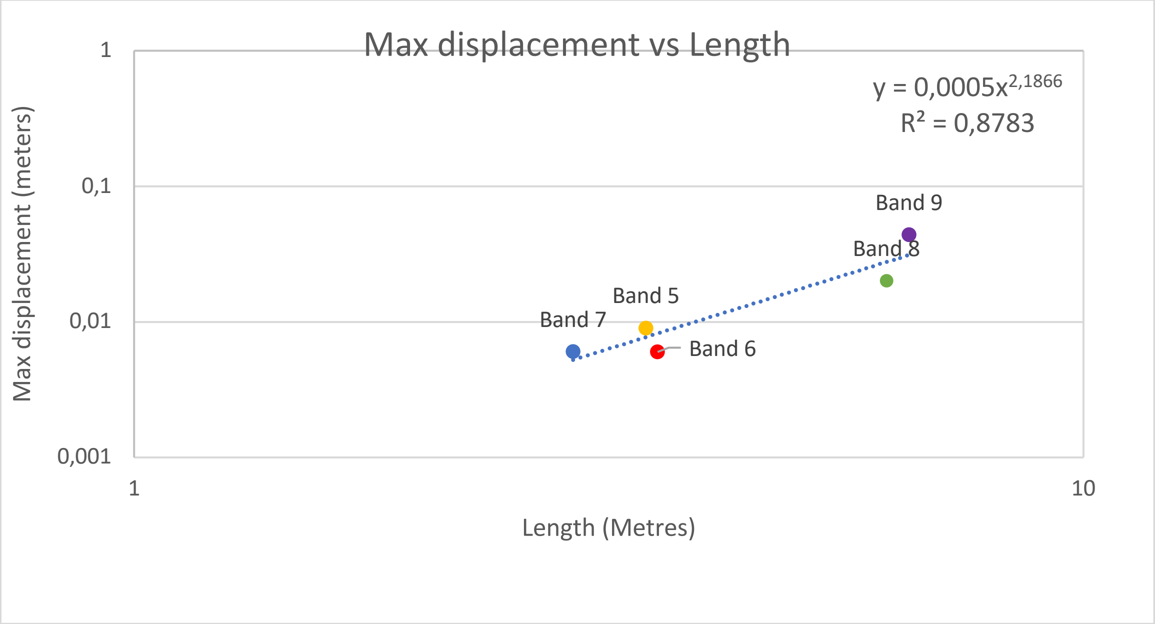

Figure 6.1: Log-log scatter plot showing the relationship between maximum displacement and length of the studied incipient bands

Microstructurally, this initial stage is characterised by shear, compaction, grain fragmentation and reorientation, and comminution (Fig 5.15). Comminution of both glass fragments and crystals leads to a thin (c. 1 mm) compacted and sheared zone with an up to five-fold reduction in porosity compared to the host rock. This indicates that cataclasis is the dominating deformation mechanism, and that it occurs at an early stage in the evolution of deformation bands and faults. Microstructural investigations show that volcanic glass is prone to comminution. Compared to the mineral grains, the glass shards are comminuted to the same extent, or more (Fig. 5.15 C), and comminution may be initiated before fracturing and comminution of mineral grains. This coincides with the findings of Wilson et al. (2006), who suggests that glass shards are mechanical weak and are preferentially crushed. Therefore, the nucleation of the deformation band may initiate by deformation of the glass shards as they represent the weakest part of the host rock.

Stage 2- Intermediate stage

Successively, the deformation bands evolve into the intermediate fault stage as the shearing continues, in which they form clusters and networks of conjugate cross-cutting deformation bands. This stage is expressed in the field by the mature bands (Chapter 5.4), which accommodate cm-dm-scale offsets. The total length of the bands at this stage is not documented, but outcropping lengths of 67 metres have been observed. Patchy slip-surfaces develop locally in the middle or at the margins of deformation band clusters or networks. Single cm-scale slip surfaces propagate in in association with deformation band clusters, while several mm-scale slip surfaces develop in deformation band networks adjacent to one another. The observed minor slip surfaces in networks of strands also indicate that the nucleation of slip surfaces develop at an early stage, and that a deformation band-cluster is not essential for its formation. Bifurcation and coalescence of the deformation band strands are common at this stage, which results in highly variable thickness of the deformation bands and number of strands. However, segmentation of the deformation band-zone is less frequent compared to the initial stage and the relay zones are characterised by a dm-wide zone of stepping deformation bands.

Width, strands and displacement profiles collected along the outcropping mature bands display variations tied to lithology, low-porosity bombs and relay zones. Irregularities as low-porosity bombs and linking relays cause a change in the architecture of the deformation bands as the band becomes wider and consists of more strands. Higher shear strain is also at this stage connected to relay zones. The relationship between displacement, width and strands is illustrated by the plots in Figures 5.29 to 5.32. These show a positive correlation between displacement, the number of strands, and width, and that accumulation of displacement usually requires a wider zone of several deformation bands. Consequently, increasing shear is accommodated by an expansion in the width of the band and an increased number of strands (e.g. Mair et al. 2000). However, lithological differences also play a major role of the band architecture at this stage (Figs. 5.16 and 5.18). Deformation bands in tuff and ignimbritic units are generally constituted by a wide zone consisting of several strands. While polygenic units are generally associated with thin deformation band clusters and extension fractures.

The intermediate stage can be observed at microscale as enhanced grain comminution and compaction. The cataclasis is affecting a larger radius, compared to the initial stage, resulting in a cm-wide strain-hardened (e.g. Aydin and Johnson, 1983) network of cataclastic bands or a mm-wide deformation band cluster. Progressive shear causes the formation of slip surfaces at the boundaries, and/or in the centre of the deformation band. As a result, a local shift from strain hardening to strain softening behaviour occur as the displacement is accommodated by frictional slip at the patchy slip surfaces. Thus, cataclasis is the most dominant deformation mechanism at the intermediate stage, followed by local initial brittle failure. S-C fabric between strands in deformation band networks may develop at this stage and is documented by (Kjenes 2018). Porosity reduction at the intermediate fault stage is severely reduced (Kjenes, 2018). However, networks of deformation bands cause negative relief locally in the host rock, which may indicate a local reduction of weathering resistance and increased porosity.

Stage 3-Final stage

By this stage, the patchy slip surfaces will commonly have propagated and linked to form one or several continuous, through-going slip surfaces, at which point we define the structure as a fully developed fault. The faults accumulates displacement of more than 0.5 metres. This final stage is comparable to the final stage of fault evolution presented by Cowie and Shipton (2001), where slip surfaces accommodate the majority of the fault displacement. However, some displacement will be accommodated by broader zones (compared to the earlier stages) of deformation band networks/clusters which envelope the slip-surfaces. The formation of a through-going slip surface coincides generally with a final stage of the fault zone establishment. Nevertheless, a through-going slip-surface is not always present, as seen in the presented data in Chapter 5.5 (Fig 5.24C), where a broad zone of deformation bands accommodates nearly one metre of offset without a visible continuous slip surface. At the final stage a distinctive fault core will be present more or less with an enveloping damage zone. The damage zone consists of scattered deformation oriented parallel to the strike or as antithetic structures. As will be further discussed in Chapter 6.3, the architecture of the studied fault zones exhibits large variations probably due to lithological variations.

Microstructurally, in the final stage progressive shear leads to a shift in the dominating deformation mechanism, which change from intense cataclasis to discrete brittle failure (e.g. Wong et al. 1997). Broad cm-wide clusters with slip surfaces (Fig. 5.25) and low porosity are distinguishing characteristics for this stage. Severe grain comminution, compaction and frictional slip generate very low porosity within the deformation band clusters. In comparison, deformation band networks comprised of single strands exhibit higher porosity between 8 to 15%.

Figure 6.2 summarises the proposed fault evolution model and illustrate, at macro- and microscale, how progressive shear results in a through-going fault. Faults in this study start forming as small incipient deformation bands (Fig. 6.2, stage-1) once horizontal stress is induced. Continued shear leads to linkage and interaction of the incipient bands to form longer, thicker and multi-stranded deformation bands (Fig. 6.2, stage-2). Increased shear leads eventually to propagation and linkage of the slip surfaces. Ultimately the slip surfaces will link up to a through-going fault plane where most of the displacement is accommodated (Fig. 6.2, stage-3).

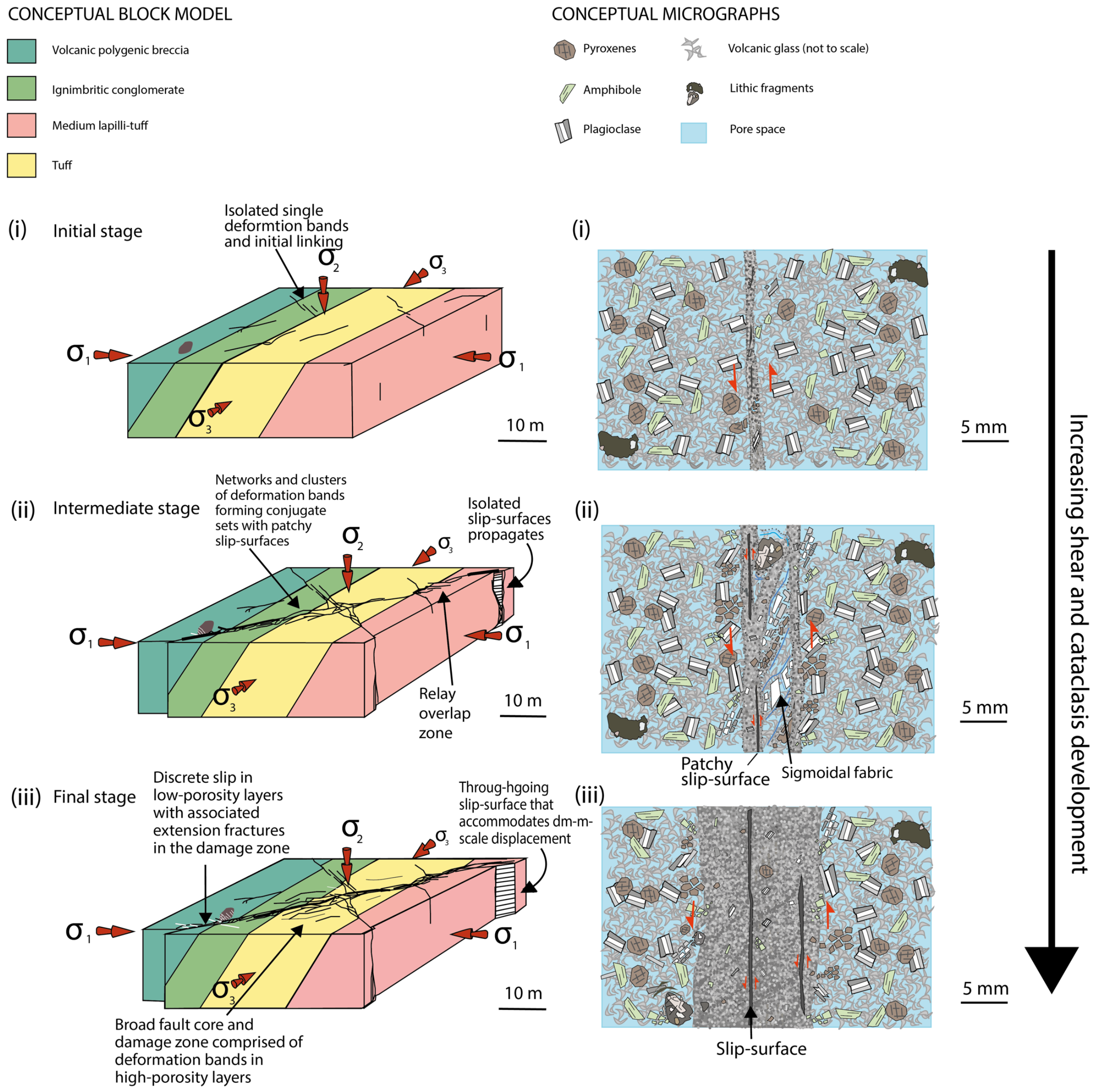

Figure 6.2: Schematic block models and micrographs over the proposed evolutionary stages of a fault in porous volcaniclastics; i) Initial stage ii) Intermediate stage. iii) Final stage. See text for details.

Discussion of the presented fault model and how it relates to previous studies.

Having presented the above model for fault evolution in porous volcaniclastics, the following section will substantiate and discuss the sequential model, and how it relates with previous studies in other lithologies.

Support for the presented sequential fault model may be found in the scaling relations between displacement-width and displacement-strands (shown in the plots in Figures 5.29 to 5.32). These attributes follow a power law which suggests that displacement is a controlling factor of the thickness of the deformation band/fault and number of strands. Additionally, this positive trend could support the evolution model, as more complex deformation band structures requires higher displacement. Nevertheless, the correlation is not perfect. The scatter of points may be caused by lithology and/or linkage of deformation bands, in addition to bifurcation and amalgamations of deformation bands. The plot in Figure 5.32, in which single stranded faults are removed from the plot, has an improved regression of fit (R^2). The removal of these points is done because the fault in some lithologies are characterised by discrete slip surfaces, and not distributed deformation banding. The removed points will therefore represent areas where the fault have a different formation mechanism.

Fault evolution in porous sandstone have been discussed for decades (e.g. Aydin and Johnson, 1978; 1983; Cowie and Shipton 2001; Schultz and Siddharthan, 2005; Fossen and Rotevatn 2012). In contrast, fault zone evolution in porous and granular carbonates has recently become a field of active research (e.g. Tondi; 2006; Micarelli and Wibberley, 2006; Tondi et al 2012; Bastesen and Braathen, 2010; Rotevatn and Bastesen, 2014). Also, fault zones in volcanic rocks have been a matter of discussion the last decade (e.g. Gray et al. 2005; McGinnes et al., 2009; Riley et al., 2010; Walker et al., 2013; Soden and Shiption, 2013). The proposed model for faulting in volcaniclastics in this thesis shares similarities with the models that are suggested for fault evolution in porous sandstones (e.g Aydin and Johnson 1978; 1983; Cowie and Shipton; Rotevatn and Fossen, 2012): First, the faults are a result of cataclastic deformation which initiated as single cataclastic deformation bands. Furthermore, the sequential evolution from single bands to zones of bands, and finally to faults is parallel to what previous studies have suggested (Aydin and Johnson,1983; Shipton and Cowie, 2001). Finally, the last fault stage whereby growth and linkage of patchy slip surfaces form a through-going fault plane are equivalent to what aforementioned studies have found.

Regarding differences, the suggested fault model in this thesis deviates from other models as the deformation bands exhibit larger displacement and slip surface nucleation occurs at an early stage (intermediate stage) in single strands. Contrary to what has generally been reported in sandstones, thick zones of deformation bands are not required for slip surface development. Deformation bands in sandstones are recognized to be strain hardening features (e.g. Aydin and Johannesen 1978;1983; Mair et al. 2000, Fossen et al 20 07) where slip surfaces develop after intense clustering and strain hardening within the zone. The Shithiping deformation bands form slip surfaces at an early stage, not necessarily connected to thick clusters, and several small slip surfaces can nucleate adjacent to one another. Moreover, the deformation bands can accommodate larger displacement than normally reported for deformation bands in other lithologies (e.g Fossen et al. 2007). Early slip-initiation and large displacement may indicate that strain hardening mechanism are less evident in the Shihtiping deformation bands and that strain softening happens earlier than in porous sandstones. In that case the mineral grains will fracture at an early stage (local strain softening) and promote cataclasis. The weak glass in the matrix could explain the premature cataclasis and may lower the mechanical and yield strength of the host rock. As a result, the band will reach the yield frictional strength of the rock and rupture earlier than what is generally observed in porous sandstones. A slip surface has a low frictional strength and less stress is required to keep the deformation along a slip surface going compared deformation banding where interlocking of grains cause strain hardening (e.g. Aydin and Johnson, 1983)

Rotevatn et al. (2008) documented slipped deformation bands that were not associated with clusters in high-porosity fluvial sandstones in the Suez rift. This study suggested that large grain sizes, high porosity and pre-fractured host rock could explain strain softening during the evolution of a band and early slip surface development. Nicchio et al. (2017) reported on deformation bands with localized slip zones in feldspar-rich porous conglomerates and argued for early slip surface development due to high feldspar content. Moreover, findings of Mair et al. (2002) shows that angular shaped minerals promote cataclasis. It can be argued that these ideas can be transferred to the deformation bands of Shihtiping, as the host rock has similar attributes:

(i) High porosities (Fig 5.7) which may lower the critical pressure for failure in the rock by decreasing the yield strength (Schultz and Siddharthan, 2005; Rotevatn et al. 2008)

(ii) High background fracturing in the host rock (Fig. 5.6G), however, this may be due to uplift and could have occurred at a later stage.

(iii) A high content of weak angular glass, plagioclase and other angular grains with cleavage.

Consequently, all these characteristics promote cataclasis from an early stage of fault evolution. For instance, the mineral assembly of plagioclase, pyroxenes and amphiboles have angular shapes, and all have two prominent cleavage planes, which represent weakness zones (Tullis and Yund, 1987). Mineral cleavage may cause anisotropic mechanical strength of the minerals, in contrast to quartz grains in porous sandstones which are more isotropic. The glass volcanic glass and the mineral content of the host rock could contribute to enhanced susceptibility for cataclasis and reduce the yield strength of the host rock. Consequently, the non-welded volcaniclastic host rock is weaker than a general porous sandstone and deform by extensive cataclasis and brittle failure at an earlier stage than observed in porous sandstones and carbonates. However, laboratory triaxial experiments of the host rock, in addition to more studies of microstructural deformation should be carried out to verify this assumption.

The proposed model is also comparable to studies conducted by Tondi et al. (2012) in carbonates on Sicily, where single bands evolve into zones of bands and eventually develops through-going slip surfaces. However, the model deviates from the findings of Tondi et al. (2012) as the single bands with mm-displacement observed in Shihtiping are longer than the mm-displacement bands Tondi et al. (2012) reports from the carbonates in Italy, which are 30-100 centimetres long. This suggests that the Shihtiping bands propagate in length more easily than the deformation bands on Sicily. Moreover, the formation of through-going slip surfaces and the stage of faulting starts after the band has accommodated 10 centimetres of displacement. The fault stage is reached earlier compared to studied deformation bands in this study, where the faulting stage starts after approximately 50 centimetres displacement. However, nucleation of patchy slip surfaces starts probably at smaller displacements in Shihtiping than in the deformation bands on Sicily. Faulting, deformation banding and slip initiation in carbonates are commonly associated with pressure solution and cataclastic pore collapse (Tondi et al. 2006; Zhu et al. 2010). Intergranular pressure solution is not observed in this study. Cataclastic pore collapse is observed in a minority of the lithic grains in polygenic lithological units but are not prominent deformation mechanism for the formation of deformation bands and faults in porous volcaniclastic rocks.

When comparing the suggested fault model with earlier fault studies in volcanic rocks, many of the previous studies are conducted in non-porous, non-granular volcanic rocks (often welded ignimbrites and tuffs, or interlayered volcaniclastics with basalt), which yield different deformation mechanisms than what is observed in this study (Gray et al., 2005; Soden and Shipton 2013; Walker et al., 2013). Accordingly, they do not form a basis for comparison. However, a fault study done in a rhyolitic tuff unit by Okabu et al. (2012) suggest that the evolution from deformation banding to a through-going fault is the result of alteration of the host rock. Alteration caused by fluid flow cause the host rock porosity to decrease. As a consequence, deformation banding cease and is replaced by brittle failure (fractures and eventually slip surfaces). This non-sequential evolution deviates from the proposed model in this study. Studies done on deformation bands, fractures and faults in the non-welded to welded tuff in the Volcanic tableland in California show some similarities with the studied deformation bands and faults (Wilson et al 2003; Evans and Bradbury, 2004; McGinnis et al, 2009). Firstly, the host rock in many of the units are highly porous, non-welded and contain pumice clasts and ash fall deposits. At microscale lithic fragments, phenocrysts of plagioclase, in addition to quartz, are surrounded by glassy matrix (Evans and Bradbury, 2004). The studies present welding as the primary control on the style of deformation and that deformation bands are found in non-welded units, whereas fractures and faults form primely in welded units. As aforementioned, Wilson et al. (2006) suggest that the deformation band initiate in the weak glassy matrix, which corresponds to the findings of this study. However, Wilson et al. (2003) found that the amount of ash, pumice, phenocrysts and lithic clast do not affect the mode of failure, which is opposite to what are being suggested here (further discussed in Section 6.3). In general, most studies do not go into the discussion of how the structures evolve into faults, which make the studies less suitable for comparison.

6.2 How do the slip surfaces nucleate and grow?

The proposed model includes slip initiation at an early stage of the fault evolution, namely stage 2 in the above proposed fault evolution. This section proposes a model for slip surface nucleation based on observations in SEM from the incipient bands. Microstructural observations within this study suggests that a possible precursor for slip surface (Figure 5.15D) will start with fracturing and reorientation of phenocrysts parallel with $\sigma3$ (Figure 5.15A). Figure 5.15B displays sigmoidal shapes of fractured mineral grains surrounded by pore space inside the cataclastic deformation band. The following sequential model for slip surface initiation is proposed (Fig. 6.3): The crystals rotate (30-40°) and align the most prominent cleavage plane with minimum principal stress axis ($\sigma 3$) inside the band (Fig. 6.3, step-1). A phase of shear-induced dilation at initial stress stages is reported from laboratory deformed rock samples (e.g Besuelle, 2001; Cilona et.al., 2012). Local, transient dilation at early stages of band development could also apply for the studied deformation bands. Transient dilatancy of the minerals could lead to extension fractures and an open void inside the band (Fig. 6.3, step-2). Cleavage fracturing (*sensu* Kjenes, 2018) of the mineral continues by extensional fractures perpendicular to the cleavage and shear fractures parallel to the cleavage (Fig. 6.3, step-2-3). As the band accumulates shear, the mineral becomes increasingly fractured. This area of fractured minerals and increased pore space inside the band works as a weakness zone where further localized shear can be accommodated. Continuous localized shear promotes intense grain comminution and compaction (Fig. 6.3, step-4). An incipient slip surface may form in the middle of the weakness zone, where further displacement can be accumulated (Fig. 6.3, step-5). Weak glass shards (Wilson et al. 2006) could feature an important function in the formation of slip surfaces as it is easily comminuted (Wilson et al.2006) and could have a lubricating effect on grain contact, similar to what presence of weak phyllosilicates do in other deformation bands (e.g. Fossen et al 2018). However, only one thin section from an incipient band is obtained. Several thin sections from different incipient bands are needed to conclude if this model is feasible.

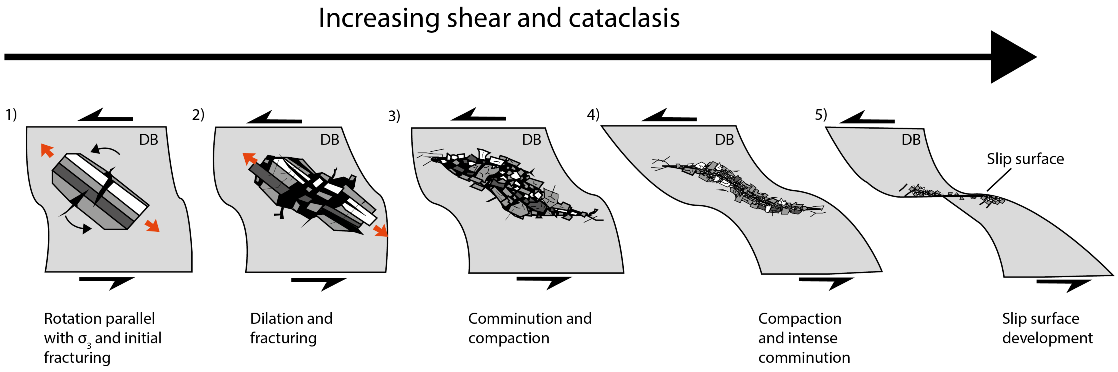

Figure 6.3: Proposed schematic and conceptual model of slip initiation within a deformation band focusing on the role of phenocrysts. Glass is not accounted for by this model. See text for further explanations. The numbers represent successive steps in the formation of a slip surface.

6.3 Fault architecture and controls thereof in volcaniclastic rocks

The results from this study show a highly variable fault architecture along strike in terms of thickness, displacement, number of strands and appearance. The faults are situated in a layered succession and display distinctive characteristics in terms of lithology and structural position. Hence, it is reasonable to discuss the lithological control on fault architecture and the influence of structural positions along the fault. The contrasting architecture and appearance of the fault are especially evident on Figures 5.24 and 5.27, which respectively display a part of the fault with distributed shear and deformation banding (in tuff and ignimbritic units), and discrete slip (in polygenic lapilli-tuff to breccia units). The variance of faulting across different lithologies may reflect the different mechanical properties of the host rocks, which in turn determine strain hardening and softening processes in fault zones (Heynekamp et al. 1999; Berg and Skar, 2005; Ferrill et al. 2017). The importance of lithological control on fault architecture and geometry in volcanic successions is highlighted by several authors that stresses the influence of the contrasting physical properties between well-lithified and poorly consolidated units (Riley et al. (2010); Walker et al., 2013; Soden and Shipton 2013). As already mentioned, earlier studies have documented that the degree of welding influences the style of deformation in ignimbrites (Wilson et al., 2003; Evans and Bradbury, 2004; Riley et al., 2010), where poorly welded units fail with deformation banding and welded units form fractures and slip surfaces. Evidence of welding is not documented in the studied succession, which raises the question of what may control the variable style in faulting.

The studied succession consists of non-welded ignimbrites, tuffs and pyroclastic material. Clear evidence from the results suggests that the polygenic units, which are comprised of low-porosity bombs, contain more fractures and discrete slip surfaces compared to tuffaceous and ignimbritic units. Fracturing of low-porosity lapilli clasts related to deformation banding in the polygenic breccia units occurs already at the initial stage of fault formation (Fig. 5.12). It is widely known that porosity regulates the deformation mechanism in granular material (e.g Aydin et al. 2006; Ballas et al 2015), as pore space allows the grains to translate, rotate and eventually interlock and fracture, and by this process shear is distributed. Whereas low-porosity rocks deform mainly by brittle failure. Considering the porosity estimations conducted in this study (Fig. 5.7), the polygenic volcanic breccia exhibit far lower porosity (as low as 3 %) compared to the other units, which in turn favors brittle fracturing. Moreover, glass content in the host rock could influence the prevailing deformation mechanism. Welded and porous (13-

20%) tuff units in the Bandelier tuff in New Mexico that contain less than 10% glass, deform by brittle failure, whereas the non-welded units, with similar porosities, contain more than 60 % glass and form deformation bands (Riley et al. 2010). In this study the polygenic volcanic breccia and lapilli-tuff units that contain a large number of low-porosity lithic fragments, contain also less volcanic glass in the matrix. In contrast, the tuffaceous and ignimbritic units contain often a higher portion of glassy matrix, and less low-porosity lithic fragments. This may infer that the amount of porosity, glass content and the number of low-porosity lapilli and bombs could influence the style of deformation.

Fault zones consist commonly of several fault segments which may interact to form longer fault segments through linkage, bifurcation and/or jogging (e.g. Cartwright et al.,1995; Walsh et al., 2003; Peacock et al., 2017). Linking and interaction between segments may cause structural complex damage zones with a high density of structures (e.g. Dimmen et al., 2017). As seen from Figure 5.21, the fault zone increases in width and complexity towards the contractional steps. The contractional steps record a high connectivity and have large range in orientations of fractures, faults and deformation bands. In the middle part of the segments, the fault zone is narrower and less complex with mostly synthetic deformation bands and fractures.

The common view of fault zone architecture is that the damage zone thickness increases with displacement and will therefore widen through time (Shipton and Cowie, 2001; 2003). However, as already discussed in this section, lithology and structural location will influence the width and complexity of the fault zone, and displacement is therefore not the only controlling factor of the fault zone architecture. In the studied fault zones is the fault core in tuffaceous and ignimbritic units generally hard to distinguish from the damage zone, because of a broad zone of deformation bands which distribute the shear movement. Therefore, an expansion of a more general fault zone model proposed by Caine et. al (1996), which simply divide between fault core and the damage zone, is needed for faults in layered volcaniclastics successions. A more suitable model is proposed by Faulkner et al. (2003; 2010) which may apply for faults where the mechanical strength contrast between the fault zone and host rock is less than normally observed. The fault zone proposed by Faulkner et. al (2003) is comprised of multiple cores in an enveloping damage zone, which in turn correspond better to the observations done in Shithiping. In sum, both lithology and structural position of the fault will influence the fault architecture in a volcaniclastic succession, in addition to displacement.

6.4 Scaling relations and comparison with previous studies

Fault development can be characterised by the relationship between displacement and fault core thickness (Torabi and Berg, 2011). The distinction between fault core and damage zone is although ambiguous, as thickness vary along strike. Hence, the boarders between fault core and damage zone are subjective and open for interpretation (e.g. Faulkner et al., 2010; Torabi and Berg, 2011). The width of the fault core is also in this study hard to define in the parts where the fault exhibits distributed shear over a wide zone, as discussed in the previous section. Nonetheless, the fault core in these wide zones of distributed shear is defined as a high-density zone of deformation bands which display a displacement above 0.5 m. Despite the uncertainties of the definitions of a fault core and damage zone, scaling relations between fault core thickness and displacement are investigated by a number of authors (e.g. Scholz, 1987; Sperrevik et al., 2002; Childs et al. 2009; Torabi and Berg, 2011). The recorded data from this project and data collected of deformation bands and faults in carbonates from Tondi et al. (2012) are compared to global data compiled by Torabi and Berg (2011) and Johannesen (2017) (Fig. 6.4). The compiled data covers displacement-thickness (D-T) records from a range of articles (listed in the Fig. 6.4). The best power law relationship for the global data is ($T=0.026D^{0.7558}$) with a correlation coefficient (R^2) value of 0.7790 which indicate a good correlation. The global dataset include data from different lithologies and tectonic setting. This make the data less susceptible for scattering and includes a range of order of magnitude faults. Nevertheless, global dataset should be regarded with care, especially due to the subjective fault core definition and because different lithologies yield different mechanical strength and therefore different deformation mechanisms (e.g. Gross et al. 1997; Ackermann et al., 2001). Considering the D-T data form this project, it shows an elevated trend compared to the global data set. Likewise do the data from the carbonates provided by Tondi et al. (2012). This indicates that the deformation bands and faults in this study, and the one provided by Tondi et al. 2012) are general one order thicker than what is observed globally. Limited extent of the data in this study, in both range of displacement and numbers of data points, may cause this elevated trend in the graph. Small displacement faults are known to be more variability in fault core thickness compared to larger displacement faults (Torabi and Berg, 2011) Additionally, different definition of fault core thickness and weaker lithology could also explain the trend. More data is therefore needed to say whether faults in volcaniclastic rocks are thicker than what have been recorded in other lithologies. However, Walker et al. (2012) reported that D-T data from intralayered basalt and volcaniclastics in Faroe Island occupy the same field as data from fault zones in sedimentary rocks. Nonetheless, the gradient of the trendline in this project is similar to the global trendline, which implies that the studied faults will progress in a similar trend and manner as other faults studied globally.

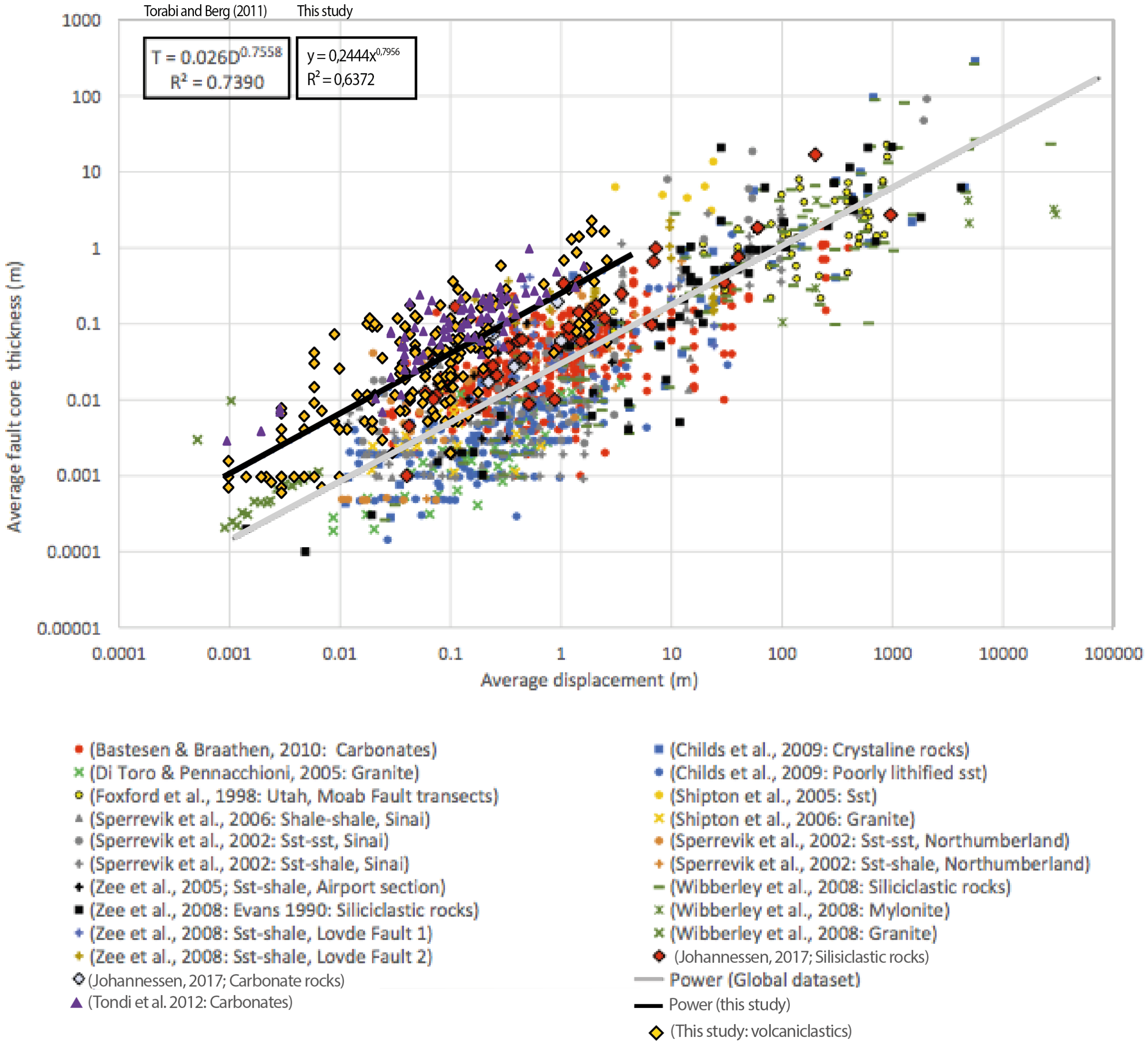

Figure 6.4: Log-log plot of displacement vs. fault core thickness modified from Johannesen (2017) and data compiled by Torabi and Berg (2011).

6.5 Implications for the flow properties of faults in volcaniclastic rocks

The understanding of deformation mechanisms affecting volcanic successions may be of economic importance as they could provide possible sub-surface reservoirs for fluid-related waste and resources (e.g. nuclear waste, hydrocarbons, minerals, hydrothermal energy and CO_2) (e.g. Sibson et al., 1988; Stagpoole, 2001; Schutter 2003; Hawkins, 2004; Rohrman, 2007; Oelkers and Cole, 2008; Walker et al., 2013). Faults, fractures and deformation bands are widely known to have an effect on fluid flow in subsurface reservoirs, in which they may act as pathways or barriers for fluids. (e.g. Aydin, 2000; Sibson et al., 2001; Fisher and Knipe, 2001; Bense and Person, 2006; Fossen and Bale, 2007; Barnicoat and Sheldon, 2009; Torabi et al. 2013; Wilson 2013b; Ballas et al. 2015)

In the studied volcaniclastic succession, porosity measurements of the layered host rock display generally high porosity readings which allow the sequence to be a good analogue for subsurface reservoirs/aquifers. However, the contrasting mechanical strength of layers in a multilayer sequence makes the deformation mechanisms variable discrete (brittle) or distributed shear (ductile) which will influence potential fluid flow (Schöpfer et al., 2006). Faults may serve as a conduit for fluids, in parts where discrete-slip accommodates the shear movement (Fig. 5.27). In addition, these sections constitute a depression in the terrain due to heavily weathering, which in turn could indicate enhanced fluid flow along the fault. (e.g. Rotevatn et al., 2008). Although the cataclasites in the core display very low porosity, the fluid could infiltrate slip surfaces and fractures (as seen in Fig. 5.28) in the fault core and damage zone. In contrast, the fault constitutes a broad zone of elevated deformation bands with a porosity as low as 1.6% in the deformation band-dominated parts. The resistance to weathering and low porosity implies low permeability (Torabi et al. 2013). Studies by Fosssen and Bale (2007) suggests that deformation bands may reduce permeability up to six orders of magnitude in porous sandstone. Moreover, previous studies underline the importance of clusters and cumulative thickness of deformation bands for an efficient permeability reduction, as a single deformation band has limited effect on fluid flow (Fossen and Bale, 2007; Torabi et al. 2013). The amount of cataclasis in the deformation band is related to the amount of permeability reduction in the band (Ballas et al. 2015). Consequently, deformation band clusters, slipped deformation bands and a distinctive fault core may exhibit a high sealing capacity. Whereas single cataclastic bands display a lower permeability contrast and will have limited effect in fluid flow. Accordingly, the structures forming in the initial fault stage will have limited effect on fluid flow, deformation bands forming in the intermediate stage may impede the fluid flow to some extent, whereas the faults in the area (which has the highest degree of cataclasis, including slip surfaces and fault core) forming at last stage may form barriers for fluid flow.

Evidence of paleofluids in the deformation bands and faults of Shithiping are visible along the deformation band boundaries and in slip surfaces as dark precipitated minerals (oxides) (Fig. 5.8), but also locally in the field as red redox fronts (Fig. 5.13). This may infer that the slip surfaces and deformation band boundaries contribute to enhanced anisotropic permeability along the bands (Rotevatn el at 2008; Torabi et al. 2014). However, the thick clusters and slip surfaces observed in the deformation band-dominated parts of the fault may baffle the fluid flow across the fault zone and act as a barrier that contributes to compartmentalization of a plausible reservoir.

Permeability of a fault zone is the product of the permeability and geometry of single structures, in which their distribution and connectivity could indicate the permeability of the entire fault zone (e.g Caine et al. 1996; Aydin 2000; Davatzes and Aydin 2003). The importance of connectivity of deformation bands on fluid flow is highlighted by Fossen and Bale (2007). High connectivity of deformation bands has a positive effect on the sealing capacity. The fault map in this study display a high connectivity in many areas, recorded by a high connecting node frequency (Fig 5.21c). As seen on Figure 5.21c, the tuff and ignimbritic units (in the central parts of segment 2) displays a high connectivity of deformation bands which emphasizes that this zone may work as a barrier for across fluid flow. In addition, the contractional steps exhibits a high node connectivity. Contractional steps (Fig. 5.21c) are comprised of a structural complex zone of deformation bands, short fractures and small faults. High connectivity of multi-oriented deformation bands and fractures in contractional steps could work as a conduit for fluid flow and be a passageway for cross-fault fluids (e.g. Rotevatn and Bastesen 2014; Dimmen et al., 2016). The structures in the contractional steps are similar to what have been reported for extensional relay ramps (e.g. Bastesen and Rotevatn 2012; Fossen and Rotevatn 2015) fault tips and fault intersections (e.g Gartell et al. 2004; Tamagawa and Pollard, 2008) which are all associated with enhanced fluid flow.

As volcaniclastics rocks often are comprised of a layered succession with variable porosity and clast content, the fault architecture will vary as well (as previously discussed, section 6.2). The faults may either serve as conduits in some parts of the fault zone and baffles for fluid flow in others, depending on the deformation mechanism. The great heterogeneities in the succession and the following fault architecture will create extensive heterogeneities in the permeability along and across the fault. This study has examined the fault architecture, fault zone topology and measured porosity and by doing so established that the faults could influence the fluid flow, if found in a subsurface reservoir. However, only direct permeability measurements can decisively prove effects of this kind.

7. SUMMARY AND CONCLUSIONS

By combining macro and microstructural analysis, this study has tried to characterise and elucidate the fault evolution in volcaniclastics successions. From the results and discussion presented in this thesis, following conclusions are made:

- Fault evolution can be divided into three successive stages using displacement as a proxy:
    - The *Initial stage* is characterised by simple band structures comprised of single strands which accommodate mm-cm-offset. Several deformation band strands and higher displacement are connected to relay zones. Cataclastic flow is the main deformation mechanism and may be initiated in weak volcanic glass.
    - The *Intermediate stage* of fault evolution includes more complex deformation band structures. Deformation band networks and clusters is common and the offset ranging from cm-scale to dm-scale. Patchy slip surfaces are developed locally. At micro scale is cataclasis the dominating deformation mechanism, while initial discrete brittle failure occurs locally at slip surfaces.
    - By the *final stage* a fault core comprised of one or several through-going slip surfaces and densely-spaced deformation bands accommodates dm-m-scale offsets. Microstructurally is this stage dominated by discrete brittle failure and subordinate cataclastic flow in the adjacent areas, and in the damage zone.
- This study has highlighted and described the variability in fault architecture as a function of lithology and fault segmentation. Fault architecture in volcaniclastic successions are dependent on the porosity, content of volcanic glass and number of low-porosity lapilli and bombs in the host rock. Relay zones are related to increased structural complexity at all stages of fault development.
- Scaling attributes for porous volcaniclastic rocks are provided by this study. Thickness of the structures generally follows a power law and increase with increased displacement.
- Topological analysis has visualised and quantified the variable connectivity of structural lineaments fault zones of volcaniclastic rocks.
- Fluid flow in plausible volcaniclastic sub-surface reservoir would be vulnerable for heterogeneities in across- and along fault fluid flow. Heterogeneities would be connected to mechanical strength of the host rock and the mode of failure.

Further work

After having conducted this study, serval questions concerning fault evolution and deformation banding in volcaniclastic successions still remains. Some ideas for further work that would improve the understanding of deformation mechanisms in volcaniclastic rocks could be:

- Microstructural studies of rock samples collected along-strike of incipient bands would be interesting to carry out in order to describe the development from zero displacement to mm-displacement. Additionally, would more in-detailed microstructural studies of the fault core be a topic for further investigations.
- Permeability measurements should be carried out on both different type of fault cores and deformation bands. This would improve the understanding on the total effect these structures have on fluid flow and how permeability may change through time.
- Systematic and quantitative measurements of the orientation of cleavage, fractures and preferred crystallographic orientation to investigate the role of mineral anisotropy on deformation in porous volcaniclastics
- More outcrop-based and quantitative studies of the damage zone of faults in volcaniclastics would be interesting to perform, as this study mainly focused on the fault core. In addition, larger-displacement faults should be studied in more detail to understand the development of scaling relations and fault architecture at larger displacements.
- There still is a lack of published studies in general on deformation bands and fault evolution in volcaniclastic rocks. In order to improve the understanding of the distribution, heterogeneity and development of deformation bands and faults in volcaniclastic rocks more outcrop-based studies and triaxial experimental studies of volcaniclastic rocks should be carried out.

8. LIST OF REFERENCES

Ackermann, R. V., Schlische, R. W., and Withjack, M. O. (2001), "The geometric and statistical evolution of normal fault systems: an experimental study of the effects of mechanical layer thickness on scaling laws», *Journal of Structural Geology*, vol. *23*(11), p. 1803-1819.

Angelier, J., E. Barrier, and H. T. Chu (1986), "Paleostress trajectories related to plate collision in the Foothills fold-thrust belt of Taiwan", *Tectonophysics,* vol. 125, p. 161–178.

Angelier, J., Chu, H.-T., and Lee, J. C., (1997), "Shear concentration in a collision zone: kinematics of the Chihshang Fault as revealed by outcrop scale quantification of active faulting, Longitudinal Valley, eastern Taiwan", *Tectonophysics*, v. 274, p. 117-143.

Antonellini, M. and Aydin, A., (1994), "Effect of faulting on fluid flow in porous sandstones: petrophysical properties" *AAPG bulletin,* vol. 78(3), p. 355-377.

Antonellini, M. A., Aydin, A. and Pollard, D. D., (1994), "Microstructure of deformation bands in porous sandstones at Arches National Park, Utah", *Journal of structural geology,* vol. 16(7), p. 941-959.

Avar, B. B., and N. W. Hudyma (2007), "Observations on the influence of lithophysae on elastic (Young's) modulus and uniaxial compressive strength of Topopah Spring Tuff at Yucca Mountain, Nevada, USA", *Int. J. Rock Mech. Min. Sci.*, vol. 44, p. 266–270

Aydin, A., (1978) "Small faults formed as deformation bands in sandstone", *Pure and applied geophysics*, vol. 116(4), p. 913–930.

Aydin, A., (2000), "Fractures, faults, and hydrocarbon entrapment, migration and flow", *Marine and petroleum geology,* vol. 17, p. 797-814.

Aydin, A., Borja, R. I., and Eichhubl, P. (2006), "Geological and mathematical framework for failure modes in granular rock" *Journal of Structural Geology*, vol. *28*(1), p. 83-98.

Aydin, A. and Johnson, A. M. (1978). "Development of faults as zones of deformation bands and as slip surfaces in sandstone", *Pure and applied geophysics*, vol. 116(4), p. 931–942.

Aydin, A. and Johnson, A. M. (1983), "Analysis of faulting in porous sandstones", *Journal of Structural Geology,* vol. 5(1), p. 19-31

Ballas, G., Fossen, H., and Soliva, R. (2015), "Factors controlling permeability of cataclastic deformation bands and faults in porous sandstone reservoirs", *Journal of Structural Geology*, vol. *76*, p. 1-21.

Barnicoat, A. C., Sheldon, H. A., and Ord, A., (2009), "Faulting and fluid flow in porous rocks and sediments: implications for mineralisation and other processes", *Mineralium Deposita*, *44*(6), 705-718.

Barrier, E., and Angelier, J., (1986), "Active collision in eastern Taiwan: the Coastal Range" *Tectonophysics*, vol. 125, (1-3), p. 39-72.

Bastesen, E. and Braathen, A. (2010). "Extensional faults in fine grained carbonates–analysis of fault core lithology and thickness–displacement relationships", *Journal of Structural Geology*, vol. *32*(11), p. 1609-1628.

Bense, V. F., Van den Berg, E. H. and Van Balen, R. T. (2003), "Deformation mechanisms and hydraulic properties of fault zones in unconsolidated sediments; the Roer Valley Rift System, The Netherlands", *Hydrogeology Journal*, vol. *11*(3), p. 319-332.

Bense, V. F. and Person, M. A. (2006), "Faults as conduit-barrier systems to fluid flow in siliciclastic sedimentary aquifers", *Water Resources Research*, vol. *42*(5).

Berg, S. S. and Skar, T. (2005), "Controls on damage zone asymmetry of a normal fault zone: outcrop analyses of a segment of the Moab fault, SE Utah", *Journal of Structural Geology*, vol. *27*(10), p. 1803-1822.

Bésuelle, P. (2001), "Compacting and dilating shear bands in porous rock: Theoretical and experimental conditions". *Journal of Geophysical Research: Solid Earth*, vol. *106*(B7), p. 13435-13442.

Bonnet, E., Bour, O., Odling, N.E., Davy, P., Main, I., Cowie, P., and Berkowitz, B. (2001), "Scaling of fracture systems in geological media", *Reviews of Geophysics*, vol. 39 (3), p. 347.

Brown, D., J. Alvarez-Marron, M. Schimmel, Wu, Y.-M. and Camanni G. (2012), "The structure and kinematics of the central Taiwan mountain belt derived from geological and seismicity data", *Tectonics*, vol. 31

Caine, J. S., Evans, J. P. & Forster, C. B. (1996), "Fault zone architecture and permeability structure". *Geology (Boulder)*, vol. 24, p. 1025-1028.

Cartwright, J. A., Trudgill, B. D. and Mansfield, C. S. (1995), "Fault growth by segment linkage: an explanation for scatter in maximum displacement and trace length data from the Canyonlands Grabens of SE Utah" *Journal of Structural Geology*, vol. *17*(9), p. 1319-1326

Cas, R. F., and Wright, J. V., (1987), *Volcanic successions: Modern and ancient*, London, Allen and Unwin, 528 p.

Cas, R. A. F. and Wright J. V. (1988), "Volcanic Successions. Modern and Ancient", *Geological Magazine*, vol. 125 (2), p. 189-200

Cavailhes, T., and Rotevatn, A. (Accepted), "Deformation bands in volcaniclastic rocks –insights from the Shihtiping tuffs, Coastal Range of Taiwan", *Journal of Structural Geology*.

Chai, B. H. T. (1972), "Structure and tectonic evolution of Taiwan", *American Journal of Science*, vol. 272, p. 389–422.

Chang, C.-P., Angelier, J., Huang, C.-Y., (2000) "Origin and evolution of a mélange: the active plate boundary and suture zone of the Longitudinal Valley, Taiwan", *Tectonophysics*, Vol. 325, Issues 1–2, 2000, p. 43-62.

Chemenda, A.I., Ballas, G. and Soliva, R., (2014), "Impact of a multilayer structure on initiation and evolution of strain localization in porous rocks: field observations and numerical modeling.", *Tectonophysics*, vol. 631, p. 29–36.

Chen, Y. G., Chen, W. S., Lee, J. C., Lee, Y. H., Lee, C. T., Chang, H. C., and Lo, C. H. (2001), "Surface rupture of 1999 Chi-Chi earthquake yields insights on active tectonics of central Taiwan", *Bulletin of the Seismological Society of America*, vol. *91*(5), p. 977-985.

Chen, W.-H., C.-Y. Huang, Y. Yan, Y. Dilek, D. Chen, M.-H. Wang, Zhang, X., Lan, Q., and Yu, M. (2017), "Stratigraphy and provenance of forearc sequences in the Lichi Mélange, Coastal Range: Geological records of the active Taiwan arc-continent collision", *Journal of Geophysical Research, Solid Earth*, vol. 122

Cheung, C.S.N., Baud, P. and Wong, T. (2012), "Effect of grain size distribution on the development of compaction localization in porous sandstone", *Geophysical Research Letters*, vol. 39, L. 21302,

Chi, W.R., Namson, J., and Suppe, J., (1981), "Stratigraphic record of plate interactions in the Coastal Range of eastern Taiwan", *Geological Society of China Memoir,* vol. 4, p. 155–194.

Childs, C., Manzocchi, T., Walsh, J.J., Bonson, C.G., Nicol, A. and Schöpfer, M.P. (2009), "A geometric model of fault zone and fault rock thickness variations". *Journal of Structural Geology*, vol. 31, p. 117-127.

Cilona, A., Baud, P., Tondi, E., Agosta, F., Vinciguerra, S., Rustichelli, A., and Spiers, C. J., (2012), "Deformation bands in porous carbonate grainstones: Field and laboratory observations", *Journal of Structural Geology*, vol. 45, p. 135-155.

Chin, S-J., Lin, J-Y., Chen, Y-F., Wu, W-N. and Liang, C-W., (2016) "Transition of the Taiwan-Ryukyu collision-subduction process as revealed by ocean-bottom seismometer observations", *Journal of Asian Earth Sciences*, vol. 128, p.149-157.

Ching, K.-E., R.-J. Rau, K. M. Johnson, J.-C. Lee, and J.-C. Hu (2011), "Present-day kinematics of active mountain building in Taiwan from GPS observations during 1995–2005", *Journal of Geophysical Research*, vol. 116.

Cowie P. A. and Scholz C. H. (1992a), "Physical explanation for the displacement-length relationship for faults using a post-yield fracture mechanics model", *Journal of Structural Geology***,** vol 14, p.1133–48.

Cowie P. A. and Schoz C. H. (1992b). "Displacement- length scaling relationship for faults: data synthesis and discussion", *Journal of Structural Geology,* vol. 14, p. 1149–56.

Cruikshank, K.M., Zhao, G. and Johnson, A.M. (1991), "Duplex structures connecting fault segments in Entrada Sandstone" *Journal of Structural Geology*, vol. 13, p. 1185-1196.

Davis, D., Suppe, J. and Dahlen, F.A., (1983), "Mechanics of fold and thrust belts and accretionary wedges", *Journal of Geophysical Research,* vol. 88, p. 1153–1172.

Dawers, N.H., and Anders, M.H. (1995) "Displacement-length scaling and fault linkage", *Journal of Structural Geology*, Vol 17 (5), p. 607-614.

Dimmen, V., Rotevatn, A., Peacock, D. C., Nixon, C. W. and Nærland, K. (2017), "Quantifying structural controls on fluid flow: Insights from carbonate-hosted fault damage zones on the Maltese Islands", *Journal of Structural Geology*, vol. *101*, p. 43-57.

Di Toro, G., Hirose, T., Nielsen, S., Pennacchioni, G., and Shimamoto, T. (2006), "Natural and experimental evidence of melt lubrication of faults during earthquakes", *Science*, vol. *311*(5761), p.647-649.

Du Bernard, X., Eichhubl, P. and Aydin, A., (2002), "Dilation bands: A new form of localized failure in granular media", *Geophysical Research Letters,* vol. 29(24), p. 29-1-29-4

Evans, J. P., and K. K. Bradbury (2004), "Faulting and fracturing of non- welded Bishop tuff, eastern California: Deformation mechanisms in very porous materials in the vadose zone", *Vadose Zone Journal*, vol. 3, p. 602–623

Ehrenberg, S.N. (1993), "Preservation of anomalously high porosity in deeply buried sandstones by grain-coating chlorite: examples from the Norwegian continental shelf", A*APG Bulletin*, vol. 77, p. 1260–1286.

Fairley, J. P. (2009), "Modeling fluid flow in a heterogeneous, fault-controlled hydrothermal system", *Geofluids*, vol. *9*(2), p. 153-166.

Faulkner, D. R., Jackson, C. A. L., Lunn, R. J., Schlische, R. W., Shipton, Z. K., Wibberley, C. A. J., and Withjack, M. O. (2010). "A review of recent developments concerning the structure, mechanics and fluid flow properties of fault zones". *Journal of Structural Geology*, vol. 32(11), p. 1557-1575.

Feng, Z. Q. (2008), "Volcanic rocks as prolific gas reservoir: a case study from the Qingshen gas field in the Songliao Basin, NE China", *Marine and Petroleum Geology*, vol. *25*(4-5), p. 416-432.

Ferreira, T., Rasband, W., (2012), ImageJ User Guide.

Ferrill, D. A., Morris, A. P., McGinnis, R. N., Smart, K. J., Wigginton, S. S., and Hill, N. J. (2017) "Mechanical stratigraphy and normal faulting", *Journal of Structural Geology*, vol. *94*, p.275-302.

Ferrill, D. A., Winterle, J., Wittmeyer, G., Sims, D., Colton, S., Armstrong, A., and Morris, A. P. (1999b). "Stressed rock strains groundwater at Yucca Mountain, Nevada", *GSA Today*, vol. *9*(5), p. 1-8.

Fisher, R.V., (1961) "Proposed classification of volcaniclastic sediments and rocks". *Geol Soc Am Bull,* vol. 71, p. 127–132

Fisher, Q., Knipe, R., and Worden, R. (2000), "Microstructures of deformed and non-deformed sandstones from the North Sea: implications for the origins of quartz cement in sandstones: Quartz Cementation in Sandstones", *Special Publication 29 of the IAS*, vol. 14, p. 129-146.

Fisher, R. V., G. Heiken, and M. Mazzoni (2006), "Where do tuffs fit into the framework of volcanoes?", *Tuffs—Their Properties, Uses, Hydrology, and Resource*s, edited by G. Heiken, *Spec. Pap. Geol. Soc. Am.*, vol. 408, p. 5–9.

Fossen, H., and Bale, A. (2007), "Deformation bands and their influence on fluid flow" *AAPG bulletin*, vol. *91*(12), p. 1685-1700.

Fossen, H., and Hesthammer, J. (1997). "Geometric analysis and scaling relations of deformation bands in porous sandstone." *Journal of Structural Geology*, vol. 19(12), p. 1479-1493.

Fossen, H., Hesthammer, J., (2000), "Possible absence of small faults in the Gullfaks Field, northern North Sea: implications for downscaling of faults in some porous sandstones". *Journal of Structural Geology,* vol. 22, p. 851-863.

Fossen, H., Schultz, R. A., Shipton, Z. K., and Mair, K., (2007), "Deformation bands in sandstone: a review", *Journal of the Geological Society*, vol. 164, p. 755-769.

Fossen, H., Soliva, R., Ballas, G., Trzaskos, B., Cavalcante, C., and Schultz, R. A., (2018), "A review of deformation bands in reservoir sandstones: geometries, mechanisms and distribution" *Geological Society, London, Special Publications*, vol. 459.

Fossen, H., Zuluaga, L.F., Ballas, G., Soliva, R., and Rotevatn, A., (2015), "Contractional deformation of porous sandstone: Insights from the Aztec Sandstone in the footwall to the Sevier-age Muddy Mountains thrust, SE Nevada, USA", *Journal of Structural Geology*, vol. 74, p. 172–184

Foxford, K. A., Walsh, J. J., Watterson, J., Garden, I. R., Guscott, S. C., and Burley, S. D. (1998), "Structure and content of the Moab Fault Zone, Utah, USA, and its implications for fault seal prediction", *Geological Society, London, Special Publications*, vol. *147*(1), p. 87-103.

Freundt, A., Wilson, C.J.N. and Carey, S.N., (2000), "Ignimbrites and Block-and-Ash Flow Deposits", *Encyclopedia of Volcanoes*, Academic Press, p. 581-599.

Gallagher, J., Friedman, M., Handin, J., and Sowers, G., (1974), "Experimental studies relating to microfracture in sandstone", *Tectonophysics*, vol. 21, p. 203-247

Gibson, R. G. (1998), "Physical character and fluid-flow properties of sandstone-derived fault zones". *Geological Society, London, Special Publications*, vol. 127(1), p. 83

Green, G. R., Solomon, M. and Walshe, J. L. (1981), "The formation of the volcanic-hosted massive sulfide ore deposit at Rosebery, Tasmania", *Economic Geology*, vol. *76*(2), p. 304-338.

Gross, M. R., Gutie, G., Bai, T., Wacker, M. A., Collinsworth, K. B., and Behl, R. J. (1997), "Influence of mechanical stratigraphy and kinematics on fault scaling relations", *Journal of Structural Geology*, vol. *19*(2), p. 171-183.

Hawkins, D. G. (2004), "No exit: thinking about leakage from geologic carbon storage sites", *Energy*, vol. *29*(9-10), p. 1571-1578.

Hesthammer, J. and Fossen, H. (2001), "Structural core analysis from the Gullfaks area, northern North Sea". *Marine and Petroleum Geology*, vol. 18(3), p. 411 – 439.

Heynekamp, M. R., Goodwin, L. B., Mozley, P. S., and Haneberg, W. C. (1999), "Controls on Fault-Zone Architecture in Poorly Lithified Sediments, Rio Grande Rift, New Mexico: Implications for Fault-Zone Permeability and Fluid Flow", *Faults and subsurface fluid flow in the shallow crust*, p. 27-49.

Hsieh, M.-L., Liew, P.-M., and Hsu, M.-Y. (2004), "Holocene tectonic uplift on the Hua-tung coast, eastern Taiwan" *Quaternary International*, vol. 115, p. 47-70.

Hsu, L., and Burgmann, R., (2006), "Surface creep along the Longitudinal Valley fault, Taiwan from InSAR measurements, *Geophysical Research letters,* vol. 33.

Hsu, T. L. (1956), "Geology of the Coastal Range, eastern Taiwan", *Bull. Geol. Surv. Taiwan*, vol. 8, p. 39–64

Hsu, V., (1990), "Seismicity and tectonics of a continent-island arc collision zone at the island of Taiwan" *Journal of Geophysical Research,* vol. 95, p. 4725–4734.

Huang, C.Y., Yuan, P.B., Teng, L.S., (1988), "Paleontology of the Kangkou Limestone in the middle Coastal Range, eastern Taiwan". *Acta Geologica Taiwanica*, vol. 26, p. 133-160.

Huang, C. Y., Yuan, P. B., Lin, C.W., and Wang, T. K., (2000), "Geodynamic processes of Taiwan arc-continent collision and comparison with analogs in Timor, Papua New Guinea, Urals and Corsica", *Tectonophysics*, vol. 325, p. 1–21

Huang, C.-Y., Yuan, P.B. & Tsao, S.-J., (2006), "Temporal and spatial records of active arc-continent collision in Taiwan: a synthesis*", GSA Bulletin.*, vol. 118(3/4), p. 274–288.

Huang, C. Y., Yen, Y., Zhao, Q., and Lin, C. T. (2012), "Cenozoic stratigraphy of Taiwan: Window into rifting, stratigraphy and paleoceanography of South China Sea", *Chinese science bulletin*, vol. *57*(24), p. 3130-3149.

Hynek, B. M., R. J. Phillips, and R. E. Arvidson (2003), "Explosive volcanism in the Tharsis region: Global evidence in the Martian geologic record", *J. Geophys. Res.*, vol. 108(E9), p. 5111

Johannessen, M. U. (2017), "Fault core and its geostatistical analysis; Insight into the fault core thickness and fault displacement", MSc. Thesis, University of Bergen 131 p.

Johansen, T. E. S. and Fossen, H. (2008), "Internal geometry of fault damage zones in interbedded siliciclastic sediments." *Geological Society, London, Special Publications*, vol. 299(1), p. 35-56

Johnston, J.D., and McCaffrey, K.J.W. (1996), "Fractal geometries of vein systems and the variation of scaling relationships with mechanism", *Journal of Structural Geology*, vol. 18, (2-3), p. 349–358

Kaproth, B. M., Cashman, S. M., and Marone, C. (2010), "Deformation band formation and strength evolution in unlithified sand: the role of grain breakage", *Journal of Geophysical Research: Solid Earth*, vol. *115*(B12).

Kim, Y-S., Peacock, D. C. P. and Sanderson, D. J., (2004) "Fault damage zones", *Journal of Structural Geology,* vol. 26, p. 503-517.

Kim, Y-S. and Sanderson, D. J (2005) "The relationship between displacement and length of faults: a review", *Earth-Science Reviews,* Vol. 68 (3–4), p. 317-334

Kjenes, M., (2018), "The geometry and evolution of deformation bands in volcaniclastic rocks: insights from Eastern Taiwan" MSc. Thesis, University of Bergen, Bergen 85 p.

Knipe, R. J., Larsen R. M., Brekke H., Larsen B. Y. and Talleraas E. (1992), "Faulting processes and fault seal", *Norwegian Petroleum Society Special Publications*, vol. 1, p 325–342.

Knott, S. D., Beach, A., Brockbank, P. J., Brown, J. L., McCallum, J. E., and Welbon, A. I. (1996), "Spatial and mechanical controls on normal fault populations", *Journal of Structural Geology*, vol. *18*(2-3), p. 359-372.

Knipe, R. J., Fisher, Q. J., Jones, G., Clennell, M. R., Farmer, A. B., Harrison, A., and White, E. A. (1997), "Fault seal analysis: successful methodologies, application and future directions". *Norwegian Petroleum Society Special Publications*, Vol. 7, p. 15-38.

Lai, Y.M. and Song, S.R., (2013), "The volcanoes of an oceanic arc from origin to destruction: a case from the northern Luzon Arc", *Journal of Asian Earth Sciences*, vol. 74, p. 97–112.

Lallemand, S., Liu, C.S., Dominguez, S., and Schrurle, P., Malavieille, J., and the ACT scientific crew, (1999), "Trench-parallel stretching and folding of forearc basins and lateral migration of the accretionary wedge in the southern Ryukyus: A case of strain partition caused by oblique convergence" *Tectonics*, vol. 18, p. 231–247.

Lallemand, S., Front, Y., Bijwaard, H., and Kao, H., (2001), "New insights on 3-D plates interaction near Taiwan from tomography and tectonic implications", *Tectonophysics*, vol. 335, p. 229–253.

Lee, T.Q., Kissel, C., Barrier, E., Laj, C., and Chi, W., (1991), "Paleomagnetic evidence for a diachronic clockwise rotation of the Coastal Range, eastern Taiwan" *Earth and Planetary Science Letters*, vol. 104, p. 245–257

Lee, Y. H., C. C. Chen, T. K. Liu, H. C. Ho, H. Y. Lu, and W. Lo (2006), "Mountain building mechanisms in the Southern Central Range of the Taiwan Orogenic Belt—From accretionary wedge deformation to arc–continental collision", *Earth Planetary Science Letters,* vol. 252(3), p. 413–422

Lee, Y. H., T. Byrne, W. H. Wang, W. Lo, R. J. Rau, and H. Y. Lu (2015), "Simultaneous mountain building in the Taiwan orogenic belt", *Geology*, vol. 43(5), p. 451–454.

Lenhardt, N., and Götz, A. E. (2011), "Volcanic settings and their reservoir potential: An outcrop analog study on the Miocene Tepoztlán Formation, Central Mexico", *Journal of Volcanology and Geothermal Research*, vol. *204*(1-4), p. 66-75.

Lenhardt, N., and Götz, A. E. (2015). «Geothermal reservoir potential of volcaniclastic settings: the Valley of Mexico, Central Mexico». *Renewable Energy*, vol. *77*, p. 423-429.

Leveille, G.P., Knipe, R. and More, C. (1997), "Compartmentalization of Rotliegendes gas reservoirs by sealing faults, Jupiter Fields area, southern North Sea". In: Ziegler, K., Turner, P. & Daines, S.R. (eds) Petroleum Geology of the Southern North Sea; Future Potential. *Geological Society, London, Special Publications*, vol. 123, p. 87–104.

Lin, A. T., Watts, A. B. and Hesselbo, S. P. (2003), "Cenozoic stratigraphy and subsidence history of the South China Sea margin in the Taiwan region". *Basin Research*, vol. 15(4), p. 453-478.

Lin, C. H. (2002), "Active continental subduction and crustal exhumation: The Taiwan orogeny", *Terra Nova*, vol. 14, p. 281–287.

Lin, S-T. and Huang, W-J. (2014), "Deformation Bands in Ignimbrite in Shihtiping, Eastern Taiwan", *American Geophysical Union, Fall Meeting*, poster.

Lindsey, D. A., (1982), "Tertiary volcanic rocks and uranium in the Thomas Range and northern Drum Mountains, Juab County, Utah", *USGPO*, p. 2330-7102.

Liu, T. K., S. Hsieh, Y. G. Chen, and W. S. Chen (2001), "Thermo-kinematic evolution of the Taiwan oblique-collision mountain belt as revealed by zircon fission track dating", *Earth Planet. Science Letters*, vol. 186(1), p. 45–56.

Magara, K. (2003), "Volcanic reservoir rocks of northwestern Honshu Island, Japan.", *Geological Society, London, Special Publications*, vol. 214(1), p. 69-81.

Mair, K., Main, I. and Elphick, S. (2000). "Sequential growth of deformation bands in the laboratory." *Journal of Structural Geology,* vol. 22, p. 25-42.

Mair, K., Frye, K. M. and Marone, C. (2002), “Influence of grain characteristics on the friction of granular shear zones”. *Journal of Geophysical Research: Solid Earth*, vol. *107*(B10).

Malavieille, J., S. E. Lallemand, S. Dominguez, A. Deschamps, C. Y. Lu, C. S. Liu, P. Schnürle, and the ACT Scientific Crew (2002), “Arc-continentcollision in Taiwan: New marine observations and tectonic evolution”, *Geol. Soc. Am. Spec. Pap.*, vol. 358, p. 187–211.

Malavieille, J., and Trullenque, G. (2009), “Consequences of continental subduction on forearc basin and accretionary wedge deformation in SE Taiwan: Insights from analogue modeling”, *Tectonophysics*, vol. *466*(3-4), p. 377-394.

Mandl, G., De Jong, L. and Maltha, A. (1977), "Shear zones in granular material". *Rock Mechanics,* vol. 9(2-3), p. 95-144.

Manzocchi, T. (2002). “The connectivity of two-dimensional networks of spatially correlated fractures”, *Water Resources Research*, vol. 38, p. 1-20.

Mollema, P. and Antonellini, M., (1996), "Compaction bands: a structural analog for anti-mode I cracks in aeolian sandstone", *Tectonophysics,* vol. 267(1), p. 209-228.

Moon, V. (1993a), "Microstructural controls on the geomechanical behaviour of ignimbrite", *Eng. Geol.*, vol. 35, p. 19–31

Moon, V., (1993b), "Geotechnical characteristics of ignimbrite: A soft pyro- clastic rock type", *Eng. Geol.*, vol. 35, p. 33–48

Morley, C. and Nixon, C. (2016), “Topological characteristics of simple and complex normal fault networks”. *Journal of Structural Geology*, vol. 84, p. 68-84.

Neeper, D. A., and Gilkeson, R. H. (1996), “The influence of topography, stratigraphy, and barometric venting on the hydrology of unsaturated Bandelier Tuff”, *Mountains Region. Guidebook*, vol. *47*, p. 427-443.

Nicchio, M. A., Nogueira, F. C., Balsamo, F., Souza, J. A., Carvalho, B. R. and Bezerra, F. H. (2017), “Development of cataclastic foliation in deformation bands in feldspar-rich conglomerates of the Rio do Peixe Basin, NE Brazil”. *Journal of Structural Geology*.

Nicol, A., Childs, C., Walsh, J.J. and Schafer, K.W., (2013), "A geometric model for the formation of deformation band clusters", *Journal of Structural Geology*, vol. 55, p. 21–33.

Nyberg, B., Nixon, C.W. and Sanderson, D.J., (2018), “NetworkGT: A GIS tool for geometric and topological analyses of two-dimensional fracture networks”. *Geosphere,* vol. *14*.

Oelkers, E. H. and Cole, D. R. (2008), “Carbon dioxide sequestration a solution to a global problem”, *Elements*, vol.*4*(5), p. 305-310.

Okubo, C. H. (2012), “Spatial distribution of damage around faults in the Joe Lott Tuff Member of the Mount Belknap Volcanics, Utah: A mechanical analog for faulting in pyroclastic deposits on Mars”, *Journal of Geophysical Research: Planets*, vol. *117*(E8).

Okubo, C. H., and Schultz, R. A. (2006), “Near-tip stress rotation and the development of deformation band stepover geometries in mode II”, *Geological Society of America Bulletin*, vol. *118*(3-4), p. 343-348.

Ortega, O. and Marrett, R. (2000), “Prediction of macrofracture properties using microfracture information, Mesaverde Group sandstones, San Juan basin, New Mexico”, *Journal of Structural Geology*, vol. 22, p. 571-588.

Pathier, E., Fruneau, B., Deffontaines, B., Angelier, J., Chang, C.-P., Yu, S.-B., and Lee, C.-T. (2003), “Coseismic displacements of the footwall of the chelungpu fault caused by the 1999, taiwan, chi-chi earthquake from insar and gps data.”, *Earth and Planetary Science Letters*, vol. 212(1-2), p. 73–88.

Peacock, D. C. P., and Sanderson, D. J. (1991). "Displacements, segment linkage and relay ramps in normal fault zones". *Journal of Structural Geology*, vol. 13(6), p. 721-733.

Peacock, D. C. P., Nixon, C., Rotevatn, A., Sanderson, D. and Zuluaga, L. (2016), "Glossary of fault and other fracture networks". *Journal of Structural Geology*, vol. 92, p. 12-29.

Peacock, D. C. P., Dimmen, V., Rotevatn, A., and Sanderson, D. J. (2017), "A broader classification of damage zones". *Journal of Structural Geology*, vol. 102, p. 179-192.

Philit S., Soliva, R., Ballas, G. and Fossen H., (2017), "Grain Deformation Processes in Porous Quartz Sandstones – Insight from the Clusters of Cataclastic Deformation Bands", *EPJ Web of Conferences,* vol. *140*, pp. 07002.

Procter, A., and Sanderson, D. J. (2017), "Spatial and layer-controlled variability in fracture networks", *Journal of Structural Geology*.

Ramsey, L. A., Walker, R. T., and Jackson, J. (2007), "Geomorphic constraints on the active tectonics of southern Taiwan" *Geophysical Journal International*, vol. *170*(3), p.1357-1372.

Riley, P. R., L. B. Goodwin, and C. J. Lewis (2010), "Controls on fault damage zone width, structure, and symmetry in the Bandelier tuff, New Mexico", *J. Struct. Geol.*, vol. 32, p. 766–780

Rohrman, R. (2007), "Prospectivity of volcanic basins: Trap delineation and acreage de-risking". *AAPG Bulletin*, vol. 91 (6), p. 915–939.

Rotevatn, A. and Bastesen, E. (2014), "Fault linkage and damage zone architecture in tight carbonate rocks in the Suez Rift (Egypt): implications for permeability structure along segmented normal faults", *Geological Society, London, Special Publications,* vol. 374**,** 79-95.

Rotevatn, A. and Fossen, H., (2012), "Soft faults with hard tips: magnitude-order displacement gradient variations controlled by strain softening versus hardening; implications for fault scaling" *Journal of the Geological Society*, vol. 169(2), p. 123-126.

Rotevatn, A., Sandve, T.H., Keilegavlen, E., Kolyukhin, D. and Fossen, H. (2013), "Deformation bands and their impact on fluid flow in sandstone reservoirs: the role of natural thickness variations". *Geofluids*, vol. 13, p. 359–371

Rotevatn, A., Thorsheim, E., Bastesen, E., Fossmark, H., Torabi, A., and Sælen, G., (2016). "Sequential growth of deformation bands in carbonate grainstones in the hangingwall of an active growth fault: Implications for deformation mechanisms in different tectonic regimes", *Journal of Structural Geology,* vol. *90*, p. 27-47.

Rotevatn, A., Torabi, A., Fossen, H. and Braathen, A., (2008), "Slipped deformation bands: a new type of cataclastic deformation bands in Western Sinai, Suez rift, Egypt". *Journal of Structural Geology,* vol. 30, p. 1317 – 1331.

Rowland, J. V., and Sibson, R. H. (2004). Structural controls on hydrothermal flow in a segmented rift system, Taupo Volcanic Zone, New Zealand. *Geofluids*, *4*(4), 259-283.

Russell, J.K. and Quane, S.L., 2005. "Rheology of welding: inversion of field constraints". *J. Volcanol. Geotherm. Res*. vol. 142, p. 173–191.

Sanderson, D. J. and Nixon, C. W. (2015), "The use of topology in fracture network characterization" *Journal of Structural Geology*, vol. 72, p. 55-66.

Schultz, R. A., and Balasko, C. M. (2003), "Growth of deformation bands into echelon and ladder geometries". *Geophysical Research Letters*, vol. *30*(20).

Schulz, S.E. and Evans, J.P. (1998), "Spatial variability in microscopic deformation and composition of the Punchbowl fault, southern California: implications for mechanisms, fluid-rock interaction and fault morphology". T*ectonophysics*, vol. 295, p. 223-244.

Schultz, R. A., and Siddharthan, R. (2005), “A general framework for the occurrence and faulting of deformation bands in porous granular rocks”, *Tectonophysics*, vol. 411(1-4), p. 1-18.

Schultz, R. A., Soliva, R., Fossen, H., Okubo, C. H., and Reeves, D. M. (2008), “Dependence of displacement–length scaling relations for fractures and deformation bands on the volumetric changes across them”, *Journal of Structural Geology*, vol. *30*(11), p. 1405-1411.

Schutter, S. R. (2003), “Hydrocarbon occurrence and exploration in and around igneous rocks”. *Geological Society, London, Special Publications*, vol. *214*(1), p. 7-33.

Shipton, Z. K., and Cowie, P. A. (2001), “Damage zone and slip-surface evolution over μm to km scales in high-porosity Navajo sandstone, Utah.” *Journal of Structural Geology*, vol. 23(12), p.1825-1844.

Shipton, Z. K., and Cowie, P. A. (2003), “A conceptual model for the origin of fault damage zone structures in high-porosity sandstone”. *Journal of Structural Geology*, vol. 25(3), p 333-344.

Shipton, Z. K., J. P. Evans, and L. B. Thompson, (2005), “The geometry and thickness of deformation-band fault core and its influence on sealing characteristics of deformation-band fault zones”, *Faults, fluid flow, and petroleum traps: AAPG Memoir,* vol.85, p. 181–195.

Shipton, Z. K., Soden, A. M., Kirkpatrick, J. D., Bright, A. M. and Lunn, R. J. (2006) “How thick is a fault? Fault displacement-thickness scaling revisited*”. Earthquakes: Radiated Energy and the Physics of Faulting*, p. 193-198.

Shyu, J. B. H., K. Sieh, Y.-G. Chen, and C.-S. Liu (2005), “Neotectonic architecture of Taiwan and its implications for future large earthquakes”, *J. Geophys. Res*., vol. 110, B08402

Sibson, R. H., Robert, F. and Poulsen, K. H. (1988), “High-angle reverse faults, fluid-pressure cycling, and mesothermal gold-quartz deposits”, *Geology*, vol. *16*(6), p. 551-555.

Sibuet, J.-C. and Hsu S.-K. (2004). "How was Taiwan created*?*" *Tectonophysics*, Vol. 379(1), p. 159-181.Sillitoe, R. H., and Bonham, H. F. (1984), “Volcanic landforms and ore deposits”, *Economic Geology*, vol. *79*(6), p. 1286-1298.

Simoes, M., Avouac, J.P., Beyssac, O., Goffé, B., Farley, K.A., and Chen, Y.-G. (2007), “Mountain building in Taiwan: A thermokinematic model*”, Journal of Geophysical Research*, vol. 112, B11405

Soden A.M. and Shipton Z.K., (2013). "Dilational fault zone architecture in a welded ignimbrite: The importance of mechanical stratigraphy". *Journal of Structural Geology*, vol. 51, p. 156–166

Soliva, R., Ballas, G., Fossen, H. and Philit, S., (2016), "Tectonic regime controls clustering of deformation bands in porous sandstone", *Geology*, vol. 44, p. 423–426.

Soliva, R., Schultz, R.A., Ballas, G., Taboada, A., Wibberley, C.A.J., Saillet, E. and Benedicto, A., (2013) “A model of strain localization in porous sandstone as a function of tectonic setting, burial and material properties; new insight from Provence (SE France)”. *Journal of Structural Geology,* vol. 49, p. 50-63.

Song, S.-R., and Lo, H.-J., (1988), “Volcanic geology of Fengpin-Takangkou area, coastal range of Taiwan”, *Yánjiū bāogāo-Guólė Táiwān dāxué. Lǐxuéyuān dėzhėxué xė*, vol. 26, p. 223- 235.

Song, S.-R., and Lo, H.-J., (2002). ”Lithofacies of volcanic rocks in the central Coastal Range, eastern Taiwan: implications for island arc evolution”. *Journal of Southeast Asian Earth Sciences,* vol. 21, p. 23–38.

Sperrevik, S., Gillespie, P. A., Fisher, Q. J., Halvorsen, T., and Knipe, R. J. (2002), “Empirical estimation of fault rock properties”, *Norwegian Petroleum Society Special Publications*, vol. 11, p. 109-125.

Sruoga, P., and Rubinstein, N. (2007), “Processes controlling porosity and permeability in volcanic reservoirs from the Austral and Neuquén basins, Argentina”. *AAPG bulletin*, vol. 91(1), p. 115-129.

Stagpoole, V and Funnel, R. (2001), “Arc magmatism and hydrocarbon generation in the northern Taranaki Basin, New Zealand”, *Petroleum Geoscience,* vol. 3, p. 255-287

Storvoll, V., Bjørlykke, K.O., Karlsen, D. and Saigal, G., (2002), "Porosity preservation in reservoir sandstones due to grain-coating illite: a study of the Jurassic Garn Formation from the Kristin and Lavrans fields, offshore Mid- Norway", *Marine and Petroleum Geology*, vol. 19, p. 767–781.

Suppe, J., (1981), "Mechanics of mountain-building and metamorphism in Taiwan", *Memoairs Geol. Soc. China,* vol. 4, p. 67-89.

Teng, L. S. (1990), "Geotectonic evolution of late Cenozoic arc-continent collision in Taiwan" *Tectonophysics,* vol. 183(1-4), p. 57-76.

Teng, L.S., Lo, H.J., (1985). "Sedimentary sequences in the island arc settings of the Coastal Range, eastern Taiwan". *Acta Geologica Taiwanica,* vol. 23, p. 77–98.

Teng, L. S. and Wang, Y. (1981), "Island arc system of the Coastal Range, eastern Taiwan", *Proceedings of the Geological Society of China*, vol. 24, p. 99-112

Thomas, M. Y., Avouac, J. P., Champenois, J., Lee, J. C., and Kuo, L. C. (2014), "Spatiotemporal evolution of seismic and aseismic slip on the Longitudinal Valley Fault, Taiwan", *Journal of Geophysical Research: Solid Earth*, vol. *119*(6), p. 5114-5139

Thorsheim, E., (2015), "The geometry and evolution of deformation bands in carbonate grainstones along the Maghlaq Fault, Malta", MSc. thesis, University of Bergen, Bergen, 91 p.

Tondi, E. (2007), "Nucleation, development and petrophysical properties of faults in carbonate grainstones: evidence from the San Vito Lo Capo peninsula (Sicily, Italy)", *Journal of Structural Geology*, vol. *29*(4), p. 614-628.

Tondi, E., Antonellini, M., Aydin, A., Marchegiani, L., and Cello, G., (2006), "The role of deformation bands, stylolites and sheared stylolites in fault development in carbonate grainstones of Majella Mountain, Italy", J*ournal of Structural Geology*, vol. 28(3), p. 376-391.

Tondi, E., Cilona, A., Agosta, F., Aydin, A., Rustichelli, A., Renda, P., and Giunta, G. (2012), "Growth processes, dimensional parameters and scaling relationships of two conjugate sets of compactive shear bands in porous carbonate grainstones, Favignana Island, Italy,. *Journal of Structural Geology*, vol *37*, p. 53-64.

Torabi, A., and Berg, S. S. (2011), "Scaling of fault attributes: A review", *Marine and Petroleum Geology*, vol. *28*(8), p. 1444-1460.

Torabi, A., Fossen, H., and Braathen, A., (2013), "Insight into petrophysical properties of deformed sandstone reservoirs", *AAPG bulletin*, vol. 97 (4), p. 619-637.

Twiss, R., and Moores, E., (1992), *Structural Geology*, Freeman, New York, 388 p

Walker, G.P.L., (1983), "Ignimbrite types and ignimbrite problems", *J. Volcanol. Geotherm. Res.*, vol. 17, p. 65-88

Walker, R. J., Holdsworth, R. E., Imber, J., and Ellis, D. (2012), "Fault-zone evolution in layered basalt sequences: A case study from the Faroe Islands, NE Atlantic margin", *Bulletin*, vol. *124*(7-8), p. 1382-1393.

Walker, R. J., Holdsworth, R. E., Imber, J., Faulkner, D. R., and Armitage, P. J. (2013), "Fault zone architecture and fluid flow in interlayered basaltic volcaniclastic-crystalline sequences". *Journal of Structural Geology*, vol. *51*, p. 92-104.

Walsh, J. J., Bailey, W. R., Childs, C., Nicol, A., and Bonson, C. G. (2003), "Formation of segmented normal faults: a 3-D perspective", *Journal of Structural Geology*, vol. *25*(8), p. 1251-1262.

Walsh, J. J. and Watterson, J., (1988), "Analysis of the relationship between displacements and dimensions of faults", *Journal of Structural Geology,* vol.10, p. 239-247.

Walsh, J. J. & Watterson, J. (1991), "Geometric and kinematic coherence and scale effects in normal fault systems", *Geological Society, London, Special Publications*, vol. 56, p. 193-203.

Walsh, J. J., Nicol, A. and Childs, C. (2002), "An alternative model for the growth of faults." *Journal of Structural Geology*, vol. 24(11), p. 1669-1675.

White, J. D. L., and Houghton, B. F. (2006). Primary volcaniclastic rocks. *Geology*, vol. *34*(8), p. 677-680.

Wibberley, C. A., Yielding, G., and Di Toro, G. (2008). Recent advances in the understanding of fault zone internal structure: a review. *Geological Society, London, Special Publications*, vol. *299*(1), p. 5-33.

Wilson, J. E., (2004) "Characteristics of faults in nonwelded ignimbrites from the Pajarito Plateau and implications for fluid flow", Phd. Thesis: New Mexico Institute of Mining and Technology

Wilson, J. E., L. B. Goodwin, and C. J. Lewis (2003), "Deformation bands in nonwelded ignimbrites: Petrophysical controls on fault-zone deformation and evidence of preferential fluid flow", *Geology*, vol. 31, p. 837–840,

Wilson, J. E., Goodwin, L. B., and Lewis, C. (2006), "Diagenesis of deformation band faults: Record and mechanical consequences of vadose zone flow and transport in the Bandelier Tuff, Los Alamos, New Mexico", *Journal of Geophysical Research: Solid Earth*, vol. *111*(B9).

Wolfe, J.A., (1981). "Philippine geochronology", *Journal of Geological Society of Philippines*, vol. 35, p. 1–30.

Wong, T.F., David, C. and Zhu, W. (1997). "The transition from brittle faulting to cataclastic flow in porous sandstones: mechanical definition", *Journal of Geophysical Research,* vol.102, p. 3009-3025.

Yang, T.Y., Liu, T.K., and Chen, C.H., (1988), "Thermal event records of the Chimei igneous complex: Constraint on the ages of magma activities and the structural implication based on fission track dating", *Acta Geologica Taiwanica*, vol. 26, p. 237–246.

Yang, T.Y., Tien, J.L., Chen, C.H., Lee, T., and Punong-Bayan, R., (1995), "Fission-track dating of volcanics in the northern part of the Taiwan-Luzon arc: Eruption ages and evidence for crustal contamination", *Journal of SE Asian Earth Sciences*, vol. 11, p. 81–93.

Yu, S-B. and Liu, C-C., (1989), "Fault creep on the central segment if the Longitudinal Valley Fault, Eastern Taiwan", *Proceedings of the Geological Society of China*, vol. 32 (3), p.209-231

Zhu, W., Baud, P., Vinciguerra, S. and Wong, T.-F., (2011), "Micromechanics of brittle faulting and cataclastic flow in Alban Hills tuff" *J. Geophys. Res.* Vol. 116, B06209.

Appendix I: Additional figures of incipient deformation bands

Figure of deformation band 5 with grain size plot along the band

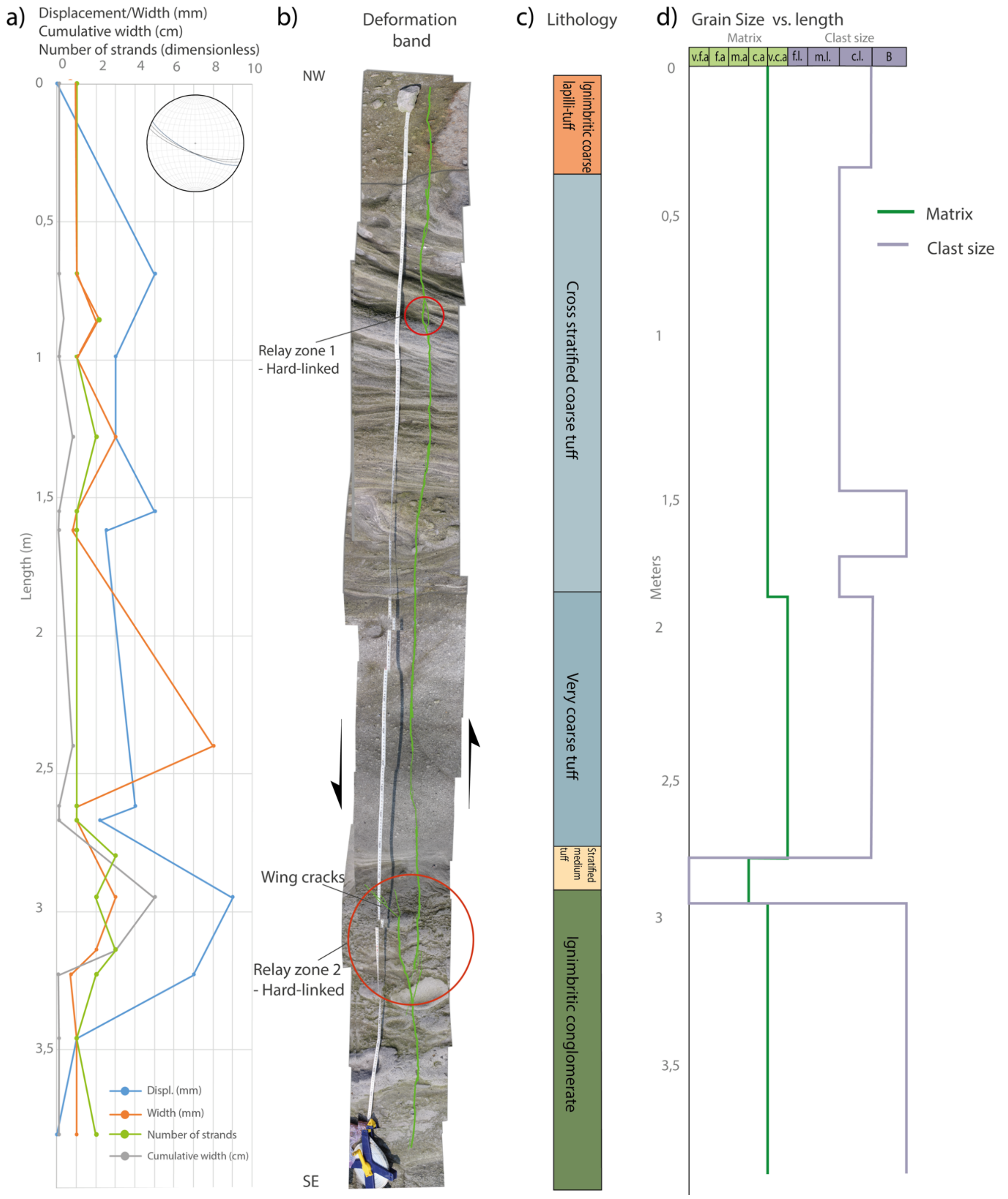

Summary figure of band 5; the location of band 5 is shown in Figure 5.11A. The top of the figure point towards the NW, A) A diagram over different parameters along the band. Displacement and width are measured in millimetres, cumulative width is displayed in cm and the number of strands is dimensionless. The lower-hemisphere stereonet shows the orientation of band 5. B) Photomosaic over band 5 with green line drawings illustrating the DB. Kinematic indicators are displayed by black arrows. Zones of interest is highlighted with red circles. C) A block diagram of the lithology along the band. D) Grain size plot.

Incipient deformation band 6

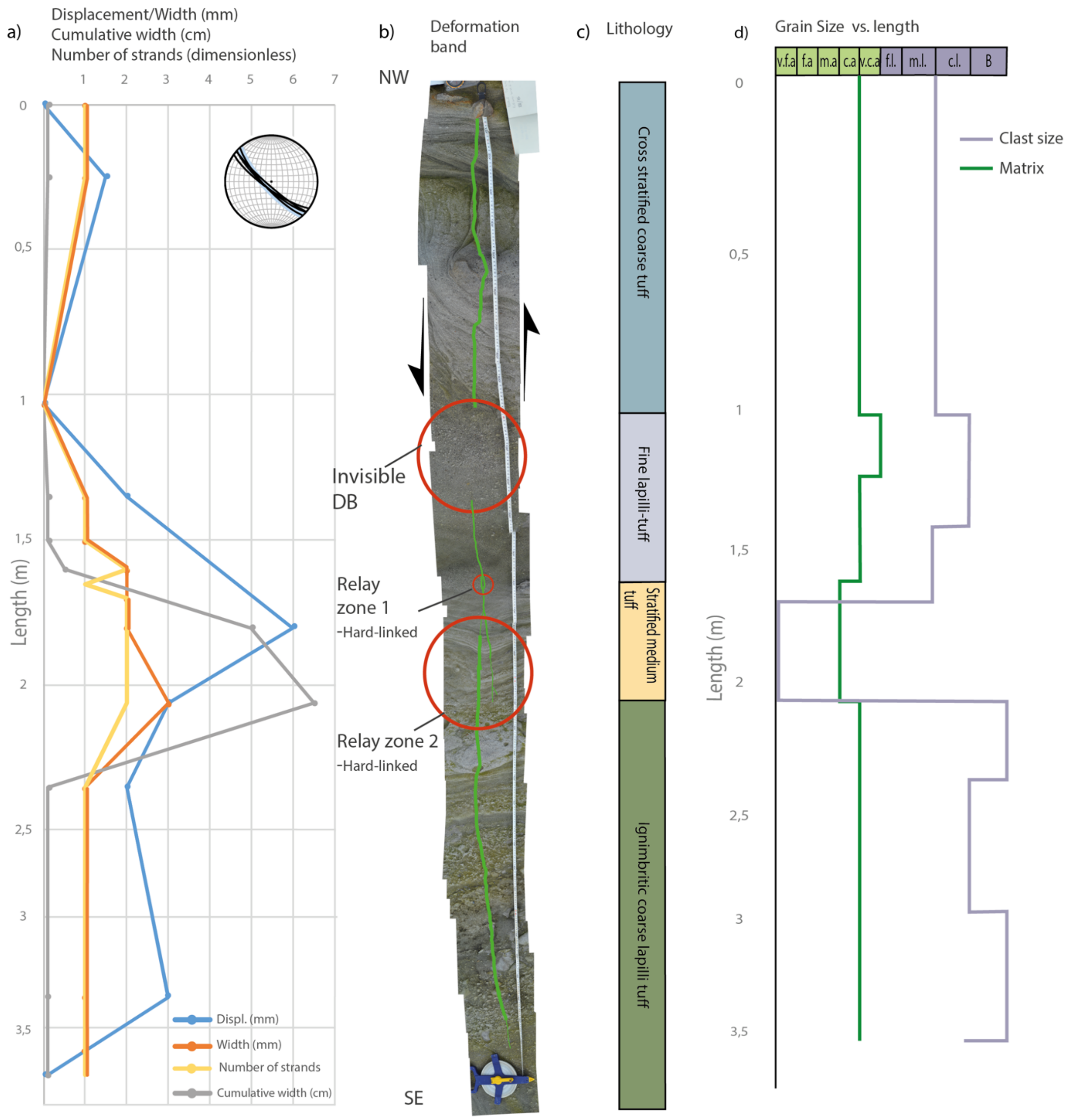

Summary figure of band 6; the location of band 6 is shown in Figure 5.11A. The top of the figure point towards the NW, A) A diagram over different parameters along the band. Displacement and width are measured in millimetres, cumulative width is displayed in cm and the number of strands is dimensionless. The lower-hemisphere stereonet shows the orientation of band 6. B) Photomosaic over band 6 with green line drawings illustrating the DB. Kinematic indicators are displayed by black arrows. Zones of interest is highlighted with red circles. C) A block diagram of the lithology along the band. D) Grain size plot of the matrix and clast material.

Incipient band 8:

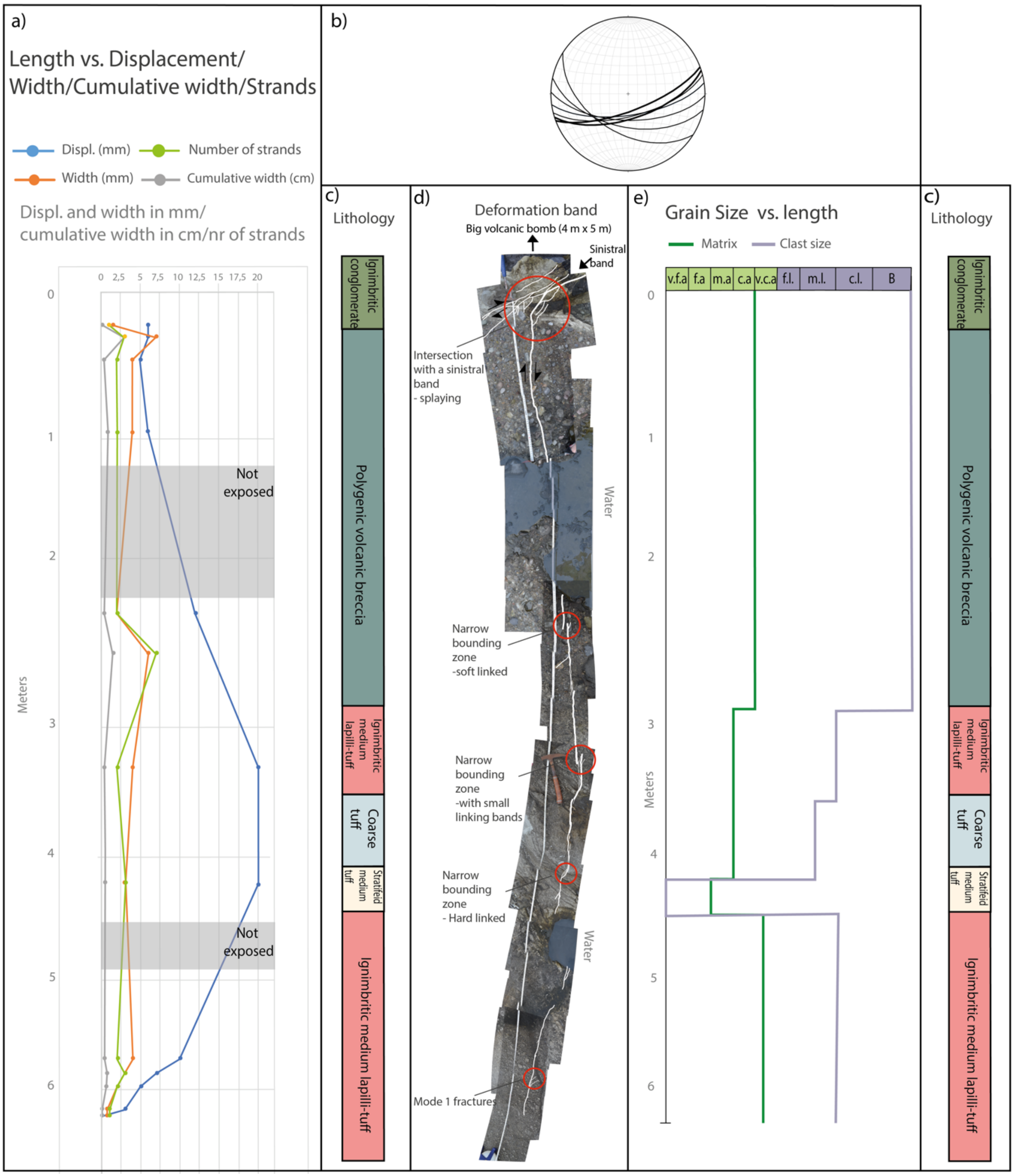

Summary figure of band 8; the location of band 8 is shown in Figure 5.11A. The top of the figure point towards the SW, A) A diagram over different parameters along the band. Displacement and width are measured in millimetres, cumulative width is displayed in cm and the number of strands is dimensionless. B) Lower-hemisphere stereonet of the orientation of band 8. C) A block diagram of the lithology along the band D) Photomosaic over band 8 with white line drawings illustrating the DB. Kinematic indicators are displayed by black arrows. Zones of interest is highlighted with red circles. E) Grain size plot of the matrix and clast material.

Band 9:

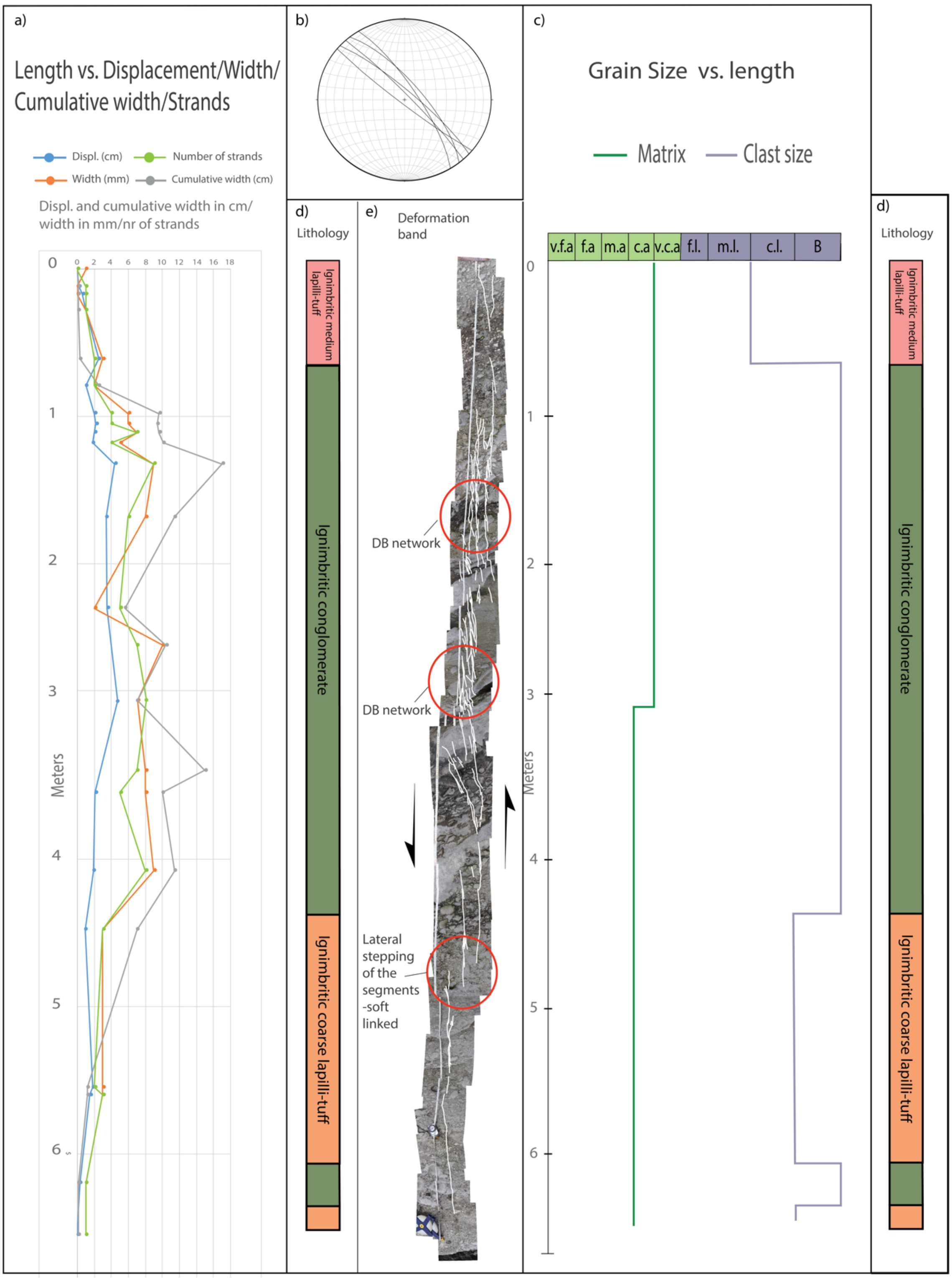

Summary figure of band 9; the location of band 9 is shown in Figure 5.11A. The top of the figure point towards the NW, A) A diagram over different parameters along the band. Displacement and width are measured in millimetres, cumulative width is displayed in cm and the number of strands is dimensionless. B) Lower-hemisphere stereonet of the orientation of band 8. C) A block diagram of the lithology along the band D) Photomosaic over band 8 with white line drawings illustrating the DB. Kinematic indicators are displayed by black arrows. Zones of interest is highlighted with red circles. E) Grain size plot of the matrix and clast material.

Appendix II: Additional figures of mature deformation bands

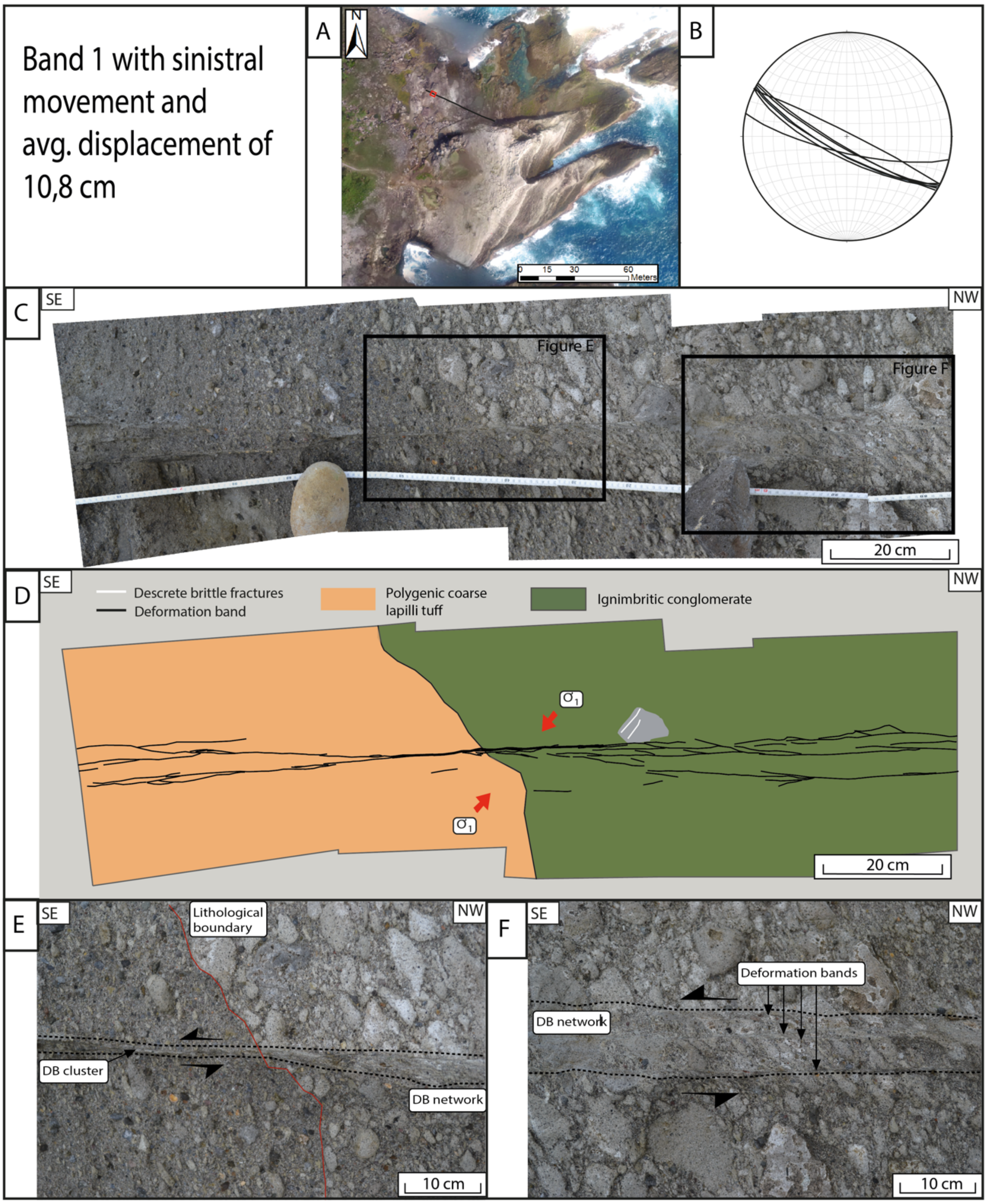

Band 1 with sinistral movement and avg. displacement of 10,8 cm

Summary figure of mature band 4:

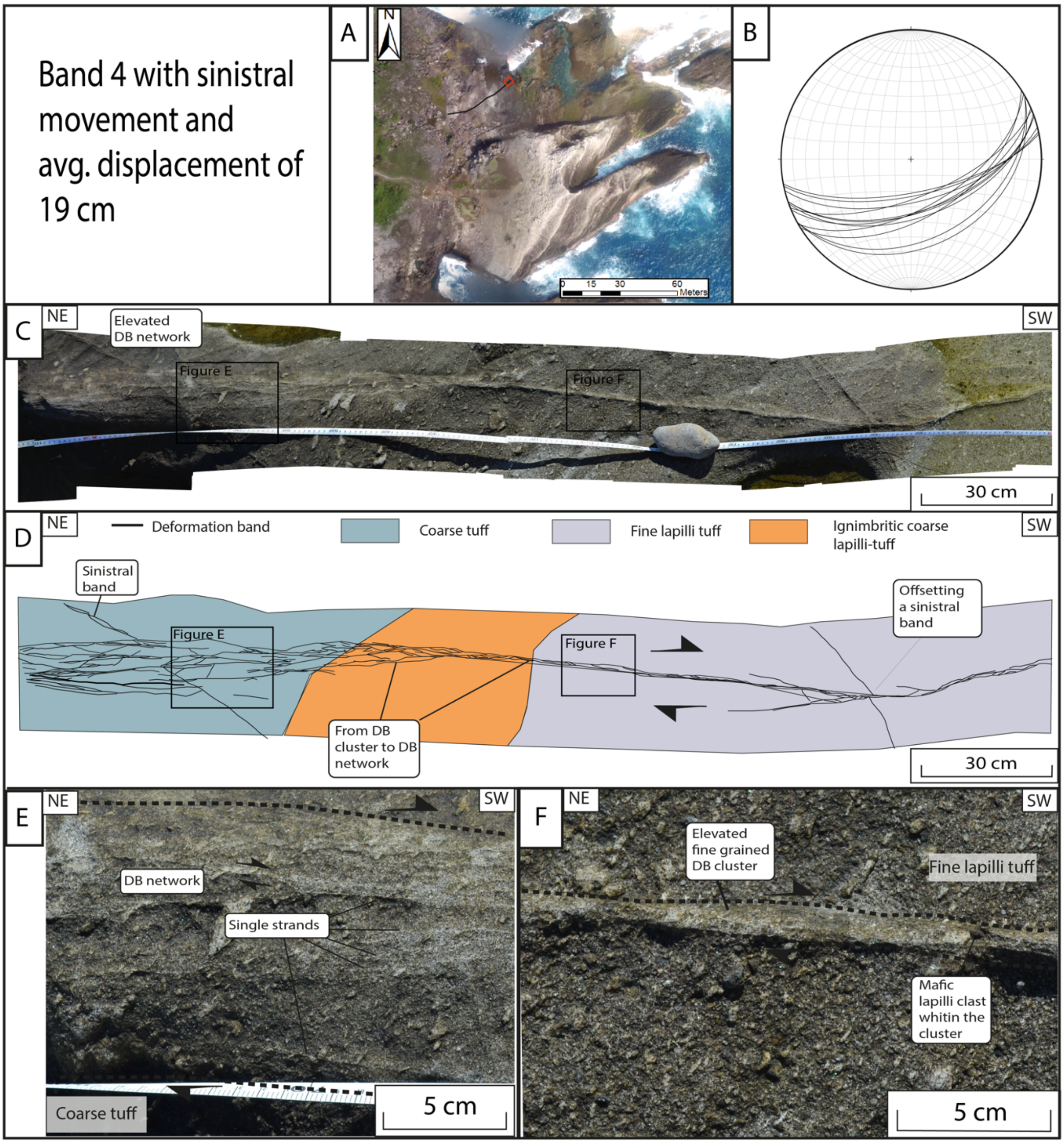

Mature band 3: Graph correlated with grain size:

Appendix III: Additional fault figures

Summary figure of fault 1:

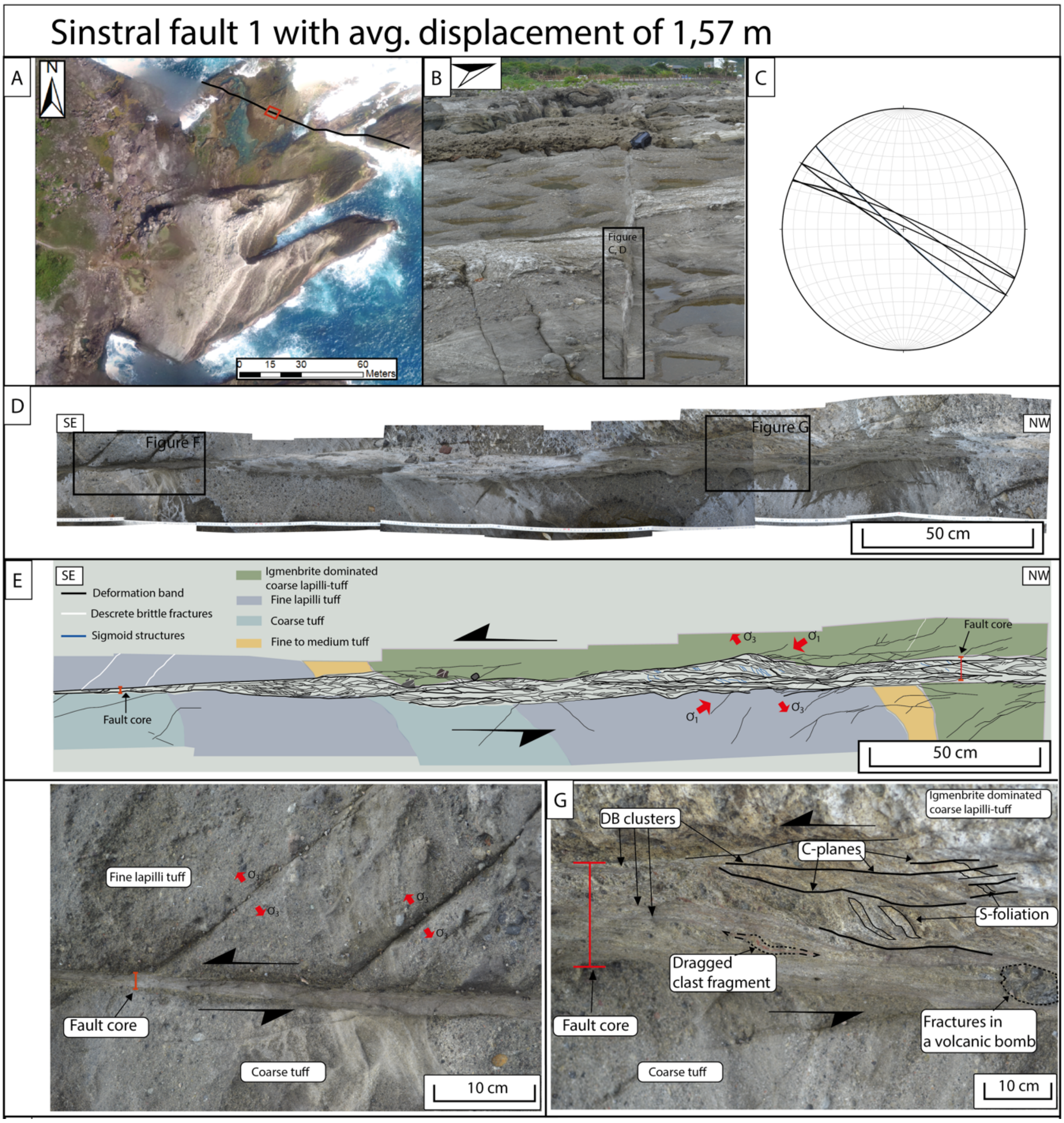

Branch density map of fault 3:

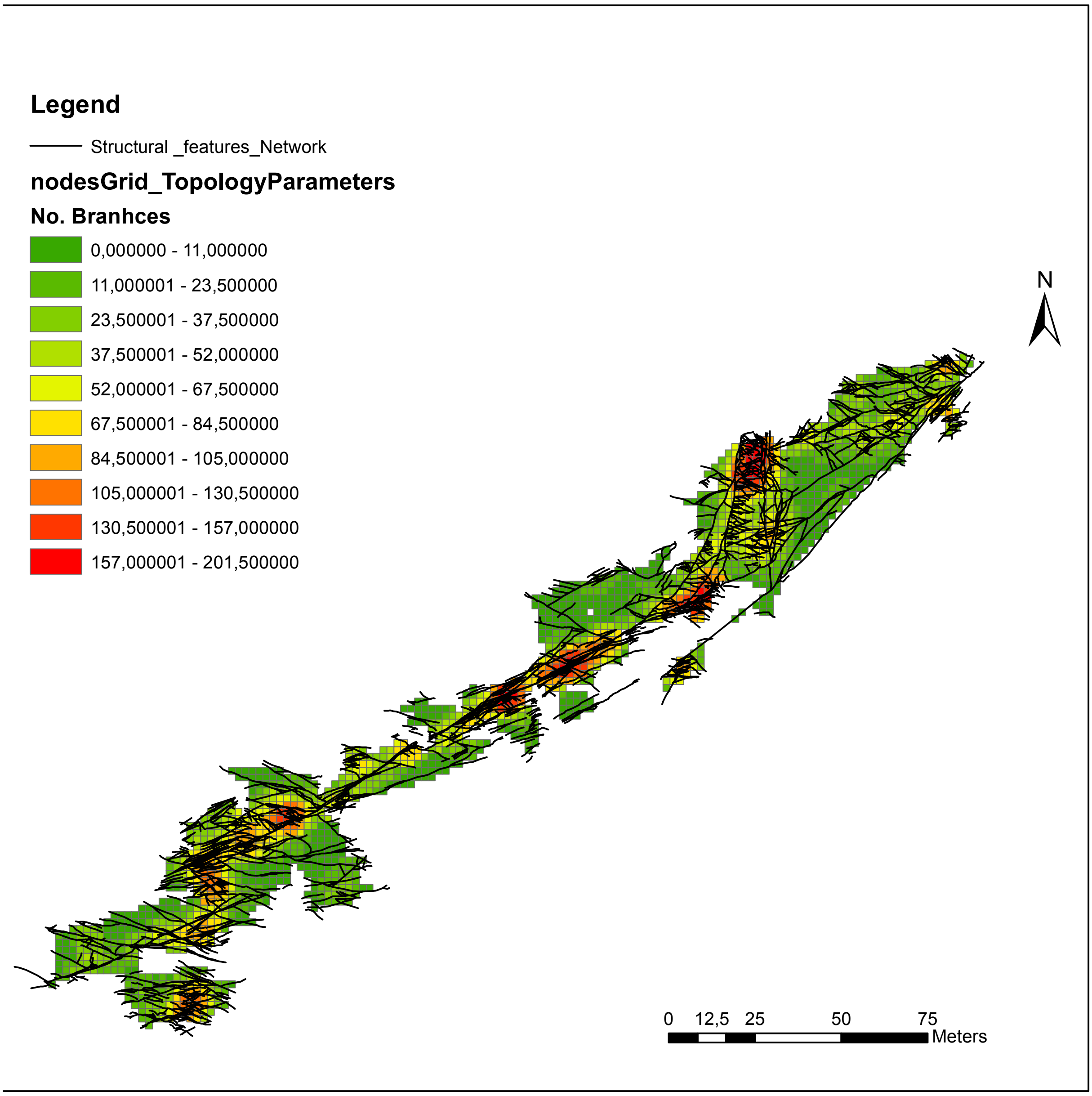

Structural map of fault 3:

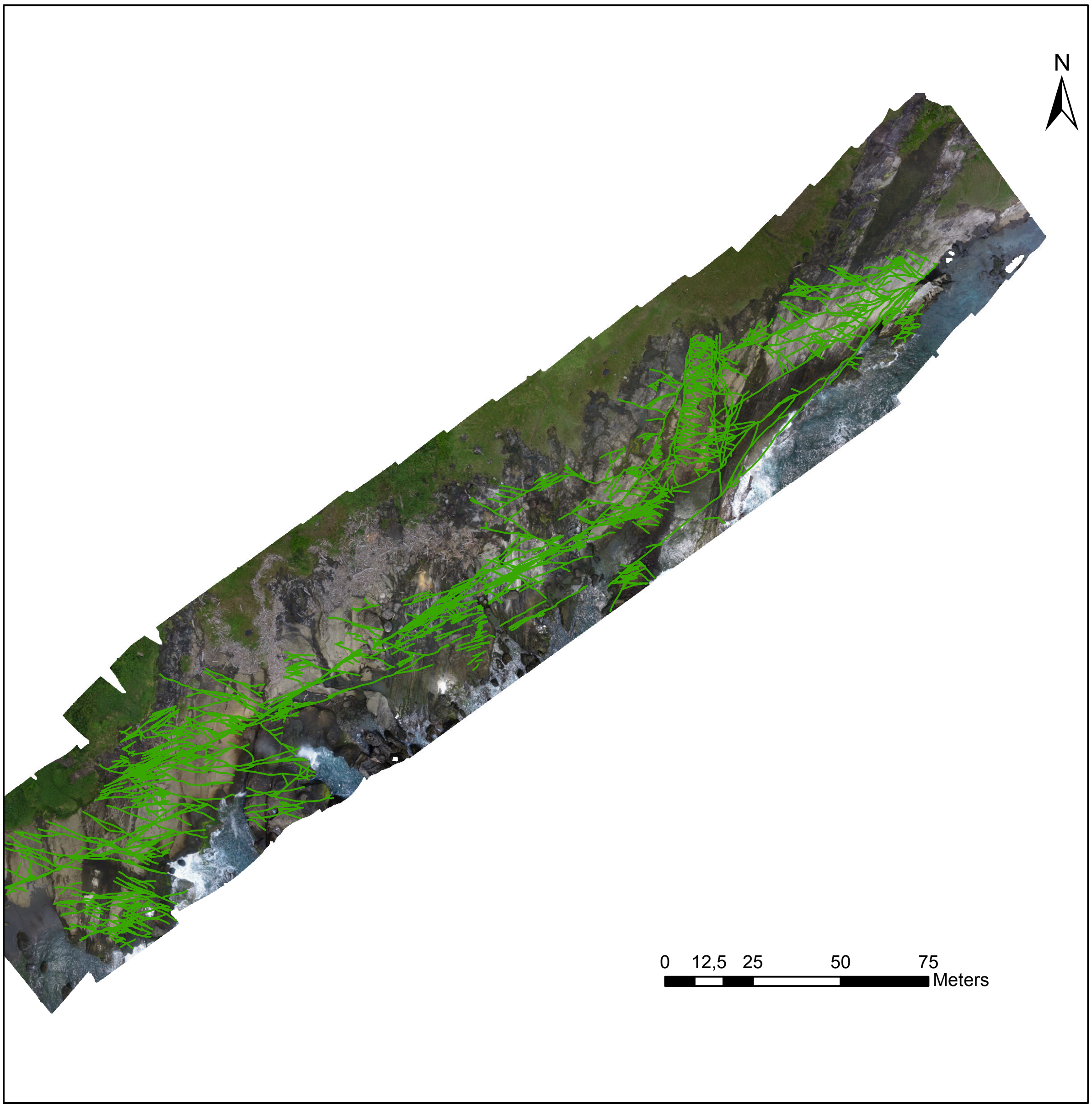

Field data: Pure compaction bands

type 1-målinger

hvor (cm)	N0	Is (mm)	T (cm)	lengde cm	gr.size
3,5	1	9	0,5	18	ms
5	2	16	0,8	24,5	ms
7,5	3	39	0,9	80	ms
12,5	4		1	76	ms
			0,8	49,625	

1-2

hvor (cm)	N0	Is (mm)	T (cm)	lengde cm	gr.size
3	1	25	0,3	22	ms
5,5	2	21	0,6	12,3	ms
8	3	10	0,3	11	ms
9,5	4	35	1,5	18	ms
14	5	19	0,7	15	ms
16	6	25	0,3	25,5	ms
19,5	7		0,6	18	ms
			0,61428571	17,4	

1-3

hvor (cm)	N0	Is (mm)	T(mm)	lengde cm	gr.size
6	1	10	1,1	64	ms-cs
7,5	2	22	0,5	27	ms-cs
10,5	3	25	0,4	12	ms
13	4	15	1,3	19	ms
15,5	5	22	0,3	18	ms
18	6	16	0,7	29	ms
21	7	-	1	15	cs

1-4

hvor (cm)	N0	Is (mm)	T(cm)	lengde	gr.size	clast size (cm)
8	1	40	1,5	130	cs	0,5-4
7,5	2	22	0,5	27	cs	0,5-4

10,5	3	25	0,4	12	cs	0,5-4
13	4	15	1,3	19	cs	0,5-4
15,5	5	22	0,3	18	cs	0,5-4
18	6	16	0,7	29	cs	0,5-4
21	7	-	1	15	cs	0,5-4

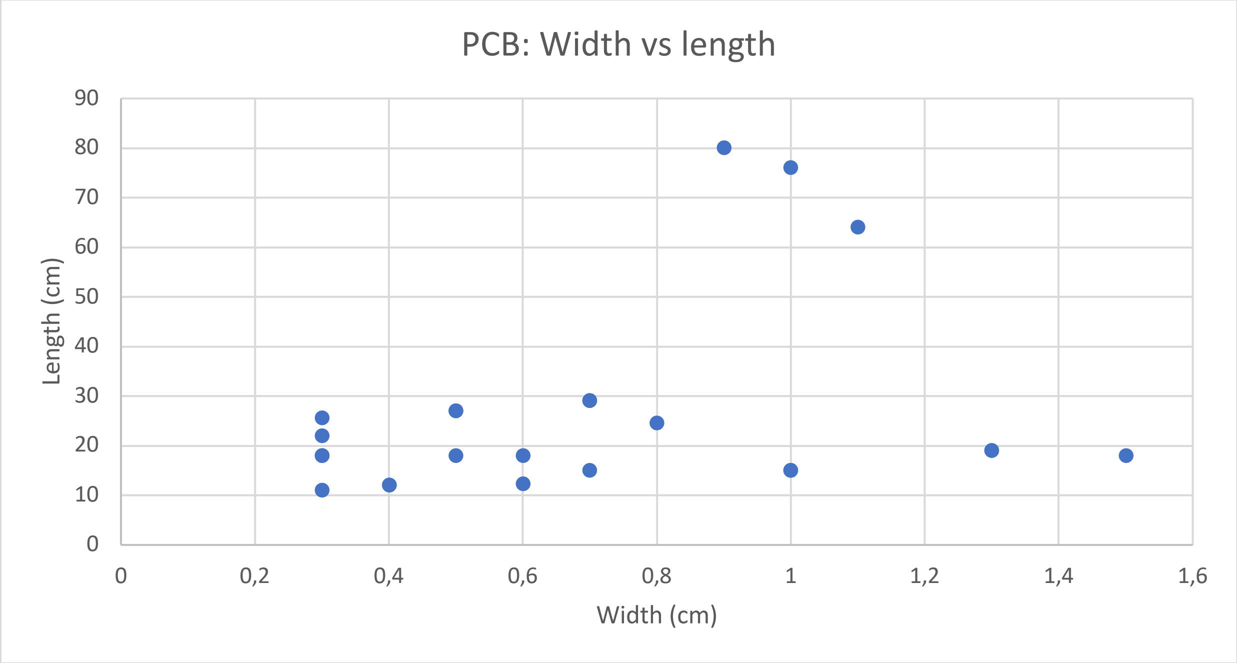

Appendix: V: Field data

	Incipient bands		
	displ. (mm)	width (mm)	strands
band 5	0	0,1	1
	0,5	0,1	1
		0,3	2
	0,3	0,1	1
	0,3	0,8	2
	0,5	0,1	1
	0,25	0,08	1
		0,8	
	0,4	0,1	1
	0,22	0,1	1
			3
	0,9	0,5	2
		0,3	3
	0,7	0,07	2
	0,1	0,1	1
	0	0,1	2
band 9	0	0,1	0
	0,2	0,1	1
	0,6	0,1	1
	1	0,1	1
	2,5	0,3	2
	1	2,5	2
	2	9,6	4
	2,2	9,4	4
	2	9,6	7
	1,8	10,1	4
	4,4	17	9
	3,4	11,4	6
	3,5	5,6	5
		10,4	7
	4,5	7	8
		15	7
	2,1	10	5
	1,9	11,4	8
	0,9	7	3
	1,8	1,2	2
	1,5	1,2	3
	0,3	0,1	1
	0	0,1	1

band 6	0	0,1	1
	0,15	0,1	1
	0	0	0
	0,2	0,1	1
		0,1	1
		0,5	2
			1
			2
	0,6	0,5	2
	0,3	0,65	2
	0,2	0,1	1
	0,3	0,1	1
	0	0,1	1
band 10	0,6	1,5	1
	0,6	3	3
	0,5	0,4	2
	0,6	0,9	2
	1,2	0,4	2
		1,5	7
			4
	2	0,4	2
	2	0,5	3
	1	0,4	2
	0,7	0,7	3
	0,5	0,6	2
	0,3	0,07	1
	0	0,07	1
band 7	0,3	0,1	1
	0,3	0,1	1
	0,1	0,07	1
	0,3	0,06	1
	0,1	0,15	2
	0,3	0,4	2
	0,6	4	5
	0,3	0,3	2

Mature bands

bånd 1	Displacement	width (cm)	Strands
	10,2	0,2	1
		0,22	2
	9	0,9	2
	12	0,5	1
		4,7	7
	11	0,5	2
		1,7	5
	11	6	5
	18	1,3	9
	17	4,7	4
		40,9	15
		30	9
	13	2	3
	10	1	2
	12	6,1	7
	12,2	29	7
		43	9
	12	3,5	7
		1,4	3
	10	1,5	5
		8	9
	9	0,5	2
	11	2	5
	8	8	7
	8,5	5	9
	6	2	2
	5	5,3	6
band 2			
	4	9	12
	10	11,5	13
	6	2,3	7
		5,2	5
	10,7	1,5	6
		4,2	11
	19	16,3	11

	20,5	7	8
		6	10
	13,5	10,4	14
		17,1	13
	12,7	6,7	8
	12,5	4	5
	12	6	12
	10,5	4,2	5
	22	11	10
	16	11,5	15
	21,5	20	24
	20	19	27
	12	3,4	6
	20,2	5,3	8
	20,35	4	8
	17	6,6	10
	3,7	3	2
	30	59	18
	11,30	9	8
	21,5	9	13
	10	2	7
	11	3,7	8
	10	3,1	7
		31	13
	5,2	12	7
	7,5	7	12
band 3			
	2,1	1,2	6
	4	1,8	6
	8	4,1	7
	6,3	4,3	7
	9	2	5
	14,5	0,6	4

	6,5	0,5	3
	10	2,4	5
	7,2	0,7	4
	9	4,6	7
	7,4	0,6	3
	8,4	1,6	10
	7	3	8
	5,7	0,9	1
	5	13	10
	5	4,5	5
	6,3	4,3	7
	6,2	2	6
	6	1,2	5
	8,2	18	4
	7,9	4,5	4
		23,5	7
	4,5	1,2	2
	4,5	1	4
	3	0,2	1
	1,7	0,5	3
	4	0,7	3
	8	1,8	5
	3,2	1,2	3
	4,7	1,3	4
	2,5	3,5	6
	4,5	1,1	4
	3,5	2,2	8
	4	2,4	6
	3,5	0,7	4
	5	4	6
	3,5	2,6	4
	2	1	4
band 4			
		13,7	12
	32	20	11
	25	21	16
	32	29	33
	22	5,4	15
	22	4	11
	14,4	23	8
		43	8

		42	15
	11	36	20
	23	8,5	6
	26	17	8
	20	2,5	5
		13	8
	10	2	3
		12	14
	15,5	5	9

	Faults		
fault 3	displ (cm)	width (cm)	Strands/Slip surfaces (dimensionless)
	70	34	17
	140	90	8
	203	36	1
	89	4	1
	266	66	7
	130	135	57
	110	67	50
	192	220	36
	253	171	106
	148	139	98
	189	170	84
fault 2		10	16
	260	5,5	7
	250	21	30
	181	9	17
	175	9,5	25
	172	53,5	59

fault 1	130	19	15
	129	30	13
	120	29	31
	145	10	11
	183	7	18
	144	8	1
		3,5	1
	175	13	1